Hybrid Intensity and Time-Of-Flight Signal Processing Techniques For Intelligent Distance Sensors

by

Itaru Hiromi

Submitted to the Department of Electrical Engineering and Computer Science
in partial fulfillment of the requirements for the degree of

Master of Science in Electrical Engineering

at the

MASSACHUSETTS INSTITUTE OF TECHNOLOGY

June 2013

Author . . . .
Department of Electrical Engineering and Computer Science
February 15th, 2013

Certified by . . . .
Charles G. Sodini
LeBel Professor of Electrical Engineering
Thesis Supervisor

Certified by . . . .
Phil Golden
Principal Design Engineer/Project Manager
Thesis Supervisor

Accepted by . . . .
Dennis M. Freeman
Chairman, Department Committee on Graduate Theses

Hybrid Intensity and Time-Of-Flight Signal Processing Techniques For Intelligent Distance Sensors

by

Itaru Hiromi

Submitted to the Department of Electrical Engineering and Computer Science
on February 15th, 2013, in partial fulfillment of the
requirements for the degree of
Master of Science in Electrical Engineering

Abstract

With the advent of "smart" consumer electronics, distance sensing is an increasingly important field in optical sensing. A novel approach to active infrared(IR) 1D distance sensing is proposed, employing both intensity and time-of-flight information. Conventional intensity based sensors lack in distance accuracy, and conventional time-of-flight sensors suffer from crosstalk and backscatter issues. The purpose of this work is to explore the solution space to these issues that hybrid intensity/time-of-flight systems enable, and to investigate their characteristics.

Optical behavior of time-of-flight and intensity of an active IR system is analyzed, and a comprehensive reflection model is created. This model is then applied to describe discrete objects, and a parameterized object model is developed. Techniques such as the use of differentiated signals, least square estimation, and optimization algorithms are introduced and applied to the object model. A range of techniques based on specific use cases are developed, and their capabilities and limitations are discussed.

Results show that in a limited set of conditions, combining time-of-flight and intensity information can allow the extraction of distance in conditions that are typically unfavorable for conventional methods, such as high crosstalk or high backscatter environments. Used in the right conditions, these techniques can gain immunity to these sources of error, at the cost of higher computational complexity.

Thesis Supervisor: Charles G. Sodini
Title: LeBel Professor of Electrical Engineering

Thesis Supervisor: Phil Golden
Title: Principal Design Engineer/Project Manager

Acknowledgments

First and foremost, I would like to thank my supersor and manager Phil Golden for providing me opportunity and support from the beginning to end of this project. I would like to thank my former mentor Dave Ritter for teaching me that nothing is impossible until you've proven it, and for insisting on the feasibility of the initial inspiration for this project.

I am extremely grateful for the time and effort spent by my advisor Professor Charles Sodini, and for his tolerance in dealing with a student who, at times, may have seemed to fall off the face of the earth.

My sincere thanks goes to all my colleagues at Intersil Corporation who have provided me their technical and philosophical wisdom through out the project. I extend my gratitude to my former colleagues at Apple Inc. whose insight on optical systems have given me a new perspective on the subject.

Last but not least, I thank my parents for supporting me through college and this project. They are both my largest source of inspiration and motivation, and true heroes in my eyes.

And to all my climbing/canyoneering/caving friends out there that haven't seen me for months: I'm back.

Contents

4 Real Time Parameter Extraction Techniques 81

List of Figures

List of Tables

Chapter 1

Introduction

Spatial characterization is a long studied field with many competing technologies, including but not limited to 3D cameras, structured light, LIDAR, and many others.

An approach to the particular problem of distance sensing from low level sensors is proposed, combining the technologies of intensity based proximity sensors and time-of-flight distance sensors. Methods of combining the two independent sources of information are discussed, and compared to conventional means. The goal of this study is to investigate the solution space to the challenges encountered in intensity based and time-of-flight distance sensors by utilizing information from both.

This chapter is dedicated to introducing the state of spatial characterization, in particular 1D distance sensing. Several system level traits will be discussed such as range, field of view, power, size, and cost, and the potential market for low cost monolithic sensors is discussed.

Chapter two describes a model of the optical environment as viewed from a time-of-flight sensor. A general model will be established using reflectance models and basic optics.

Chapter three extends the model to describe objects, and will develop a parametric model of an object in the field of view of the sensor.

Chapter four will explore the properties of the object parameter model developed in chapter three, and will introduce several real time techniques unique to hybrid intensity/time-of-flight systems for determining distance under unfavorable conditions.

Chapter five will broaden the discussion in chapter four to account for multiple readings, and will discuss algorithms that will extend the capabilities of the techniques developed in chapter four.

Chapter six will provide a comprehensive summary of the capabilities and limitations of hybrid intensity/time-of-flight systems, and will discusses design trade offs and applications that best suit the technology.

1.1 Intelligent Distance Sensing

1.1.1 Motivations for Spatial Characterization

The idea of spatial characterization in the field of discrete Integrated Circuit (IC) sensors are motivated by the recent trends in consumer electronics for "smart" devices. Optical sensing ICs have established a place in this market with proximity sensors for mobile applications, primarily in use for detecting when a mobile phone is placed against the ear.

Spatial "awareness" of smart devices is certainly not a new idea, but one that has been increasing in popularity. Implementations in lighting, bathroom units, automobiles and security has been around for over a decade, but there has been little advancement in the form factor or power consumption since their introduction. IC sensors have the potential of delivering small, low power solutions to many of these applications, as well as introducing similar functions to a whole range of electronics and appliances that were previously thought to not be suitable for the technology.

Another important motivation is the trend for gesture based interfaces in consumer electronics. Especially with the introduction of Kinect in 2010, open-air gesture has received a lot of interest, and is considered by some as the "holy grail" of user interfaces. Most gesture recognition solutions are currently implemented using power hungry cameras and structured light.

Based on these trends there appears to be a gap in the current technology for low power spatial characterization. Monolithic System-On-Chip solutions for distance sensing and event detection beyond the basic proximity sensing has just begun to enter the market as of 2013. This work will investigate one such approach, combining time-of-flight techniques and intensity based techniques using a single photodetector.

1.1.2 From 5D to 1D: Challenges in Distance Sensing

For many applications, the acquisition of spatial information is the goal in itself. 3D scanning and 3D mapping are just a few examples. However, for most other applications, the end goal is to detect an event. This event could be the presence of an object, a target reaching a specific location, or the prediction of a collision. If given a 3D model of a particular situation, most events can be detected with the use of generous computation. However, this approach is generally extremely computation intensive, and requires bulky and power hungry hardware to obtain the spatial information necessary.

However, many simple events do not require a full 3D model, and can be detected by much more primitive means. A 1D distance sensor is one such approach. Distance is the inherently quantitative language to describe the relationship between two objects, and is often the only metric required. The primary advantage for using a distance sensor over a 3D spatial characterization technique is due to the amount of information collected, distance sensors are inherently more compact and require less power. In fact, many 3D spatial characterization techniques are simply arrays of distance sensors or a single distance sensor multiplexed to scan through the other dimensions.

It is important to recognize here some issues that come with the fact that a distance sensor is one dimensional. Because of the 3 dimensional nature of the world, describing a feature as 1 dimension requires specifying how the other two dimensions are treated. In fact, more generally speaking, an active reflection based sensor has up to 5 dimensions of interest; 2 spatial dimensions at the illumination source and detector each, and time-of-flight or 'depth'.

Perhaps the application of this technique that most illustrates exactly how much information can be encoded by the reflection of light is the CORNAR project conducted by the Camera Culture group at the MIT Media Lab. The CORNAR projects takes a series of picosecond resolution images, each illuminated by a coherent beam of light. By processing this large amount of data collected over 5 dimensions (4 spatial dimensions and time-of-flight), this project demonstrates the capability to "look around corners", generating 3D models of objects hidden from the camera's field of view [11].

A typical distance sensor is taking a small slice of the 5D information present in the system, and computes a single distance. The process in which these dimensions are reduced is of particular importance in understanding the tradeoffs involved in distance sensor design.

1.1.3 Multipath, Field of View, and Target Ambiguity

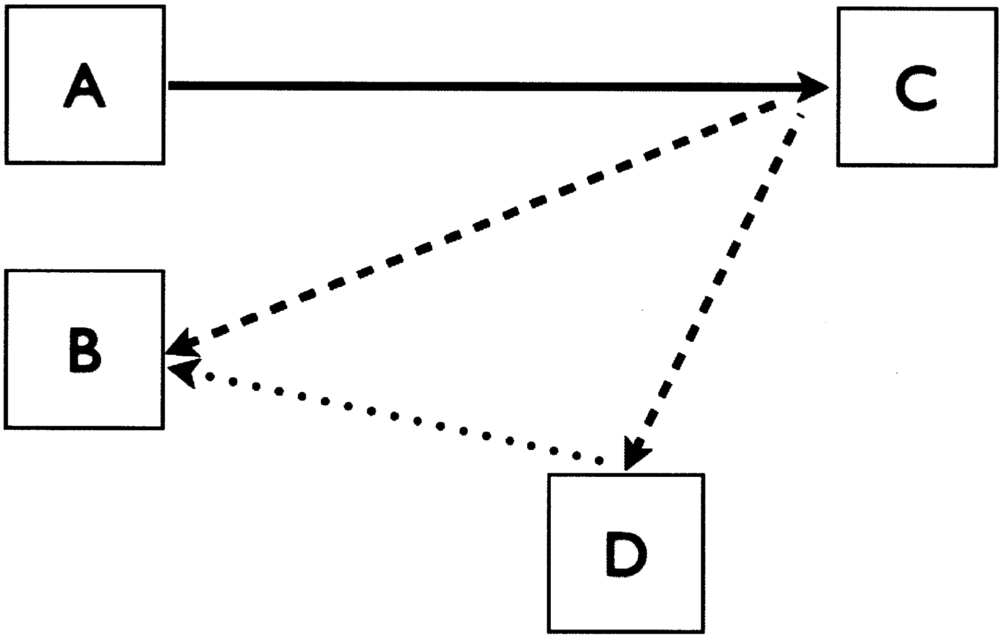

Figure 1-1: A Simple Multipath Scenario. Two optical paths A-C-B, and a weaker A-C-D-B are both detected by the detector B.

The first issue to recognize is that there are always multiple optical pathways for the light to travel. Figure 1-1 illustrates this issue for a simple scenario. A sensor with source A and detector B emits a signal which strikes object C and is reflected back. However, another object D is also present, and also reflects the signal from C and back at the detector. Different sensor technologies are designed to respond to these different reflection paths, presenting very different requirements in both opto-mechanical and opto-electrical considerations.

Another important parameter to introduce, particularly for detecting events, is the field of view. Also known as angle of view for photography, this metric measures the extent of the physical world the sensor is looking at, and consequently influences the nature of the measured distance. Distance sensors with a wide field of view can be advantageous in detecting certain types of events, specifically when the target of interest is not in a guaranteed orientation from the sensor, such as in the case for presence detection and collision detection.

However, a wider field of view also implies that there may be more than one object in the field of view, in which case the both objects would contribute to the signal. Figure 1-2shows a the same scene, but with a wide field of view source. Note that on top of the signals shown for the previous example, the paths A-D-B and A-D-C-B are added to the picture, resulting in further ambiguity.

There are three general ways a system can respond to multiple paths and multiple objects. The first is to sample along the relevant dimension. These systems would report all of the paths and their respective strengths, preserving as much information about the scene as possible. The second is select the information, most commonly by reporting the minimum distance at which the signal strength exceeds a certain signal, or by having selective responsively to a certain incident angle or distance. The third is to add or average the information according to some function. Adding or averaging always results in the best signal Signal to Noise Ratio (SNR), but at the cost of the information being inherently less useful, as the significance of the reading is ambiguous, no longer providing a one-to-one relationship between a physical scene and it's corresponding reading. It is always possible to post process sampled information to emulate a selective or averaging system, but usually at the cost of

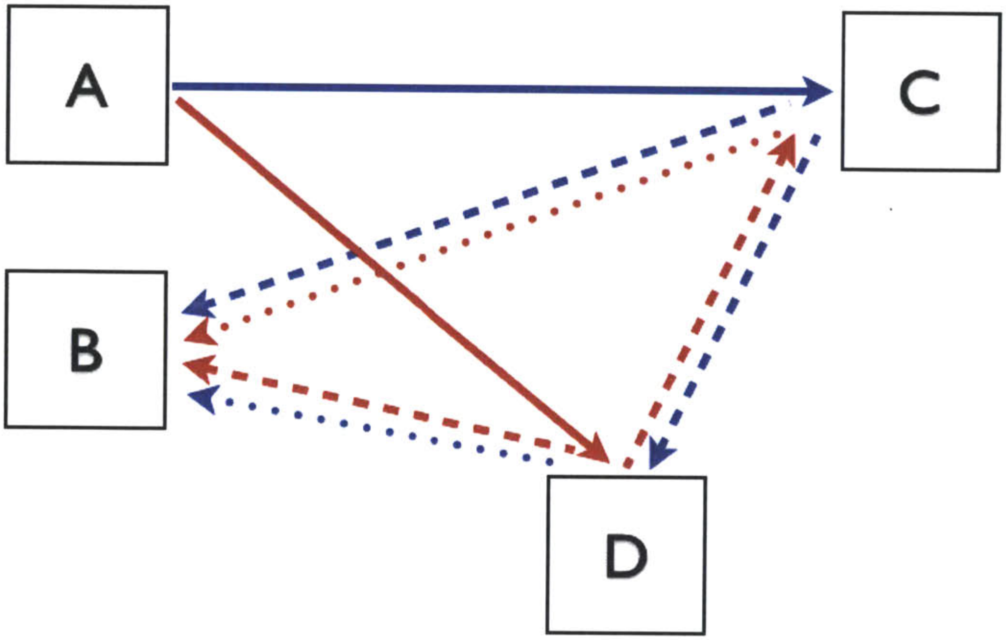

Figure 1-2: Wide Field of View Scenario. A source with a wide radiation profile adds paths A-D-B and A-D-C-B (red), on top of the existing paths (blue)

increased quantization noise and power. Typical tradeoffs and implementations for these three strategies are summarized in Figure 1-3 and Table 1.1.

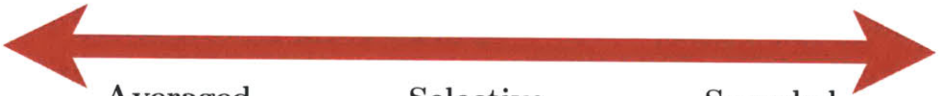

Averaged	**Selective**	**Sampled**
Simple		Complex
Low Cost		Expensive
Low Power		Resource Intensive
Ambigous		Unambigous

Figure 1-3: Properties of Averaged, Selective, and Sampled Systems

This work will focus on an implementation where all of the five dimensions are averaged or summed, such that a wide field of view is achieved with the simplest circuitry and optical set up possible. This also introduces the largest ambiguity in the significance of the signal, making it prone to systematic errors caused by multi path and target ambiguity issues.

Table 1.1: Common Language and Implementations for Averaged, Selected, and Sampled Systems

-	Averaged	Selective	Sampled
Time-Of-Flight	I-TOF	D-TOF	Deconvolution
Illumination Source (Example)	Dispersed Source (LED)	Coherent Source (Laser)	Scanned Source (Laser & Mirror)
Detector	Single Detector	Slit/Aperature	Pixelated/Arrayed Sensor

1.2 Active IR Distance Sensing Technologies

Most distance sensors use the properties of the propagation of infrared light or ultrasound waves through a medium, due to the fact that these waves are not perceivable by the human body. The basic concept behind these sensors is to drive an source, typically a laser or LED for infrared light, or a transducer for sonar/ultrasound sensors, and characterize the response to extract distance. This section will introduce three methods that use infrared radiation to measure distance, and discuss some of their properties and common applications.

1.2.1 Active IR Intensity Based Systems

Intensity based systems are the most primitive of the three, and are not strictly distance sensors, but proximity sensors. Reflections from an IR LED are measured, and the strength of the reflected signal is thresholded to detect proximity. These sensors are extremely simple, and can be made very small and low power. Although not technically a distance sensor, we will briefly discuss some of the properties of monolithic IC proximity sensors as they will later be addressed in the context of distance sensing.

These primitive sensors rely on the assumption that objects closer will present a stronger reflected signal than those that are further away. However, they have the disadvantage that they are not capable of reporting distance, as the reflected signal strength is also a function of the reflectivity and size of the target. In an extreme example, a material that is 100% absorptive would not be registered (or be equivalently, at infinite distance) regardless of how close it is from the sensor.

Intensity based optical proximity sensors have been around for decades. However, as an monolithic IC sensor, they have only become popularized for their use in smart phones in the last 5 years. Monolithic IC proximity sensors are either stand alone solutions or are used in conjunction with an external IR LED, and are available on the market for \$3 or less. Package sizes have evolved to be as small as 7.4mm^2 for a complete solution. Ranges are typically on the order of approximately 10cm, although some models have higher power modes that claim operation up to 50cm. Their field of view vary depending on the LED's angular intensity distribution, but are typically around 30 degrees to 120 degrees.

1.2.2 Triangulation

Triangulation based sensors are the are one of the most common type of compact distance sensors in the market, and are commonly used in robotics, manufacturing, and presence detection. The nature of the technology fundamentally limits these systems to a narrow field of view, and require a certain minimum size for the sensor that is proportional to the range of the sensor. This technology is best suited for distances in the 10cm $\sim$ 1m range, and a typical sensor would be 20mm x 40mm x 20mm (L x W x H)

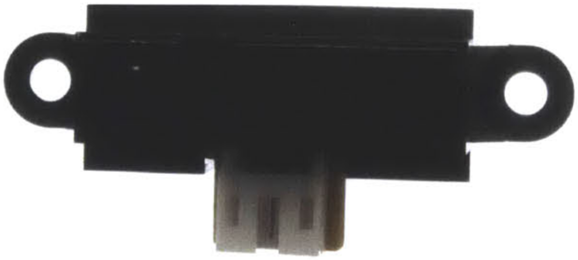

Figure 1-4: A Triangulation Based Distance Sensor : Sharp GP2Y0A21YK [5]

The 3D equivalent of triangulation based of sensors are often called structured light, and are used for structure light 3D scanners. Possibly the most prevalent of these scanners is the Microsoft Kinect, an imaging system used for Human-Machine-Interaction for the gaming console Xbox 360.

1.2.3 Time-Of-Flight Systems

Time Of Flight systems take advantage of the finite speed of light and measure distance by measuring the time taken for an optical signal to strike a reflective target and reflect back. Conceptually, these systems are based on the same principles as RADAR, but use modulated light (typically near-infrared) as a radiation source. A light source is either pulsed or modulated with a sinusoidal signal, which is then detected and converted to distance.

Time-of-Flight systems come in a whole variety of shapes and sizes. The longest distance time of flight sensor in existence is likely the sensor monitoring the distance of the moon, measuring a distance of over 300,000km to a precision of a few centimeters. While the equipment that monitors the distance to the moon consists of a full sized telescope and a room full of electronics, the smallest time of flight sensor is embedded in a pixel of a time-of-flight camera.

Although based on the same physical properties, three basic methods of measuring and processing the time of flight exist, time domain sampling, direct conversion, and indirect or ratiometric conversion.

1.2.3.1 Time Domain Sampling

Time Domain Sampling is the most basic and brute force method of measuring the time of flight, and is done by sampling the reflected signal at a very high sampling rate, and processing the data using digital signal processing techniques. Due to the large amount of information required, this approach is very power intensive and requires significant computational resources and is most commonly used in sophisticated LIDAR equipment. However, it is also the most powerful in that it preserves multi path information, and is capable of recording signals from multiple reflections.

1.2.3.2 Direct Conversion Techniques

Direct Conversion techniques are techniques in which the time of flight is directly measured with the use of time-to-analog/time-to-digital circuits or similar. These techniques are sometimes referred by the name "D-TOF" , for Direct Time-Of-Flight [7]. Direct conversion techniques are inherently lossy, because they achieve high gain and sensitivity by triggering off the reflected signal, and thereby limiting the detection to the first reflection path (or combination of reflection paths) that are strong enough to cause the system to trigger. This results in a system that is selective in multi path, at the cost of Signal to Noise Ratio [8].

1.2.3.3 Ratiometric Conversion Techniques

This is contrasted with "I-TOF", for Indirect Time-Of-Flight, which sample the reflected using a windows shuttering scheme or demodulation, a topic that will be discussed in much greater detail in Chapter 2. One of the properties of I-TOF conversion techniques is that they are inherently based on ratiometric measurements, and are primarily implemented using LTI techniques. Unlike Time Domain Sampling, these conversion techniques use demodulation and/or integration, and do not require the circuits to operate at the time scales necessary in Time Domain Sampling. In addition, ratiometric conversion techniques require very little computational resources, and are therefore are the predominant technology in arrayed systems such as Time-Of-Flight Cameras and 3D scanners. Figure 1-5 shows two different implementations of direct and indirect time-of-flight techniques as presented in [8].

1.2.4 Comparison of Distance Sensing Technologies

Table 1.2 shows a comparison of TOF technologies with respect their treatment of each of the 5 dimensions. In general, technologies that involve sampling information have greater capabilities, but are typically large, and expensive.

1.3 Hybrid Intensity/Time-of-Flight

This work aims to introduce yet another class of distance sensing, based off of intensity based and I-TOF techniques, but with unique capabilities only made possible by combining the two forms of information present in a reflected signal. Time-Of-Flight

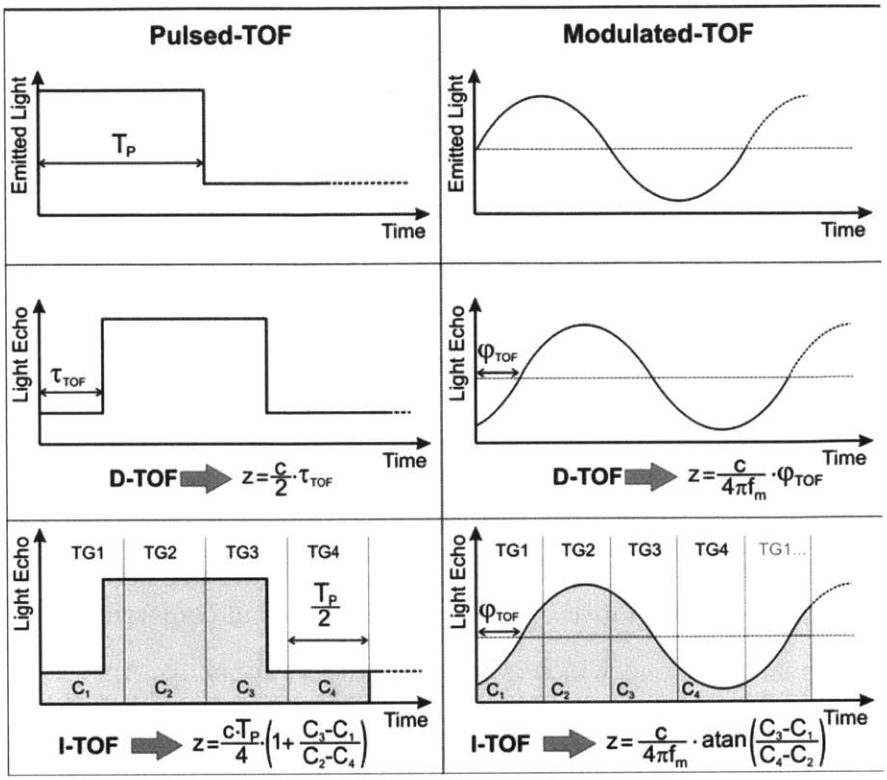

Figure 1-5: Pulsed, Modulated D- and I-TOF measuring techniques using four time-gated photon counters, borrowed from [8]

Table 1.2: Comparison of Distance Sensing Technologies

Technology	Emitter	Detector	TOF	Examples
Intensity Based	Averaged	Averaged	N/A	ISL290XX, Si11XX
Triangulation	Selective	Sampled (1D)	N/A	Sharp GP2 Series
Structured Light	Sampled	Sampled	N/A	Kinect
TOF Distance Sensor	Averaged	Averaged	Averaged	ISL29200
Laser Range Finder	Selective	Selective	Ave./Sel.	Nikon Laser Series
TOF Camera (I-TOF)	Averaged	Sampled	Ave./Sel.	PMD CamCube
LIDAR(Low End)	Sampled	Averaged	Ave./Sel.	Forecast 3D Laser
LIDAR(High End)	Sampled	Averaged	Sampled	EAARL
CODAC	Compressed	Averaged	Sampled	CODAC
CORNAR	Sampled	Sampled	Sampled	CORNAR
Hybrid Intensity/TOF	Averaged	Averaged	Averaged	This Work

information is completely lost in intensity based sensors, and intensity information is not captured for typical D-TOF and I-TOF sensors. Even if the intensity information is captured, TOF sensors typically do not take advantage of this information.

1.3.1 Prior Work

Intersil Corporation (Intersil) is a manufacture of electronic components, including intensity based infrared proximity sensors. From 2008, there has been a development of a time of flight based sensor that is of a similar form factor of a monolithic integrated circuit and external LED. With a part name of ISL29200, this part will be one of the smallest true distance sensors in the market when released[2].

During the feasibility study stages this sensor, challenges regarding crosstalk were quickly discovered, and the concept of quantifying and subtracting out crosstalk were considered in the early stages of the study. As background and target ambiguity issues surfaced, a basic hybrid technique that relied on both the intensity and time-of-flight properties was developed. A paper for an internal conference was written at the time on this subject, and which is included in the appendix A.

This thesis is a direct extension of these findings.

1.3.2 Hybrid Techniques for Intelligent Sensors

The most basic form of using both time-of-flight and intensity information is to remove the effect of crosstalk in the system. Time-of-Flight sensors and intensity based sensors alike are highly prone to crosstalk, which can significantly reduce the accuracy and effective range. If this crosstalk can be measured in advance, it is possible to subtract or cancel the crosstalk out, effectively eliminating the systematic error.

The logical extension to this concept is to apply the technique to background and target ambiguity issues, as well as scenarios where the crosstalk can not be quantified in advance. This paper seeks to explore the solution space to these issues, by modeling both the intensity and time-of-flight of the reflected signal of a wide field of view sensor, and describing it's properties in terms of a finite set of meaningful physical parameters.

Chapter 2

Optical Modeling of Wide Field of View Indirect Time-Of-Flight Systems

A typical time of flight system is shown in the FIgure 2-1, containing the following components:

- Illumination Source: Typically near-infrared light in the 800nm 1000nm range is used for the illumination source, due to it's low (or lack of) visibility, and minor radiation concerns. This light source is modulated by driving circuitry to generate the optical signals necessary for the system. Sometimes a diffuser is used in conjunction with the source to better distribute the light.
- Photodetector: A photodiode is used as a detector, with appropriate optical filters to extract the desired wavelength of light. Lens and mirrors can be used to focus or redirect the light, but we will consider this as part of our detector.
- Circuitry: Analog and Digital circuits are required to drive the illumination source, and to sense and process the detected optical signal.

In this chapter, we will discuss the characterization and modeling of the optical components of the system, ultimately determining the relationship of the circuit

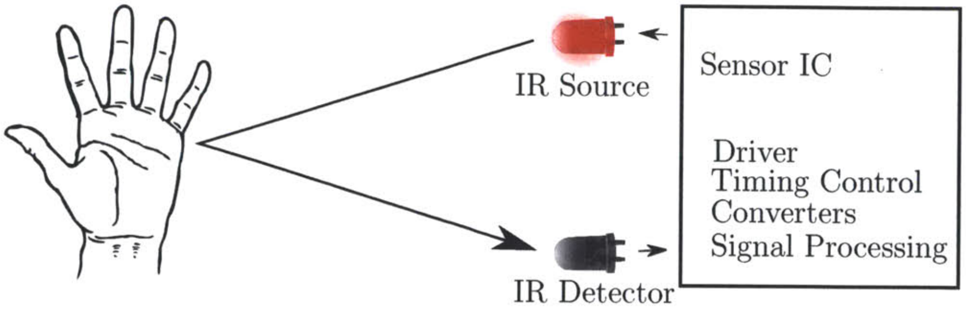

Figure 2-1: System Setup

behavior of the illumination source to the detector. For 3D cameras and LIDAR applications, the sensor and optical elements are arranged such that each pixel of the detector corresponds to a relatively small area. Thus these time of flight systems are easily modeled as a collection of time of flight measurements, each characterized by three points in space, the source, a point on the seen, and the detector. However, for systems that collect light from a wide field of view, the response must be obtained by integrating over the entire field of view.

In order to model the behavior of the system, we must first be able to model the reflections from the "scene" given our illumination source, and then determine it's projection on to the image sensor. This a classic problem in computer graphics, and we will use models and techniques commonly used in this field to obtain our model.

The basic premise of the technique is as follows: for every differential solid angle illuminated by the source, we can find the reflection off an arbitrary surface, and finally find the contribution from that reflection back to the detector. In the model developed in this chapter, we will consider the first reflection only, but in principle, many reflections can be modeled for more realistic results.

2.1 Descriptions of Components

In this section, we will describe the behavior of each component of the optical system. These descriptions will be later assembled to develop a comprehensive model of the optical channel.

2.1.1 Radiance and Light Fields

The entire characteristics of light on any surface can be described using it's light field, a 4 dimensional function measuring radiance as a function of the position and direction. Light fields can be parameterized using a few different systems, one of which is using point $\mathbf{r} = (u, v)$ on a plane or curved surface S, and the direction $\vec{\omega} = (\theta, \phi)$, as shown on the left in Figure 2-2. This is typically the way radiance is defined in optics, as the physical quantities are more easily obtained. Another convention is defined using two points $\mathbf{r}_1 = (u, v)$, and $\mathbf{r}_2 = (s, t)$, one each on two plane or curved surfaces, S_1 and S_2, as shown on the right. The later technique is more common in computer graphics, which usually requires modeling the projection from an object onto a simulated image plane.

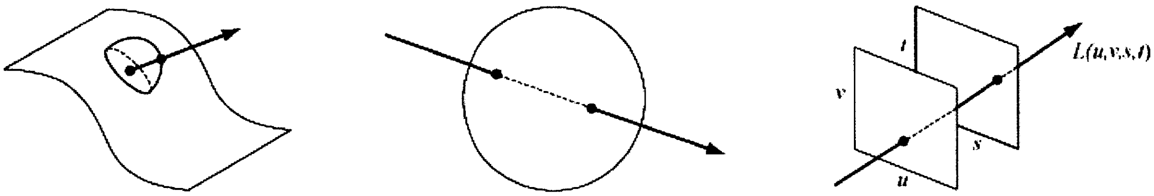

Figure 2-2: Different Parameterizations for the Light Field [3]

Although we will use the later for the most part, we will use both of these expressions interchangeably, under the transformation:

$$\vec{\omega} = \widehat{\mathbf{r}_2 - \mathbf{r}_1} \tag{2.1}$$

$$L(\mathbf{r}_1, \mathbf{r}_2) = L_1(\mathbf{r}_1, \widehat{\mathbf{r}_2 - \mathbf{r}_1}) \tag{2.2}$$

It is important to note that although written as one variable, both $\mathbf{r}$ and $\vec{\omega}$ each represent the projection of two variables on to a surface/unit sphere in three spatial dimensions. Also worth noting is that not all possible rays starting from S_1 are modeled in the second convention, only those that strike a point in S_2 are defined.

2.1.2 Bidirectional Reflectance Model

To model the behavior of a light on our scene, we must consider the relationship between incoming and outgoing light for an incremental surface element. This function that describes redistribution of light from incident ray to outgoing radiance is known as the *bidirectional reflectance distribution function* (BRDF) and was first described by Fred Nicodemus in 1965. [4]

The BRDF is in general a 6 dimensional function, $f_r(\mathbf{r}, \vec{\omega}_o, \vec{\omega}_i)$, where $\vec{r} = r(\theta, \phi)$ denotes a point on the incident surface, and ω_o and ω_i each are scaler vectors describing of the outgoing and incoming ray angle, respectively. We can obtain the outgoing radiance from the incoming radiance according to the following relationship:

$$L_o(\mathbf{r}, \vec{\omega}_o) = \iint\limits_{\Omega_{2\pi}} f_r(\mathbf{r}, \vec{\omega}_i, \vec{\omega}_o) L_i(\mathbf{r}, \vec{\omega}_i)(\vec{\omega}_i \cdot \vec{n}) d\vec{\omega}_i \tag{2.3}$$

Transforming this into our two surface representation of radiance, we reach the following equation.

$$L_o(\mathbf{r}_2, \vec{\omega}_o) = \iint\limits_{S_1} f_r(\mathbf{r}_1\widehat{\mathbf{r}_2 - \mathbf{r}_1}, \vec{\omega}_o) L_i(\mathbf{r}_1, \mathbf{r}_2)(\widehat{\mathbf{r}_2 - \mathbf{r}_1} \cdot \vec{n}) \frac{dA_1}{||\mathbf{r}_2 - \mathbf{r}_1||^2} \tag{2.4}$$

Note that in changing the variable and integration limit, we have lost the rays included in the integrand that did not pass the surface S_1. However, for these rays, L_i is by definition zero, so the equality holds. Further projecting this radiance field onto a third surface S_3, would result in the following transformation:

$$L_o(\mathbf{r}_2, \mathbf{r}_3) = \iint\limits_{S_1} f_r(\mathbf{r}_1\widehat{\mathbf{r}_2 - \mathbf{r}_1}, \widehat{\mathbf{r}_3 - \mathbf{r}_2}) L_i(\mathbf{r}_1, \mathbf{r}_2)(\widehat{\mathbf{r}_2 - \mathbf{r}_1} \cdot \vec{n}) \frac{dA_1}{||\mathbf{r}_2 - \mathbf{r}_1||^2} \tag{2.5}$$

2.1.2.1 Specular Reflection

The BRDF is a measurable quantity for a given object or material, that can be experimentally determined by illuminating and measuring the irradiance at different surface angles [1]. However, it is also a function that has been modeled with fairly high success. One such model is known as the Torrance-Sparrow Model, first published in 1976. This model assumes that a roughened surface is composed of perfectly specular small micro facets distributed in some distribution function. [10]

Using the Torrance-Sparrow model, the BRDF of a point on a surface with local surface orientation $\vec{n}$ is given by the following expression:

$$f_{r,d}(\vec{\omega}_i, \vec{\omega}_o) = \frac{D(\vec{h})G(\vec{\omega}_i, \vec{\omega}_o)Fr(\vec{\omega}_o \cdot \vec{h})}{4(\vec{n} \cdot \vec{\omega}_i)(\vec{n} \cdot \vec{\omega}_o)} \tag{2.6}$$

where $\vec{h}$ is the half angle vector given by:

$$\vec{h} = \frac{\vec{\omega}_i + \vec{\omega}_o}{||\vec{\omega}_i + \vec{\omega}_o||} \tag{2.7}$$

Here, $D(\vec{h})$ is the Distribution of micro-facets, $G(\vec{\omega}_i, \vec{\omega}_o)$ is the Geometric Attenuation Factor to account for micro facets shadowed by other micro facets, and $Fr(\vec{\omega}_o \cdot \vec{h})$ is the Fresnel Factor given by Fresnel Equations. All three of the terms D, G, and Fr depend on the local surface orientation $\vec{n}$, and the Fresnel term Fr depends on the material's refractive index as well as the wavelength of light, but these are left implicit in the expression above.

The original Torrance-Sparrow article used a Gaussian distribution for the distribution of micro-facets. Five years later, Cook and Torrance published an updated model that takes into account wavelength and color shift, but this time using Beckmann Distribution, which is considered to give the best results without introducing any arbitrary parameters, but at the cost of increased computational demands. [6] Armed with modern high level programming languages and multi-core processors, this work uses the Beckmann Distribution Function reproduced below:

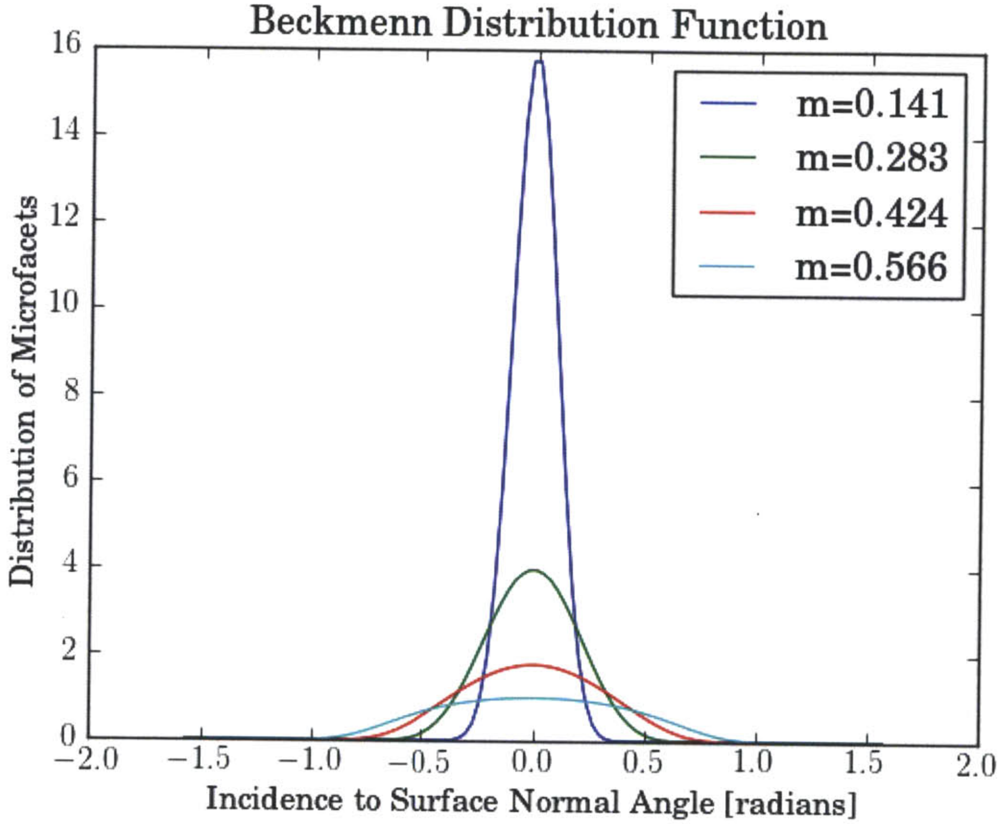

Figure 2-3: The Beckmann Distribution

$$
\begin{aligned}
D(\vec{h}) &= \frac{e^{-\frac{tan^2(cos^{-1}(\vec{h}\cdot\vec{n}))}{m^2}}}{\pi m^2(\vec{h}\cdot\vec{n})^4} \\
&= \frac{e^{-\frac{1-(\vec{h}\cdot\vec{n})^2}{(\vec{h}\cdot\vec{n})^2 m^2}}}{\pi m^2(\vec{h}\cdot\vec{n})^4}
\end{aligned} \tag{2.8}
$$

where m is the RMS slope of the micro facets, representing a metric of the roughness of the surface at that point.

2.1.2.2 Diffuse Reflection

We will model the diffuse reflections using the Lambertian reflector model, which assume an isotropic response over all viewing angles $\vec{\omega}_o$ independent of incidence angle $\vec{\omega}_i$. This is equivalent to a BRDF function as follows:

$$f_{r,s}(\vec{\omega}_o) = \frac{1}{\pi} \tag{2.9}$$

2.1.2.3 Combined Reflections

Most objects exhibit some amount of diffuse reflections and specular high lights. To model this, we will supply two parameters, k_s and k_d, that represent the portion of incident energy that is reflected through specular and diffuse mechanisms, respectively. Our final expression for BRDF will thus now be:

$$f_r(\vec{\omega}_i, \vec{\omega}_o) = k_s f_{r,s}(\vec{\omega}_i, \vec{\omega}_o) + k_d fr, d(\vec{\omega}_o) \tag{2.10}$$

2.1.3 Illumination Source

An infrared light emitting diode (IR LED) would be used as the illumination source. To fully describe a light source, we must once again use radiance fields. However, LEDs are generally modeled as point sources with a particular radiant intensity as a function of angle, i.e.: $I_e = I_e(\theta)$. LEDs are technically finite in size, but for distances that are several times larger than the dimension of the diode, (which are on the order of 1mm or less for surface mount chip LEDs), this approximation is quite accurate and the standard method of characterizing an LED. We will also define the quantity Φ_0, which represents the total optical energy emitted by the diode, given by:

$$\Phi_0 = \int_0^{2\pi} \int_0^{\frac{\pi}{2}} I_e(\theta) sin\theta d\theta d\phi \tag{2.11}$$

2.1.4 Photodetector

A photodiode will be used to detect the light reflected back from the target scene. The amount of optical power incident on the photodetector is simply the integral of the radiance across the area of the diode, across the upper hemisphere, according to the following expression:

$$\Phi_d = \iint_A \iint_{\Omega_{2\pi}} Lcos(\theta)dAd\Omega \tag{2.12}$$

Where Ω is the Solid Angle, and θ is the zenith angle in spherical coordinates. More generally, in vector notation:

$$\Phi_d = \iint_A \iint_{\Omega_{2\pi}} L(\vec{\omega} \cdot \vec{n})dAd\vec{\omega} \tag{2.13}$$

The diode photocurrent I_d is equal to the total Radiant Flux times the Responsivity, which is typically near constant in photoconductive mode.

$$I_d = R\Phi_d = \eta \frac{q}{hf} \Phi_d \tag{2.14}$$

where η is the quantum efficiency of the photodiode for a given wavelength, q is the electron charge, h is Plank's constant, and f is the frequency of the radiation.

In avalanche mode, the Responsivity is still linear, but with an additional gain of M. i.e.:

$$I_d = MR\Phi_d \tag{2.15}$$

However, in Geiger mode as used with Single Photon Avalanche Diodes (SPADs), the response is better understood as an triggering event, and does not follow the same principle. For these devices, each photon triggers a pulse, and additional circuitry is required to integrate or "count" the number of photons arrived in a certain period of time. This has the advantages of high sensitivity and intrinsic low noise, but has the disadvantage that it loses accuracy at higher incident radiant flux due to saturation of the avalanche process. The exact relation of the voltage acquired and incident radiant flux is dependent on the implementation of the trigger circuitry and

Table 2.1: Parameter Definitions for Intensity Model

Symbol	Description	Dimensionality/Units
$\mathbf{r}_e$	Point along the Emitter Surface	Position Vector
$\mathbf{r}_s$	Point along Scene Surface	Position Vector
$\mathbf{r}_s$	Point along Detector Surface	Position Vector
dA_e	Infinitesimal Area Element on the Emitter	$[m^2]$
dA_s	Infinitesimal Area Element on the Scene	$[m^2]$
dA_d	Infinitesimal Area Element on the Detector	$[m^2]$

the analog counter, but in general, they are designed such that:

$$V_{int} \propto \int \Phi_d dt \tag{2.16}$$

In either scenario, the diode is designed and used such that the diode current is proportional to the incident optical power. This current is usually then integrated using a capacitor, or converted to voltage before amplification and digitization. For the purpose of this study, we will simply assume that what ever mechanism is used at the detector and signal conditioning circuits, the optical power is the intrinsic measure that the acquired signal is representing. Thus, we will abstract the photodetector as simply a device that measures optical power.

2.2 Intensity Model

In assembling these results, we will define the following variables.

We will first consider a general Illumination Source, characterized by the 4D Radiance Field $L_i(\mathbf{r}_e, \mathbf{r}_s)$, that is occupying a surface $E = \mathbf{r}_e$, projecting light on to the surface $S = \mathbf{r}_s$. In this setup, we have:

$$L_o(\mathbf{r}_s, \mathbf{r}_d) = \iint\limits_E f_r(\mathbf{r}_e\widehat{\mathbf{r}_s - \mathbf{r}}_e, \widehat{\mathbf{r}_s - \mathbf{r}}_d) L_i(\mathbf{r}_e, \mathbf{r}_s)(\widehat{\mathbf{r}_s - \mathbf{r}}_e \cdot \vec{n}) \frac{dA_e}{||\mathbf{r}_s - \mathbf{r}_e||^2} \tag{2.17}$$

$$\Phi_d = \iint\limits_D \iint\limits_{\Omega_{2\pi}} L_o(\mathbf{r}_s, \mathbf{r}_d)(\vec{\omega}_o \cdot \hat{n}_d) d\vec{\omega}_o dA_d \tag{2.18}$$

$$= \iint\limits_D \iint\limits_S L_o(\mathbf{r}_s, \mathbf{r}_d)(\widehat{\mathbf{r}_s - \mathbf{r}}_d \cdot \hat{n}_d) \frac{dA_s}{||\mathbf{r}_s - \mathbf{r}_d||^2} dA_d \tag{2.19}$$

This involves three surface integrals, and is both computation intensive and too complex to be informative for analysis. For a sufficiently small emitters we can make the approximations as the source as a point source characterized by Radiant Intensity $I_e(\vec{\omega}) = I_e(\widehat{\mathbf{r}_s - \mathbf{r}}_e)$ centered at $\mathbf{r}_e = \mathbf{R}_E$ with an area A_E.

$$L_i(\mathbf{r}_e, \mathbf{r}_s) dA_e = I_e(\widehat{\mathbf{r}_s - \mathbf{r}}_e)\delta(\mathbf{r}_e - \mathbf{R}_E) \tag{2.20}$$

This simplifies Equation 2.17- 2.18 down to:

$$L_o(\mathbf{r}_s, \mathbf{r}_d) = f_r(\mathbf{r}_e\widehat{\mathbf{r}_s - \mathbf{r}}_e, \widehat{\mathbf{r}_s - \mathbf{r}}_d) I_e(\widehat{\mathbf{r}_s - \mathbf{R}}_E) \frac{(\widehat{\mathbf{r}_s - \mathbf{r}}_e \cdot \vec{n})}{||\mathbf{r}_s - \mathbf{R}_E||^2} \tag{2.21}$$

$$\Phi_d = \iint\limits_D \iint\limits_S f_r(\mathbf{r}_e\widehat{\mathbf{r}_s - \mathbf{r}}_e, \widehat{\mathbf{r}_s - \mathbf{r}}_d) I_e(\widehat{\mathbf{r}_s - \mathbf{R}}_E) \frac{dA_s}{||\mathbf{r}_s - \mathbf{R}_E||^2} (\widehat{\mathbf{r}_s - \mathbf{r}}_e \cdot \vec{n}) \frac{dA_d}{||\mathbf{r}_s - \mathbf{R}_D||^2} (\widehat{\mathbf{r}_s - \mathbf{r}}_d \cdot \tag{2.22}$$

Where we observe a nice bit of symmetry. To further simplify the expression, we can model the detector as a "point detector" centered at $\mathbf{R}_D$ with area A_D and mean surface normal $\hat{N}_d$, by making the following approximation.

$$dA_d(\mathbf{r}_d) = A_D \delta(\mathbf{r}_d - \mathbf{R}_D) \hat{N}_d \tag{2.23}$$

Making these approximations, we arrive to the following formulas:

$$\Phi_d = \iint\limits_S f_r(\mathbf{r}_s, \widehat{\mathbf{r}_s - \mathbf{R}_E}, \widehat{\mathbf{r}_s - \mathbf{R}_D}) I_e(\widehat{\mathbf{r}_s - \mathbf{R}_E}) \frac{dA_s}{||\mathbf{r}_s - \mathbf{R}_E||^2} (\widehat{\mathbf{r}_s - \mathbf{R}_E} \cdot \vec{n}) \frac{A_D}{||\mathbf{r}_s - \mathbf{R}_D||^2} (\widehat{\mathbf{r}_s - \mathbf{R}_D} \cdot \hat{N}_d) \tag{2.24}$$

For clarity, we will define the following displacement vectors:

$$\mathbf{r}_i = \mathbf{r}_s - \mathbf{R}_E \tag{2.25}$$

$$\mathbf{r}_o = \mathbf{r}_s - \mathbf{R}_D \tag{2.26}$$

Substituting this, we obtain:

$$\Phi_d = \iint\limits_S f_r(\mathbf{r}_s, \hat{\mathbf{r}}_i, \hat{\mathbf{r}}_o) I_e(\hat{\mathbf{r}}_i) \frac{dA_s(\hat{\mathbf{r}}_i \cdot \hat{n})}{||\mathbf{r}_i||^2} \frac{A_D(\hat{\mathbf{r}}_o \cdot \hat{N}_d)}{||\mathbf{r}_o||^2} \tag{2.27}$$

For most time-of-flight systems, the emitter and detector are close to each other, which leads us to the approximation $\mathbf{r} = \mathbf{r}_i = \mathbf{r}_o$, giving us:

$$\Phi_d = \iint\limits_S f_r(\mathbf{r}, \hat{\mathbf{r}}, \hat{\mathbf{r}}) I_e(\hat{\mathbf{r}}) \frac{dA_s(\hat{\mathbf{r}} \cdot \hat{n}) A_D(\hat{\mathbf{r}} \cdot \hat{N}_d)}{||\mathbf{r}||^4} \tag{2.28}$$

2.3 Time Dependancy

Light travels at the speed of light, incurring a time delay between when a ray is emitted from a source and is detected back at the source. This time delay is the basis of all Time-Of-Flight Systems. For Time-Of-Flight Systems, this effect must be taken into effect.

2.3.1 Wave Propagation Model

Light travels at a finite speed through any medium. If a ray of light is emitted with waveform $f(t)$ is emitted at a point $\mathbf{r}_0$, the same ray observed at point $\mathbf{r}_1$ will have the waveform:

$$f\left(t - \frac{||\mathbf{r}_1 - \mathbf{r}_0||}{c}\right) \tag{2.29}$$

To combining this with our model from Equation 2.27, we will represent the radiant intensity of a illumination source is represented as a function of time, such that $I_e = I_0(\vec{\omega})f(t)$. Now, the flux at the detector will be:

$$\Phi_d(t) = \iint\limits_S d\Phi_d(\mathbf{r}_s) f\left(t - \frac{||r_i|| + ||r_o||}{c}\right) \tag{2.30}$$

where,

$$d\Phi_d(\mathbf{r}_s) = f_r(\mathbf{r}_s, \hat{\mathbf{r}}_i, \hat{\mathbf{r}}_o) I_0(\hat{\mathbf{r}}_i) \frac{dA_s(\hat{\mathbf{r}}_i \cdot \hat{n})}{||\mathbf{r}_i||^2} \frac{A_D(\hat{\mathbf{r}}_o \cdot \hat{N}_d)}{||\mathbf{r}_o||^2} \tag{2.31}$$

2.3.2 Measuring Time-Of-Flight

As introduced in Chapter 1, there are several methods for measuring the time of flight. Here, we will focus on "Indirect" Time-Of-Flight methods. There are two main categories for I-TOF systems, those that use Pulsed Light and those that use a Sine Wave Modulation.

2.3.2.1 Pulsed Light

This is the most common approach for 3D time-of-flight cameras, taking two or more shutter windows and using the ratio to determine the time of flight. The time-of-flight is related to the distance as:

$$d = \frac{c\Delta T}{2} \tag{2.32}$$

This is implemented by using a square pulse for the waveform, with pulse width T_p. This signal is then integrated over two or more separate windows, and the ratio is used to determine the time.

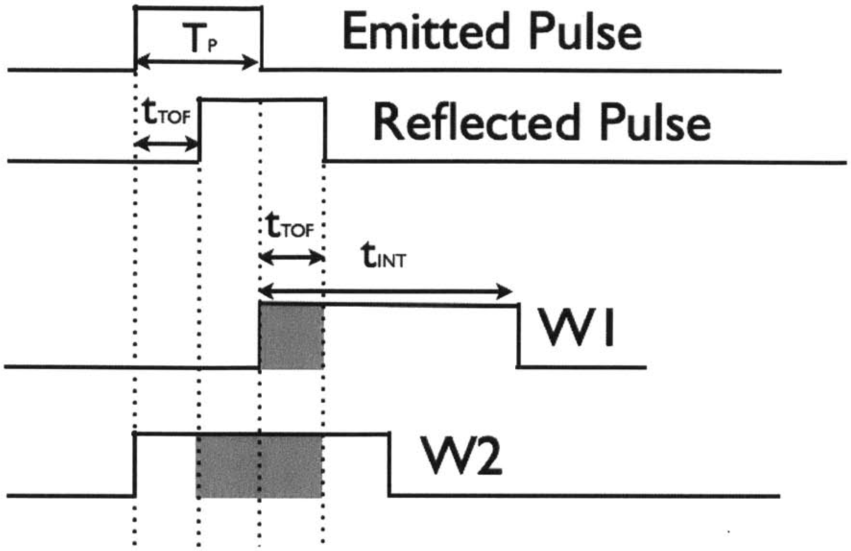

Figure 2-4: Window Scheme for Pulsed TOF

Using the windowing scheme shown in Figure 2-4:

$$\begin{aligned} W_1 &= \int_{T_1}^{T_1+T_{int}} \Phi(t)dt \\ &= \iint\limits_S \frac{||\mathbf{r}_i|| + ||\mathbf{r}_o||}{c} d\Phi_d(\mathbf{r}_s) \end{aligned} \tag{2.33}$$

$$\begin{aligned} W_2 &= \int_{T_0}^{T_0+T_{int}} \Phi(t)dt \\ &= \iint\limits_S T_p d\Phi_d(\mathbf{r}_s) \end{aligned} \tag{2.34}$$

The time of flight is computed from these two windows as following:

$$\begin{aligned} \Delta t &= T_p \frac{W_1}{W_2} \\ &= \frac{\iint\limits_S d\Phi_d(\mathbf{r}_s) \frac{||\mathbf{r}_i|| + ||\mathbf{r}_o||}{c}}{\iint\limits_S d\Phi_d(\mathbf{r}_s)} \end{aligned} \tag{2.35}$$

As can be seen, each component of light adds linearly, and the resultant time of flight is effectively the weighted average of time of flights from all the paths from the emitter to the detector. Converting this to distance, we get:

$$d = \frac{c\Delta t}{2} = \frac{\iint\limits_S d\Phi_d(\mathbf{r}_s)(||\mathbf{r}_i|| + ||\mathbf{r}_o||)}{2\iint\limits_S d\Phi_d(\mathbf{r}_s)} \tag{2.36}$$

2.3.2.2 Sine Wave Modulation

An alternative to Pulsed Time-of-Flight is a technique referred as Sine Wave Modulation (SWM). This technique is similar to Phase Modulation used in RF applications, but instead of modulating the signal with a signal to be transmitted, optical channel is the modulator. Unlike pulsed light modulation which extracts the time-of-flight using ratios between windows, this technique extracts phase delay from trigonometric identities. This phase delay $\Delta\phi$ is related to the distance according to the following formula:

$$d = \frac{c}{4\pi f}\Delta\phi \tag{2.37}$$

The main advantages that sine wave modulation has are two fold. This first is that the bandwidth requirements and time domain behavior is easily analyzed due to the availability of Sinusoidal Steady State analysis as well as frequency domain techniques. The second is that filtering and other techniques common in RF systems can be readily applied in the signal chain to improve SNR. However, their is a slight complication in interpreting the signals, due to the non-linear nature on the conversion.

The system is constructed by emitting an optical signal modulated with a sine wave or similarly narrow band signal with a frequency of f, or a radial frequency $\omega_m = 2\pi f$. The reflected signal is detected and demodulated using a similarly narrow band signal, typically a square wave, and the result is sampled and quantized. By using two demodulators 90 degrees apart, one can obtain both the amplitude and phase information. With $f(t) = cos(\omega_m t + \phi_0)$, the two demodulation signals are

$cos(\omega_m t)$ and $sin(\omega_m t)$.

$$\begin{aligned}
x_I &= \int_T \Phi(t) cos(\omega_m t) dt \\
&= \iint_S \int_T d\Phi_d(\mathbf{r}_s) cos(\omega_m t) cos\left(\omega_m \left(t - \frac{||\mathbf{r}_i|| + ||\mathbf{r}_o||}{c}\right) + \phi_0\right) dt \\
&= \iint_S d\Phi_d(\mathbf{r}_s) \pi cos\left(\omega_m \left(\frac{||\mathbf{r}_i|| + ||\mathbf{r}_o||}{c}\right) - \phi_0\right) \qquad (2.38) \\
x_Q &= \int_T \Phi(t) sin(\omega_m t) dt \\
&= \iint_S \int_T d\Phi_d(\mathbf{r}_s) sin(\omega_m t) cos\left(\omega_m \left(t - \frac{||\mathbf{r}_i|| + ||\mathbf{r}_o||}{c}\right) + \phi_0\right) dt \\
&= \iint_S d\Phi_d(\mathbf{r}_s) \pi sin\left(\omega_m \left(\frac{||\mathbf{r}_i|| + ||\mathbf{r}_o||}{c}\right) - \phi_0\right) \qquad (2.39)
\end{aligned}$$

The phase of the signal is computed as:

$$\Delta\phi = tan^{-1}\left(\frac{x_I}{x_Q}\right) + \phi_0 \qquad (2.40)$$

We will abstract this implementation using complex exponentials, letting $x_I = \Re(x)$, $x_Q = \Im(x)$:

$$\begin{aligned}
x &= \iint_S d\Phi_d(\mathbf{r}_s) \pi e^{j(\frac{\omega_m}{c}(||\mathbf{r}_i||+||\mathbf{r}_o||)-\phi_0)} \\
\Delta\phi &= \angle(x) + \phi_0 \qquad (2.41)
\end{aligned}$$

2.4 Simulation and Analysis of Simple Scenes

A numerical simulation model implementing Equation 2.24, 2.35, and 2.41 was written in Python. The following section finds analytic solutions to the model for simple scenes, and provides a comparison to simulation results to verify the simulation results.

2.4.1 Perfect Sphere, Point Source

We will first study the special case for the following conditions:

- Emitter is an ideal point source with uniform distribution.

  i.e. $I_e(\vec{\omega}) = I_0 = \frac{\Phi_0}{2\pi}$, where Φ_0 is the total optical power emitted from the illumination source.

- The scene is a perfectly diffuse shell of constant radius r.

$$\mathbf{r} = (r, \theta, \phi) \tag{2.42}$$

$$||\mathbf{r}|| = r \tag{2.43}$$

$$dA = r^2 sin\theta d\theta d\phi \tag{2.44}$$

$$f_r(\mathbf{r}, \vec{\omega}_i, \vec{\omega}_o) = \frac{1}{\pi} \tag{2.45}$$

$$\hat{n} = \hat{\mathbf{r}} \tag{2.46}$$

- Emitter and the Detector are coincident, and are oriented in the XY plane: i.e.:

$$R_E = R_D \tag{2.47}$$

$$\hat{N_d} = \hat{z} \tag{2.48}$$

$$\hat{N_d} \cdot \hat{\mathbf{r}} = \cos(\theta) \tag{2.49}$$

In this scenario, Equation 2.24 simplifies to the following:

$$\begin{aligned} \Phi_d &= \int_{-\pi}^{\pi} \int_{0}^{\frac{\pi}{2}} \frac{\Phi_0}{2\pi} A_D \frac{1}{\pi} \frac{cos\theta}{r^2} \frac{r^2 sin\theta d\theta \phi}{r^2} \\ &= \frac{1}{2\pi} \Phi_0 A_D \frac{1}{r^2} \end{aligned} \tag{2.50}$$

The time of flight is computed as:

$$
\begin{aligned}
\Delta t &= \frac{\iint\limits_S \int_{-\pi}^{\pi} \int_0^{\frac{\pi}{2}} \frac{\Phi_0}{2\pi} A_D \frac{cos\theta}{r^2} \frac{r^2 sin\theta d\theta\phi}{r^2} \left(\frac{2r}{c}\right)}{\iint\limits_S \int_{-\pi}^{\pi} \int_0^{\frac{\pi}{2}} \frac{\Phi_0}{2\pi} A_D \frac{cos\theta}{r^2} \frac{r^2 sin\theta d\theta\phi}{r^2}} \\
&= \frac{\frac{1}{2}\Phi_0 A_D \frac{1}{r^2} \left(\frac{2r}{c}\right)}{\frac{1}{2}\Phi_0 A_D \frac{1}{r^2}} \\
&= \frac{2r}{c} \qquad (2.51)
\end{aligned}
$$

Using the simulation code, the field of view of the system is divided into a $N \times N$ array of facets, and the contribution of the first reflection off of each facet is computed and added up to deliver the total optical power on the diode. The simulation results are summarized in the figures 2-5 through 2-9. As can be seen quite clearly, the simulation and analytical results match quite well, save a small constant offset due to the discretization of the scene, which diminishes as the simulation resolution is increases.

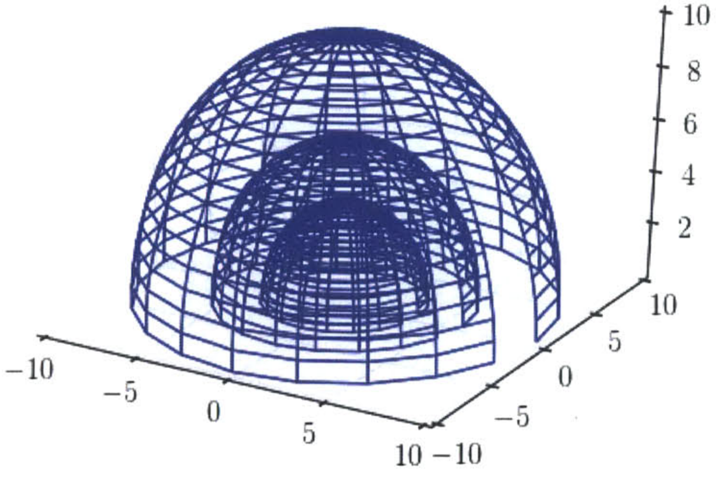

Figure 2-5: Facet Array of Spherical Shells for N=20

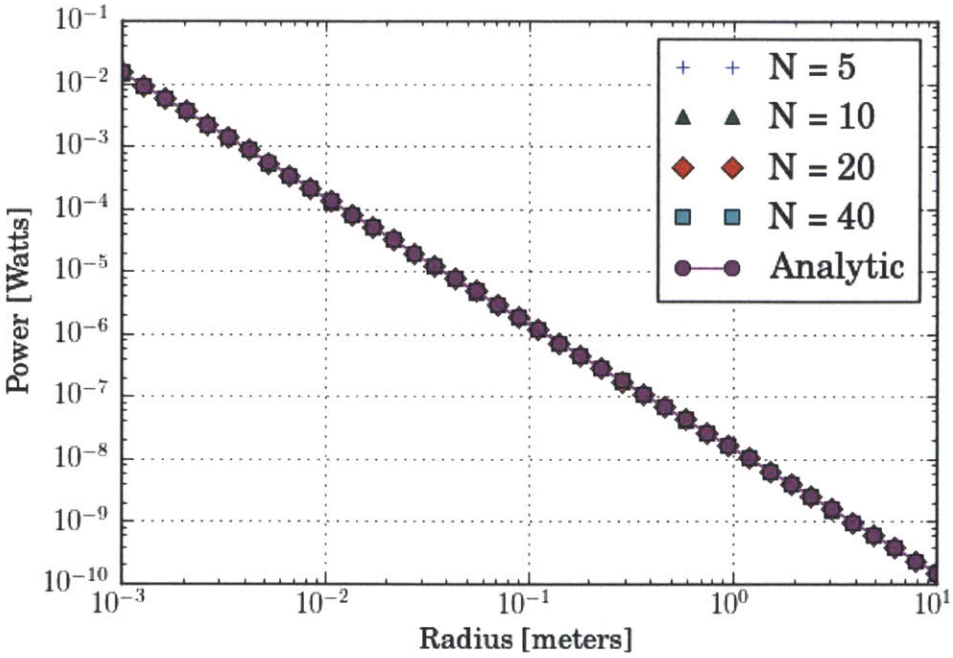

Figure 2-6: Distance v.s. Intensity for a Spherical Shell

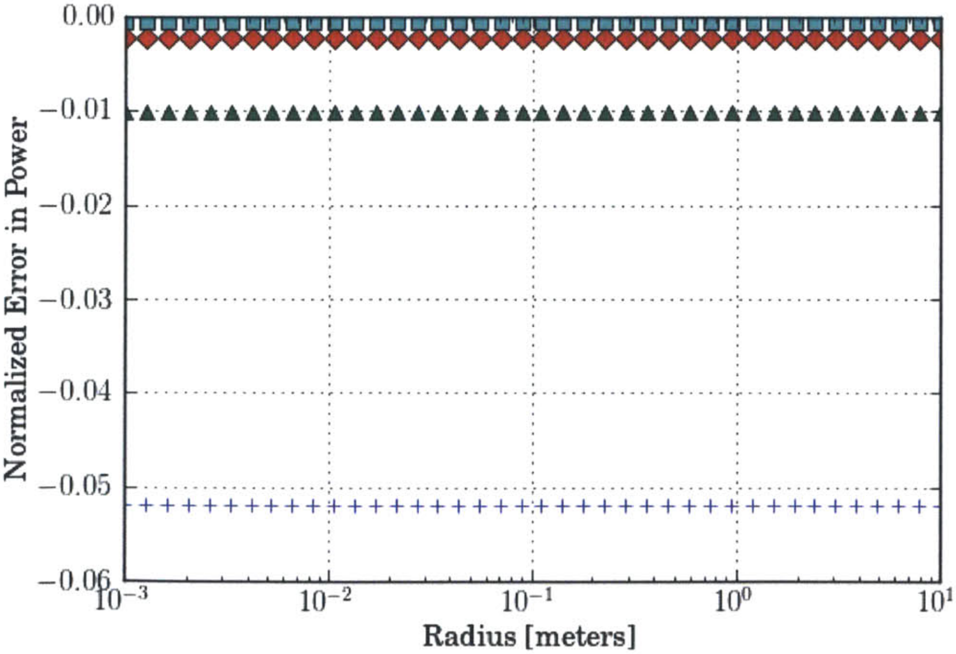

Figure 2-7: Distance v.s. Simulation Error in Intensity for a Spherical Shell

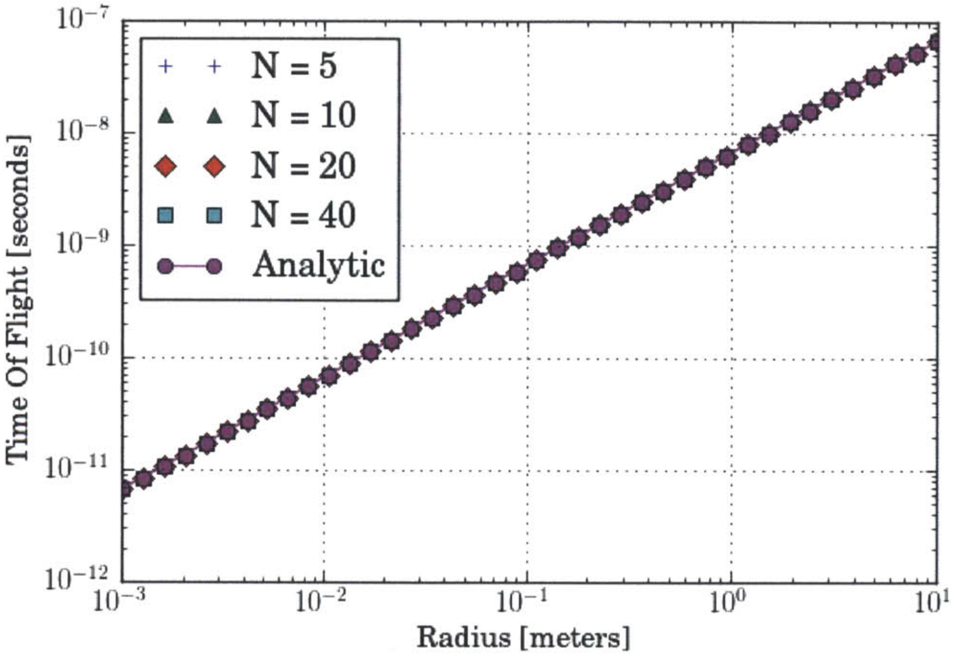

Figure 2-8: Distance v.s. TOF for a Spherical Shell

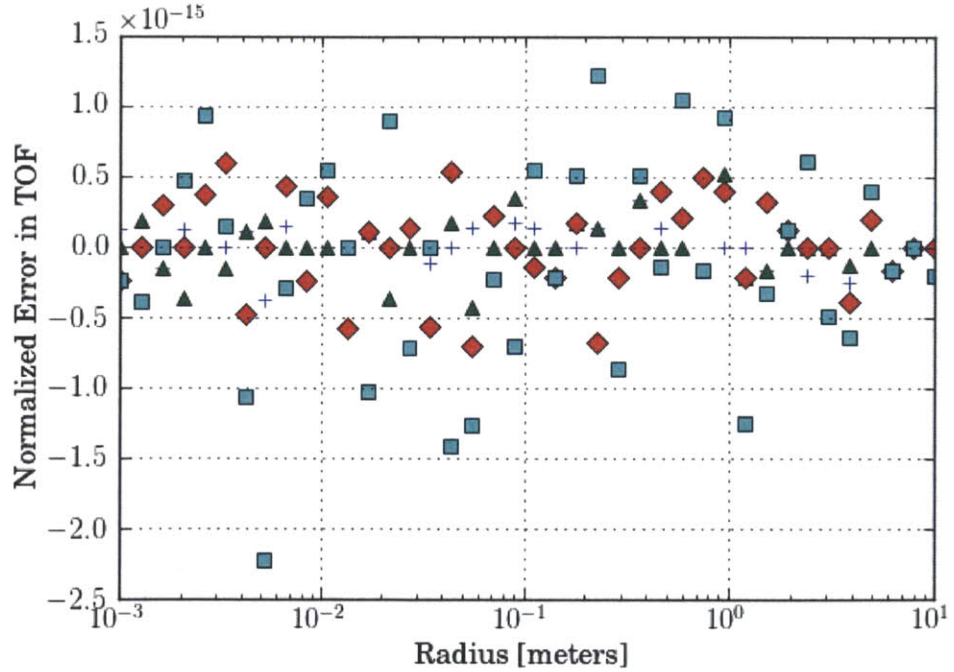

Figure 2-9: Distance v.s. Simulation Error in TOF for a Spherical Shell

2.4.2 Infinite Plane, Point Source

We will look at another simple scene that can be verified analytically. We will continue using the same conditions for the following:

- Emitter is an ideal point source with uniform distribution.
  i.e. $I_e(\vec{\omega}) = I_0 = \frac{\Phi_0}{2\pi}$, where Φ_0 is the total optical power emitted from the illumination source.

But instead of a sphere, we will use a infinite plane of diffuse material a set distance d away form the plane of the sensor.

$$\mathbf{r} = \left(\frac{d}{\cos(\theta)}, \theta, \phi\right) \tag{2.52}$$

$$||\mathbf{r}|| = \frac{d}{\cos(\theta)} \tag{2.53}$$

$$dA = r^2 sin\theta d\theta d\phi = \frac{d^2 sin\theta d\theta d\phi}{\cos^2(\theta)} \tag{2.54}$$

$$f_r(\mathbf{r}, \vec{\omega}_i, \vec{\omega}_o) = \frac{1}{\pi} \tag{2.55}$$

$$\hat{n} = \hat{z} \tag{2.56}$$

The amplitude of the detected signal is now given by:

$$\begin{aligned}
\Phi_d &= \int_{-\pi}^{\pi}\int_{0}^{\frac{\pi}{2}} \frac{\Phi_0}{2\pi} A_D \frac{1}{\pi} \frac{cos^2\theta}{r^2} \frac{r^2 sin\theta d\theta d\phi}{r^2} \\
&= \int_{-\pi}^{\pi}\int_{0}^{\frac{\pi}{2}} \frac{\Phi_0}{2\pi} A_D \frac{1}{\pi} \frac{cos^4\theta sin\theta d\theta d\phi}{d^2} \\
&= \frac{\Phi_0}{5\pi} A_D \frac{1}{d^2}
\end{aligned} \tag{2.57}$$

The time of flight is computed as:

$$\begin{aligned}\Delta t &= \frac{\iint\limits_S \int_{-\pi}^{\pi} \int_0^{\frac{\pi}{2}} \frac{\Phi_0}{2\pi} A_D \frac{cos^2\theta}{r^2} \frac{r^2 sin\theta d\theta\phi}{r^2} \left(\frac{2r}{c}\right)}{\iint\limits_S \int_{-\pi}^{\pi} \int_0^{\frac{\pi}{2}} \frac{\Phi_0}{2\pi} A_D \frac{cos^2\theta}{r^2} \frac{r^2 sin\theta d\theta\phi}{r^2}} \\ &= \frac{\frac{1}{5\pi} \Phi_0 A_D \frac{1}{d^2} \left(\frac{2d}{c}\right)}{\frac{1}{4\pi} \Phi_0 A_D \frac{1}{d^2}} \\ &= \frac{5}{2}\frac{d}{c} \end{aligned} \tag{2.58}$$

The simulation results summarized in figures 2-10 through 2-13 show a slight systematic error in the time of flight, most likely due to the fact that at the boundary of the field of view of the sensor (which is ill behaved for a numerical simulation) theoretically contributes an infinite distance, converging to a finite error despite the the $1/r^2$ dependance.

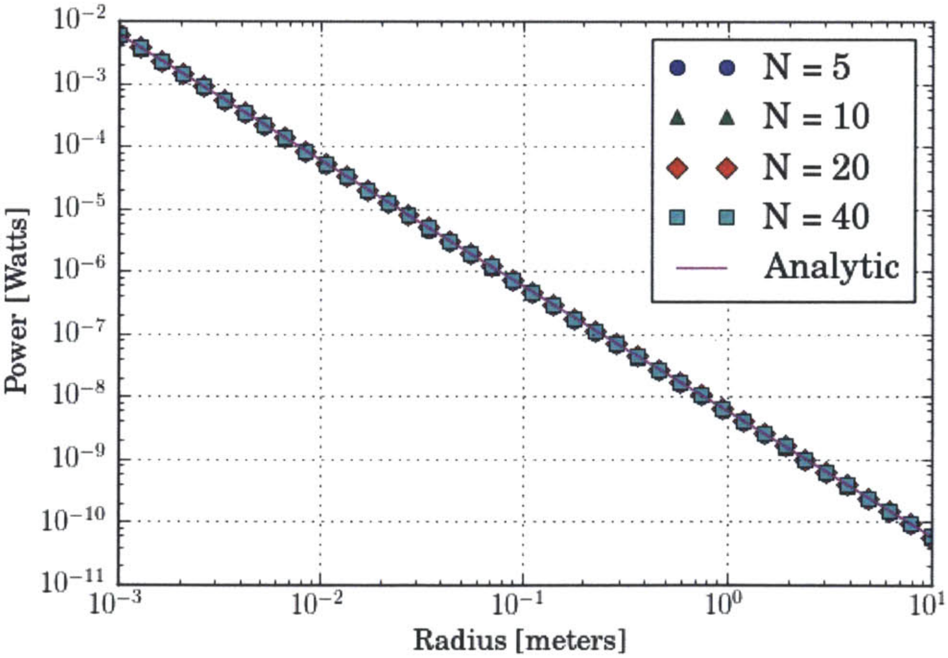

Figure 2-10: Distance v.s. Intensity for an Infinite Plane

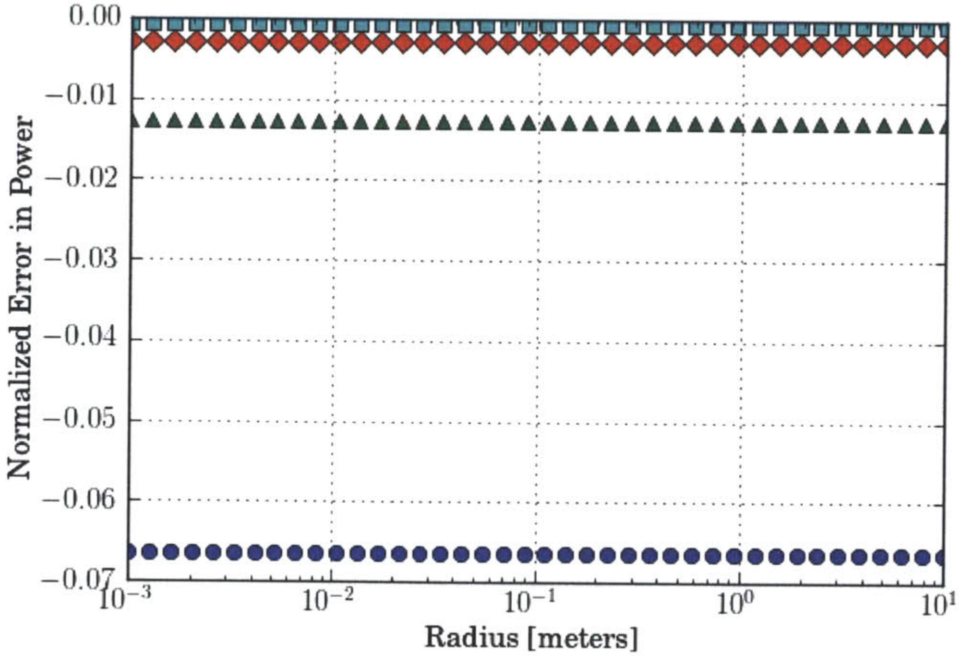

Figure 2-11: Distance v.s. Simulation Error in Intensity for an Infinite Plane

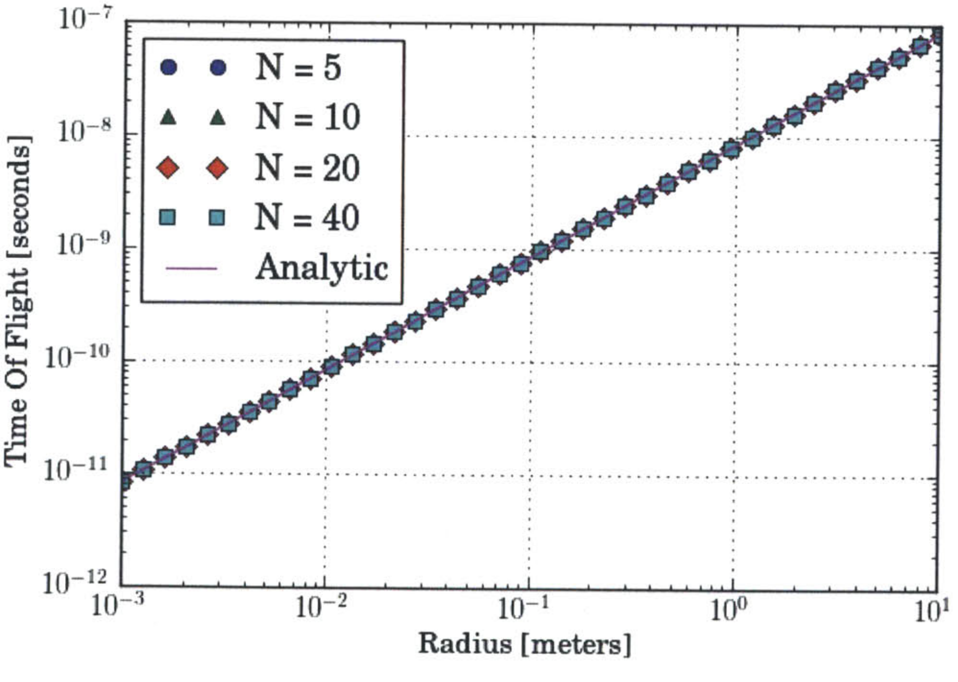

Figure 2-12: Distance v.s. TOF for a Infinite Plane

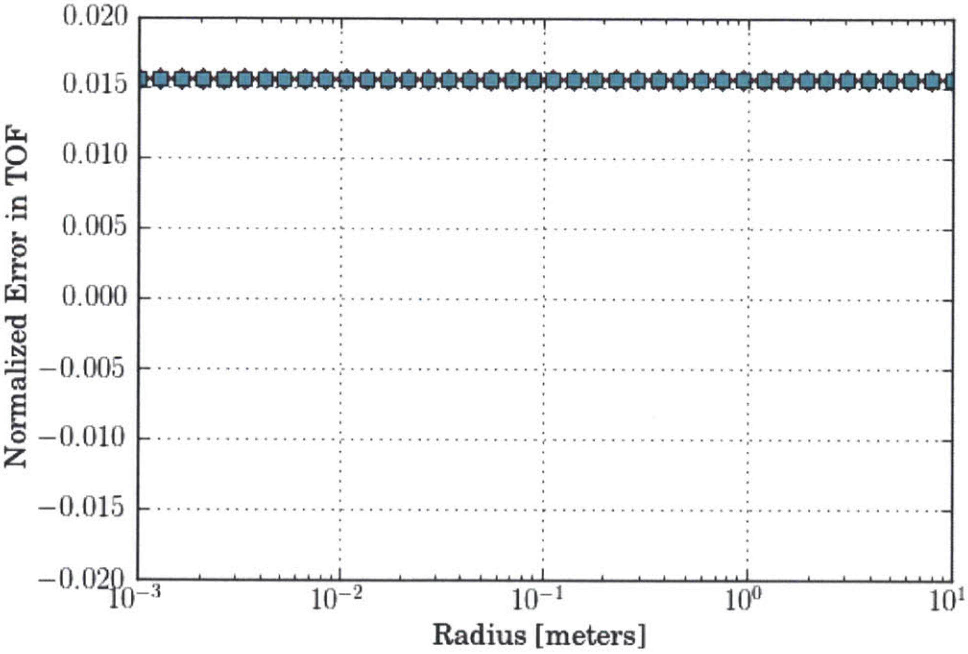

Figure 2-13: Distance v.s. Simulation Error in TOF for an Infinite Plane

Chapter 3

Parameterizing Objects in Hybrid Intensity/Time-Of-Flight Signals

This chapter will discuss how we can extract physical attributes of real scenes from signals obtained from a system as characterized in Chapter 2. In principle, the same signal from the detector can originate from an infinite possibility of scenes. However, by making certain assumptions about typical scenes, we can extract useful information from the signal obtained from our detector. In order to accomplish this, we must first describe the signal using a finite number of sensible parameters. Our ultimate goal will be to estimate these parameters, obtaining a description of the optical scene.

3.1 Parametrizing Objects

In this section we will use the models developed in Chapter 2 to parameterize Time-Of-Flight signals. The base assumption that we will make here, is that the scene is composed of distinct "objects". Physical objects tend to be fairly uniform in their surface texture, refractive index, and surface orientation, and most importantly, are localized in space and do not change size. Ultimately, these objects are what we would like to be able to recognize and identify. Therefore, it is critical that we understand how a typical object behaves in a Time-Of-Flight systems.

3.1.1 Effective Distance

The first parameter to introduce is the *Effective Distance*, which we will denote simply as r_e.

The effective distance of an object is defined as the distance needed for a point reflector to result in the same time-of-flight computed from a signal reflected from an entire object. Let us recall the results of converting our signal from the whole scene to a single Time-Of-Flight in Equations 2.35 for Pulsed Time-Of-Flight, and 2.41, for Sine Wave Modulated Time-Of-Flight systems. For simplicity, let us briefly focus on Pulsed Time-Of-Flight, whose distance expression is reproduced below:

$$d = \frac{c\Delta t}{2} = \frac{\iint\limits_S d\Phi_d(\mathbf{r}_s)(||\mathbf{r}_i|| + ||\mathbf{r}_o||)}{2\iint\limits_S d\Phi_d(\mathbf{r}_s)} \tag{3.1}$$

We will define r_e as the application of the above equations over the object's projected area, O, and obtain:

$$r_e = \frac{c\Delta t}{2} = \frac{\iint\limits_O d\Phi_{obj}(\mathbf{r}_O)(||\mathbf{r}_i|| + ||\mathbf{r}_o||)}{2\iint\limits_O d\Phi_{obj}(\mathbf{r}_s)} \tag{3.2}$$

The effective distance is simply half of the optical path length:

$$\begin{aligned} r_e = \frac{d}{2} &= \frac{\iint\limits_O d\Phi_{obj}(\mathbf{r}_s)(||\mathbf{r}_i|| + ||\mathbf{r}_o||)}{2\iint\limits_O d\Phi_{obj}(\mathbf{r}_s)} \\ &= \frac{\iint\limits_O r d\Phi_{obj}(\mathbf{r})}{\iint\limits_S d\Phi_{obj}(\mathbf{r})} \end{aligned} \tag{3.3}$$

As can be seen, this effective distance is effectively the weighted average of the distance of the facets on the object reflecting the illumination back at the sensor.

This may or may not agree with what a person may intuitively perceive as the distance between the sensor and the target object, but it is nonetheless unique for any particular geometry. This definition of *effective distance* is the natural measure to describe an object for a time of flight system with a wide field of view, since it is the direct extension of interpretation of time of flight measurement for a narrow field of view LIDAR or 3D TOF camera.

Let us return to the infinite plane that we examined in Chapter 2. On the infinite plane, $r = z/cos(\theta)$, where z is the distance between the object plane and emitter/detector plane. Earlier, we had assumed a uniform illumination source, but we will now let it be a general illumination source with radiant intensity $I_e(\theta)$. Assuming the emitter and detector are sufficiently close, (i.e. $||\mathbf{r}_i|| = ||\mathbf{r}_o|| = r$), uniform surface material and smoothness, and radially symmetric profile, every term can be described by the zenith angle θ, and the expression becomes:

$$\begin{aligned} r_e &= \frac{\int_0^{2\pi}\int_0^{\frac{\pi}{2}} f_r(\theta)I_e(\theta)\frac{r^2 sin\theta d\theta d\phi(cos\theta)}{r^2}\frac{A_D(cos\theta)}{r^2}r}{\int_0^{2\pi}\int_0^{\frac{\pi}{2}} f_r(\theta)I_e(\theta)\frac{r^2 sin\theta d\theta d\phi(cos\theta)}{r^2}\frac{A_D(cos\theta)}{r^2}} \\ &= \frac{\int_0^{2\pi}\int_0^{\frac{\pi}{2}} f_r(\theta)I_e(\theta) sin\theta d\theta d\phi(cos\theta)\frac{A_D(cos^3\theta)}{z^2}\frac{z}{cos\theta}}{\int_0^{2\pi}\int_0^{\frac{\pi}{2}} f_r(\theta)I_e(\theta) sin\theta d\theta d\phi(cos\theta)\frac{A_D(cos^3\theta)}{z^2}} \\ &= z\frac{\int_0^{\frac{\pi}{2}} f_r(\theta)I_e(\theta)\cos^3\theta\sin\theta d\theta}{\int_0^{\frac{\pi}{2}} f_r(\theta)I_e(\theta)\cos^4\theta\sin\theta d\theta} \end{aligned} \tag{3.4}$$

For an ideal lambertian reflector and a point source, f_r and I_e are both constants, simplifying this further to:

$$\begin{aligned} r_e &= z\frac{\int_0^{\frac{\pi}{2}}\cos^3\theta\sin\theta d\theta}{\int_0^{\frac{\pi}{2}}\cos^4\theta\sin\theta d\theta} \\ &= \frac{5}{4}z \end{aligned} \tag{3.5}$$

If the source has an lambertian illumination profile, there will be another factor of $\cos\theta$ in both integrands, resulting in an effective distance of $\frac{8}{7}z$. If we approximate narrow Illumination profiles as powers of $\cos\theta$, we see that as narrower illumination profiles converge towards the effective distance equaling the plane to plane distance. This is consistent with our understanding of a TOF system with a narrow field of view such as a laser range finder, in that the distance computed from the time-of-flight information becomes the point to point distance between the sensor and the spot illuminated by the laser.

Real objects are finite in size, and will behave somewhat between an infinite plane and a point reflector. For a circular disk of radius a, if the distance between the object plane and emitter/detector plane is greater than the radius (i.e. $z >> a$), the effective distance of the object would be that of a point reflector. If the distance between the object plane and emitter/detector plane is small compared to the disk radius (i.e. $z << a$), the effective distance of the object approximates that of an infinite plane. The exact solutions is given by the solution to the equation:

$$r_e = z \frac{\int_0^{\arctan\left(\frac{a}{z}\right)} f_r(\theta) I_e(\theta) \cos^3\theta \sin\theta d\theta}{\int_0^{\arctan\left(\frac{a}{z}\right)} f_r(\theta) I_e(\theta) \cos^4\theta \sin\theta d\theta} \tag{3.6}$$

Table 3.1 summarizes this trend.

3.1.2 Inverse Squared and Inversed Fourth Laws

We will now focus on the relationship between the effective distance r_e and the intensity of the signal contributed from the object.

In Chapter 2, we studied two particular examples of idealized objects, a hemisphere, and an infinite plane. For both of these objects, we saw that the intensity of the detected signal decayed as an inverse square law. Mean while, we from equation 2.28 that each differential surface element contributes as an inverse quartic. This behavior can be generalized to large and small objects, respectively. For significantly large objects, an incremental change in distance will proportionately increase the area of the object illuminated by the emitter, resulting in minimal energy lost in the emis-

Table 3.1: Effective Distance for Various Illumination Profiles

Illum. Profile	Effective Distance		
I_e	$z << a$	$z >> a$	Exact Solution
$\frac{\Phi_0}{2\pi}$	$\frac{5}{4}z$	z	$\frac{5}{4}z\left(\frac{(z^2+a^2)^{\frac{5}{2}}-z^4(z^2+a^2)^{\frac{1}{2}}}{(z^2+a^2)^{\frac{5}{2}}-z^5}\right)$
$\frac{\Phi_0}{\pi}\cos\theta$	$\frac{6}{5}z$	z	$\frac{6}{5}z\left(\frac{(z^2+a^2)^{\frac{6}{2}}-z^5(z^2+a^2)^{\frac{1}{2}}}{(z^2+a^2)^{\frac{6}{2}}-z^6}\right)$
$\frac{(N+1)\Phi_0}{2\pi}\cos^N\theta$	$\frac{N+5}{N+4}z$	z	$\frac{N+5}{N+4}z\left(\frac{(z^2+a^2)^{\frac{N+5}{2}}-z^{N+4}(z^2+a^2)^{\frac{1}{2}}}{(z^2+a^2)^{\frac{N+5}{2}}-z^{N+5}}\right)$
$\frac{\Phi_0\delta(\theta)}{2\pi}$ *	z	z	z
$\frac{(\frac{\pi}{2}-\theta)}{\pi(\pi-2)}\Phi_0$	$\frac{96\pi-128}{45\pi}z$	z	**See Below

$$*\ \frac{\Phi_0\delta(\theta)}{2\pi} = \lim_{N\to\infty}\frac{(N+1)\Phi_0}{2\pi}\cos^N\theta$$

$$**\ \frac{-16}{9}\,\frac{\left(3\pi z^3\sqrt{\frac{z^2+a^2}{z^2}}+3\pi z\sqrt{\frac{z^2+a^2}{z^2}}a^2-3\pi z^3+6\arctan(\frac{a}{z})z^3-6az^2-4a^3\right)(z^2+a^2)}{\sqrt{\frac{z^2+a^2}{z^2}}\left(-8\pi a^2z^2-4\pi a^4-5\arctan(\frac{a}{z})z^4+5az^3+3a^3z+6\arctan(\frac{a}{z})z^2a^2+3\arctan(\frac{a}{z})a^4\right)}$$

sion to object illumination. There is still an inverse square law due to the projection of the reflected light field onto the detector area.

For small objects, an incremental change in distance will result in a no change in illuminated area, but the solid angle that the object occupies will decrease as an inverse square. The loss of optical flux through the vacant space is causes an inverse square term, which combined with the inverse square term associated to the loss of the detector, result in an signal intensity proportional to $\frac{1}{r_e^4}$.

However, real objects are typically somewhat in between the two extremes. For example, for a detection range of $10cm$ to $2m$, any object with a dimension in the same range is likely to exhibit both or an "in between" behavior in significant portions of the detection range.

3.1.3 Analytic Examples

Let us consider an ideal lambertian reflector shaped as a circular disk of radius a. Then, our bidirectional reflectance f_r is independent of incident and outgoing angle. $f_r = \frac{1}{\pi}$. We will once again assume a point source, $I_e = \frac{\Phi_0}{2\pi}$, and then extend the analysis to other distributions. Along the object surface, $r = \frac{z}{cos(\theta)}$. and the object is defined for $0 \leq \theta \leq \arctan(\frac{a}{z})$. Solving for the flux using Equation 2.24, we obtain:

$$\begin{aligned}
\Phi_{obj} &= \int_{-\pi}^{\pi} \int_{0}^{\arctan(\frac{a}{z})} I_e A_D \frac{\cos^2\theta}{r^2} \frac{r^2 \sin\theta d\theta d\phi}{r^2} \\
&= \int_{-\pi}^{\pi} \int_{0}^{\arctan(\frac{a}{z})} I_e A_D \frac{cos^4(\theta)}{z^2} \sin\theta d\theta d\phi \\
&= \Phi_0 A_D \frac{1}{z^2} \left(\frac{1}{5} - \frac{z^5}{5(z^2+a^2)^{\frac{5}{2}}} \right)
\end{aligned} \tag{3.7}$$

Although this expression looks quite complex, this expression can be largely divided into two regions, corresponding to the conditions $z^2 >> a^2$, and $z^2 << a^2$. For these two extremes, the expression simplifies to:

$$\Phi_{obj} \approx \begin{cases} \Phi_0 A_D \frac{1}{5z^2} & \text{for } z^2 << a^2 \\ \Phi_0 A_D \frac{a^2}{2z^4} & \text{for } z^2 >> a^2 \end{cases} \tag{3.8}$$

These two trends intersect at $z^2 = \frac{5}{2}a^2$, or $z = \sqrt{\frac{5}{2}}a$

This behavior can be approximated by an inverse quartic of the form:

$$\frac{\Phi_0}{2\pi} A_D \frac{a^2}{z^2(2z^2 - 0.70az + 5a^2)} \tag{3.9}$$

or in terms of r_e

$$\frac{\Phi_0}{2\pi} A_D \frac{a^2}{r_e^2(2r_e^2 - 0.81ar_e + 3.2a^2)} \tag{3.10}$$

For a lambertian source, we simply apply our analysis with $I_e = \frac{\Phi_0 \cos(\theta)}{\pi}$, and obtain:

$$\begin{aligned}\Phi &= \int_{-\pi}^{\pi}\int_{0}^{\arctan(\frac{a}{z})} \frac{\Phi_0}{\pi} A_D \frac{cos^5(\theta)}{z^2} \sin\theta d\theta d\phi && (3.11)\\ &= \frac{\Phi_0}{\pi} A_D \frac{1}{z^2}\left(\frac{1}{6} - \frac{z^6}{6(z^2+a^2)^3}\right) && (3.12)\\ & && (3.13)\end{aligned}$$

Once again, for the two extremes, this relation simplifies to a simple quartic and a quadratic.

$$\Phi \approx \begin{cases} 2\Phi_0 A_D \frac{1}{6z^2} & \text{for } z^2 << a^2 \\ 2\Phi_0 A_D \frac{a^2}{2z^4} & \text{for } z^2 >> a^2 \end{cases} \tag{3.14}$$

intersecting at $z^2 = 3a^2$, or $z = \sqrt{3}a$

This approximates to:

$$\Phi \approx \begin{cases} \frac{\Phi_0}{\pi} A_D \frac{a^2}{z^2(2z^2 - 0.85az + 6a^2)} & \text{in terms of } z \\ \frac{\Phi_0}{\pi} A_D \frac{a^2}{r_e^2(2r_e^2 - 0.95ar_e + 4.17a^2)} & \text{in terms of } r_e \end{cases} \tag{3.15}$$

Table 3.2 below summarizes the behavior of several illumination profiles that are analytically solvable.

3.1.4 Generalization and Numerical Simulations result

In general, we will find that the intensity and time-of-flight of the detected signal of an object can be approximated using the following model:

$$\Phi_{obj} = \Phi_0 A_D \frac{c_0 c_2}{r_e^2(r_e^2 + c_1 r_e + c_0)} \tag{3.16}$$

$$\Delta t = \frac{r_e}{c} \tag{3.17}$$

Note that this approximation has no loss in generality, for there are more parame-

Table 3.2: Intensity Behavior for Various Illumination Profiles

Illum. Profile	Limit Behavior			Quartic Approximation
I_e	$\frac{z}{a} << \eta$	$\frac{z}{a} >> \eta$	η	$\Phi(z)/\Phi(r_e)$
$\frac{\Phi_0}{2\pi}$	$\Phi_0 A_D \frac{1}{5z^2}$	$\Phi_0 A_D \frac{a^2}{2z^4}$	$\sqrt{\frac{5}{2}}$	$\Phi_0 A_D \frac{a^2}{z^2(2z^2-0.70az+5a^2)}$ $\Phi_0 A_D \frac{a^2}{r_e^2(2r_e^2-0.81ar_e+3.2a^2)}$
$\frac{\Phi_0}{\pi} \cos\theta$	$2\Phi_0 A_D \frac{1}{6z^2}$	$2\Phi_0 A_D \frac{a^2}{2z^4}$	$\sqrt{3}$	$2\Phi_0 A_D \frac{a^2}{z^2(2z^2-0.85az+6a^2)}$ $2\Phi_0 A_D \frac{a^2}{r_e^2(2r_e^2-0.95ar_e+4.17a^2)}$
$\frac{(N+1)\Phi_0}{2\pi} \cos^N \theta$	$\frac{N+1}{N+5} \Phi_0 A_D \frac{1}{z^2}$	$(N+1)\Phi_0 A_D \frac{a^2}{2z^4}$	$\sqrt{\frac{N+5}{2}}$	$(N+1)\Phi_0 A_D \frac{a^2}{z^2(2z^2-abz+(N+5)a^2)}$ * $(N+1)\Phi_0 A_D \frac{a^2}{r_e^2(2r_e^2-abr_e+\frac{(N+4)^2}{N+5}a^2)}$ *
$\frac{\Phi_0 \delta(\theta)}{2\pi}$	$\Phi_0 A_D \frac{1}{z^2}$	-	-	$\frac{\Phi_0}{A} D \frac{1}{z^2} = \frac{\Phi_0}{A} D \frac{1}{r_e^2}$
$\frac{(\frac{\pi}{2}-\theta)}{\pi(\pi-2)} \Phi_0$	$\Phi_0 A_D \frac{5}{64(\pi-2)z^2}$	$\Phi_0 A_D \frac{a^2}{4(\pi-2)z^4}$	$\sqrt{\frac{16}{5}}$	$\frac{\Phi_0}{A} D \frac{5a^2}{(4\pi-8)(5z^2-az+16a^2)}$

* b is some function of N (i.e. $b = f(N)$). The exact expression is not important for this analysis.

ters than observable quantities. However, we will find that this model is a particularly useful one in analyzing the scope of signals that occur naturally from an ordinary object. Specifically, we will find that for radial motion, the parameters c_0, c_1, and c_2 are not effected to first order for a large range of objects. We will call this model the *Object Parameter Model*, and will refer to the three parameters c_0, c_1, and c_2 as the *object parameters.*

The two measurable quantities for a Pulsed TOF system can now be represented in terms of this object parameter model as follows:

$$
\begin{aligned}
W_1 &= \Phi_0 A_D \frac{c_0 c_2}{r_e^2(r_e^2 + c_1 r_e + c_0)} T_p \frac{r_e}{r_0} \\
W_2 &= \Phi_0 A_D \frac{c_0 c_2}{r_e^2(r_e^2 + c_1 r_e + c_0)} T_p \qquad (3.18) \\
\text{where } r_0 &= \frac{cT_p}{2}
\end{aligned}
$$

Using the numerical simulation model developed in Chapter 2 with a 100 by 100 grid. Intensity was measured against Effective Distance, and each set of data was fit to object parameters using linear least square estimation. The results are summarized in Appendix B The results show that for the set of scenes tested, all scenes can be modeled with a constant values for c_0, c_1, and c_2, with only the values of r_e changing over the course of the motion. The average error for each point was less than 0.1%, showing that the model sufficiently represents the effective distance to intensity relationship of objects for the scenes simulated.

3.2 Physical Interpretation of Parametric Model

The physical interpretation of these object parameters c_0, c_1, c_2, are as following:

- c_0: The *Effective Area.* This parameter signifies the effective area of the object. The effective area of an object is a function of the physical surface area of the object illuminated by the source, weighted by the strength of the source and the efficiency of the detector in that solid angle. Narrow illumination profiles result in larger effective areas for the same object, and off axis objects will appear to have a smaller effective area. $\frac{c_0^2}{r_e^2}$ is closely related to the fraction of the optical power incident on the object.

- c_1: The *Effective Dimension.* This parameter is related to the dimensions of the object's profile. The closer the object is to a perfect disk/sphere, the smaller this value becomes. Being further off axis of the source also increases this parameter. For on axis objects, $\frac{1}{2\pi}$ of the circumference is an effective order-of-magnitude approximation.

- c_2: The *Effective Reflectivity* This parameter is the joint effect of the object's orientation and surface properties, as well as the radiance of the source observed at the object. It can be roughly understood as the ratio of the strength of light incident on the object to the strength of light reflected from the object, and will take on values of between 0 and unity.

In this section, we will look into further detail how each parameter is effected by physical attributes.

3.2.1 Size

Size of the object predominantly effects the two parameters c_0 and c_1. These two parameters are a direct consequence of the way the light falls off the edge of the object, and are therefore directly related to the size of the object. For small objects that are directly in line of sight of the sensor, we expect c_0 to be roughly equal to the profile area of the object. Objects that are in the peripherals of the field of view would appear smaller, and would diminish as they exit the field of view. c_1 also depends on size, but is roughly proportional to linear dimension as opposed to area.

These observations can be explained by our understanding of the limit cases. When an object is very close to the sensor, it appears like an infinite plane, and the behavior becomes independent of the area to first order. This corresponds with our model's behavior for $r_e << \sqrt{c_0 - \frac{c_1^2}{4}} - \frac{c_1}{2}$, where the intensity is independent of both c_1 and c_0. When the object is far away, the intensity equation converges to $\Phi_0 A_D \frac{c_2 c_0}{r_e^4}$, which agrees with the behavior of an infinitesimal area element $dA = c_0$.

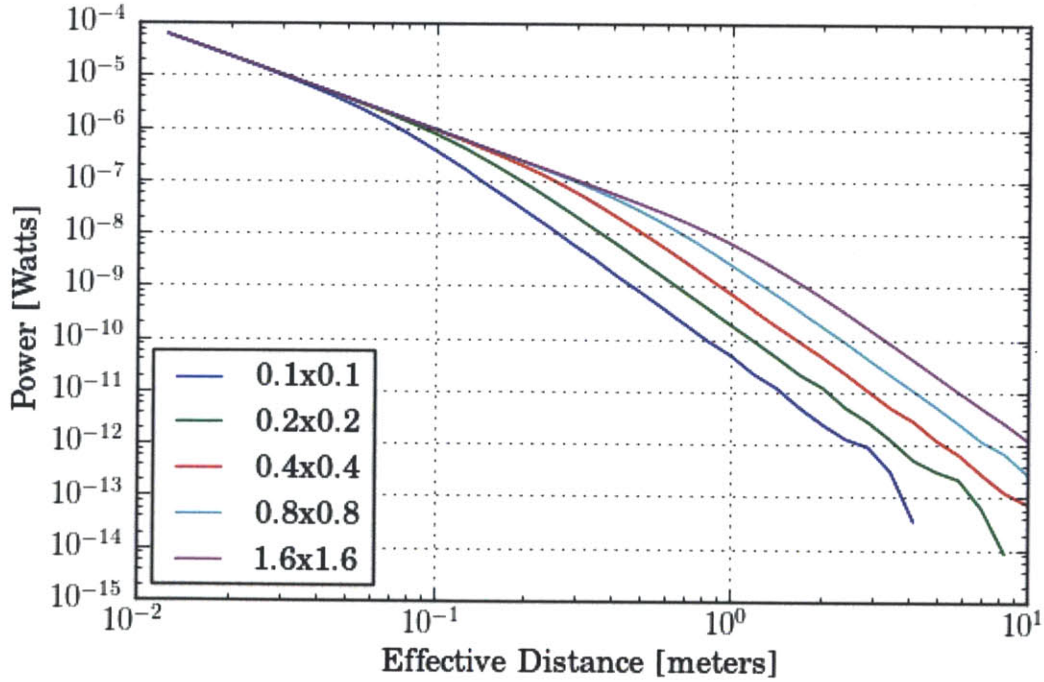

Figure 3-1: Effective Distance v.s. Intensity for a Diffuse Square of Various Sizes

3.2.2 Shape

Shape has an effect on the transition between square law behavior and fourth law behavior. This is characterized by the parameter c_1 in the object parameter model. Figure 3-2 show a series of simulation results of a rectangular sheet of fixed area of 0.36m^2, but with various ratios of width and height. In general, an elongated shape results in a larger value of c_1, or equivalently, a slower transition from square law to fourth law behavior.

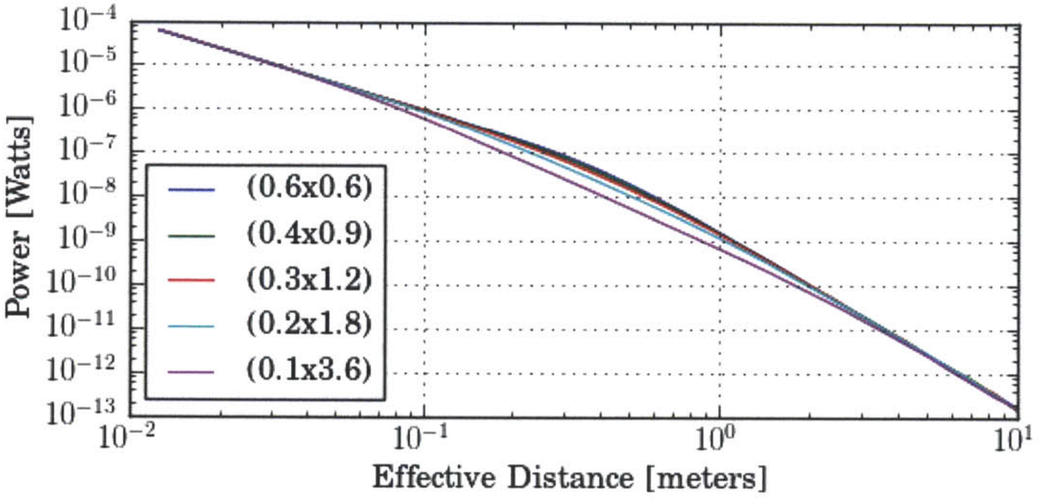

Figure 3-2: Effective Distance v.s. Intensity for Rectangles of Various Proportions w/ Diffuse Surface

3.2.3 Object Orientation

The object orientation can potentially effect all three of the parameters c_0, c_1, and c_2. However, most of those effects are a consequence of the shape of the effective illuminated area changing as an object rotates. Unless the object has radial symettery around the axis of rotation, rotation will change the shape and size of an objects profile. For a planer object, the size or projected area of an object goes as the cosine of the angle between the face normal and the direction of the object. These resultant effects are summarized in the section above, we will focus on the effects that are external to the shape (and size) of the object.

The remaining effect is purely due to the surface orientation of the facets on the object. The primary effect is on c_2, due to the angle dependance of reflectivity of most objects. A metasurface such as a retroreflector also would be exempt from a similar relationship, due to it's property to reflect most of the incident light back at the direction of the source. For objects that have a diffuse surface, c_2 is also mostly independent of object orientation, as angle independence that is the defining property of lambertian reflectors. However, if the object exhibits significant specular components, the object orientation can heavily impact the effective reflectivity. This is due to the dependency of the surface normal in the behavior of specular reflections, and will generally result in a higher effective reflectivity if the object's illuminated surface is orthogonal to the direction of the sensor. Similar to the case of c_0, However, it is possible for the effective area to remain unchanged, while the effective reflectivity changes, and vice versa.

Although relatively small in effect, c_0 can also be effected due to surface orientation. This secondary effect is due to the fact that for an object that is oriented at an angle some parts of the object are closer to the sensor than others, resulting in the transition from square law to fourth law be biased towards the edges that are closer to the sensor. Usually a larger tilt means that this unevenness in edges is exaggerated more, resulting in the transition occurring at a closer effective distance, or equivalently a smaller c_0.

Figures 3-3 and 3-4 show these effects for diffuse reflector and specular reflector, respectively. The small changes in intensity for the diffuse surface are caused by the non-uniform distance of the object, causing closer facets to impact the effective distance more than facets that are further away.

3.2.4 Zenith Angle

The zenith angle also has the potential to effect all three parameters. Although the actual exposed area of the object may not change with the angular position with respect to the sensor, due to the weighting caused by the emitters radiant intensity distribution, (i.e. the shape of $I_e(\theta)$), and the detectors angular response (generally

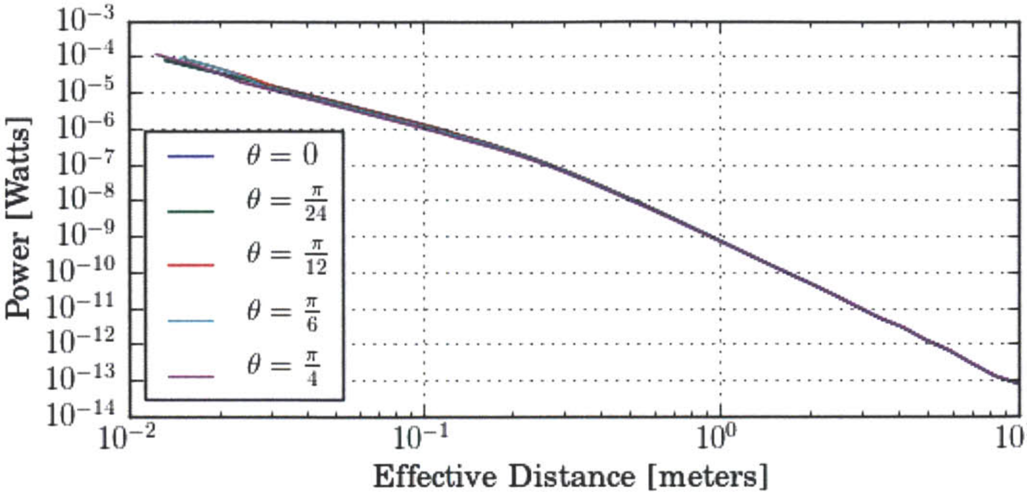

Figure 3-3: Effective Distance v.s. Intensity for Diffuse Rectangles Oriented at Different Angles wrt. Sensor

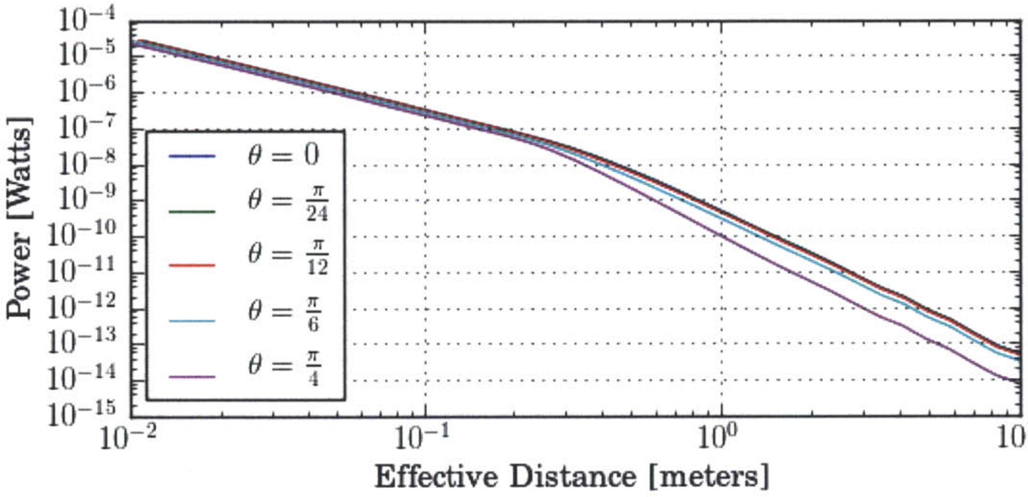

Figure 3-4: Effective Distance v.s. Intensity for Specular Rectangles Oriented at Different Angles wrt. Sensor

lambertian for a planer diode), off axis objects tend to be represented by a smaller effective area c_0 than those near the zenith.

c_1 can be understood as a parameter that represents how distributed the object's edge is with respect to zenith angle. Physically, this distribution doesn't change as a function of zenith angle, but once again, the weighting mentioned above makes this a little more complicated. As the zenith angle changes, different parts of the object have a different weighting, and hence so does the zenith angle distribution. Therefore, c_1 ends up being larger objects positioned closer to the zenith. Only one of the two dimensions of the object gets shrunk due to this effect, so once again, c_1 scales roughly as the square route of c_0.

c_2 changes as a direct consequence of the zenith angle, as this is the parameter that gets directly effected by the emitters radiant intensity distribution, and the detectors angular response. c_2 generally is larger for angles close to the zenith, due to the emitter and detectors angular response. For diffuse reflections, this is the only factor that effects c_2 as a function of zenith angle. However, for specular components, we must take into account the change in specular reflectivity that is caused by the alignment between the illumination source and the object orientation, as discussed above. This usually results in c_2 peaking at an angle somewhat in-between the zenith and the angle that maximally aligns the object's prominent surface normal and the direction of the object. As discussed above, this effect highly depends on the shape of the object, and is non existent for symmetrical shapes such as a sphere.

Figure 3-5 shows these relationships for a diffuse object. These effects are similar but are generally stronger for specular objects as well as systems that use a illumination source with a non-uniform radiant intensity.

3.2.5 Surface Properties

The surface property of an object has two main effects. The first is to influence the overall intensity of the the reflection. Stemming from difference in a materials inherent reflectivity, this effect is represented by different values of c_2 in the object parameter model.

The second effect is the angular redistribution due to diffuse v.s. specular reflections. Objects with surfaces that behave as specular reflectors oriented towards the sensor will tend to exaggerate their sizes, resulting in larger values of c_0 compared to diffuse objects. As briefly mentioned above, this influences the behavior for the object orientation as well as zenith angle. Change in both surface properties and other physical attributes can create chaotic results, but luckily, surface properties tend to

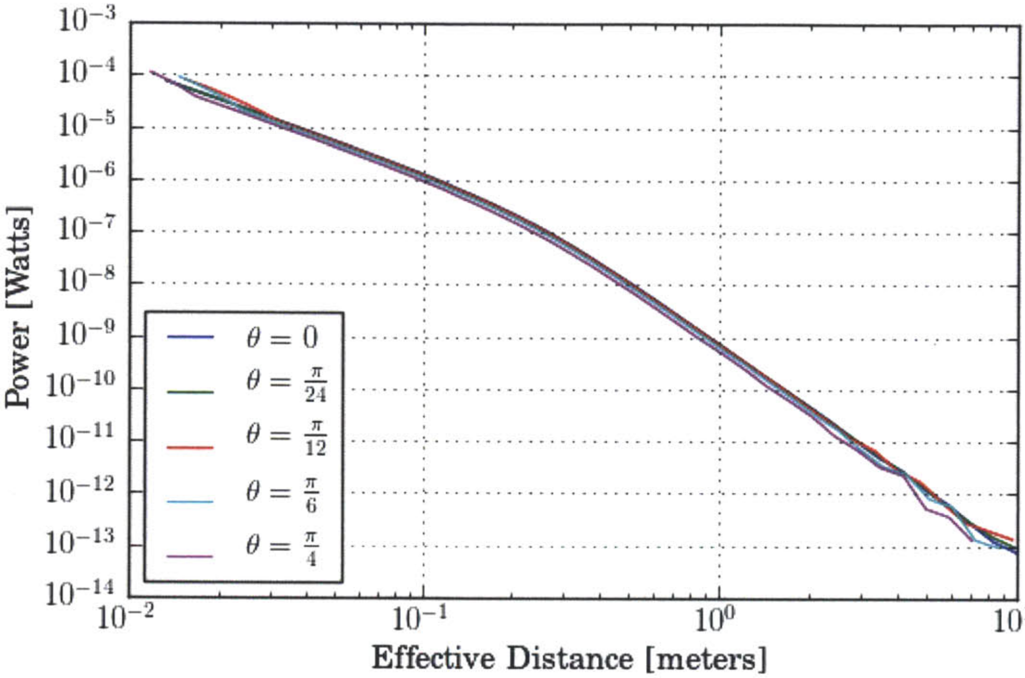

Figure 3-5: Effective Distance v.s. Intensity for Objects at Different Zenith Angles

stay consistent for typical physical objects.

Figure 3-6 shows the effective distance to intensity relationship for different surface properties, ranging from diffuse to highly specular. Note the brief transition to fourth law behavior at around 0.4m caused by light falling off the edge of the object at 0.4m, but switching back to square law behavior for highly specular objects. This is due to the highly direction dependent nature of specular reflectivity, resulting in the area of the object less relevant than the sections of the object that are directly orthogonal to the incoming rays. Even with these artifacts, the behavior can be approximated with the object parameter model with an average error of less than 1.5% for the case of a smooth object with the rms slope $m = 0.1$, and an average error of less than 4% for a smooth surface with $m = 0.01$.

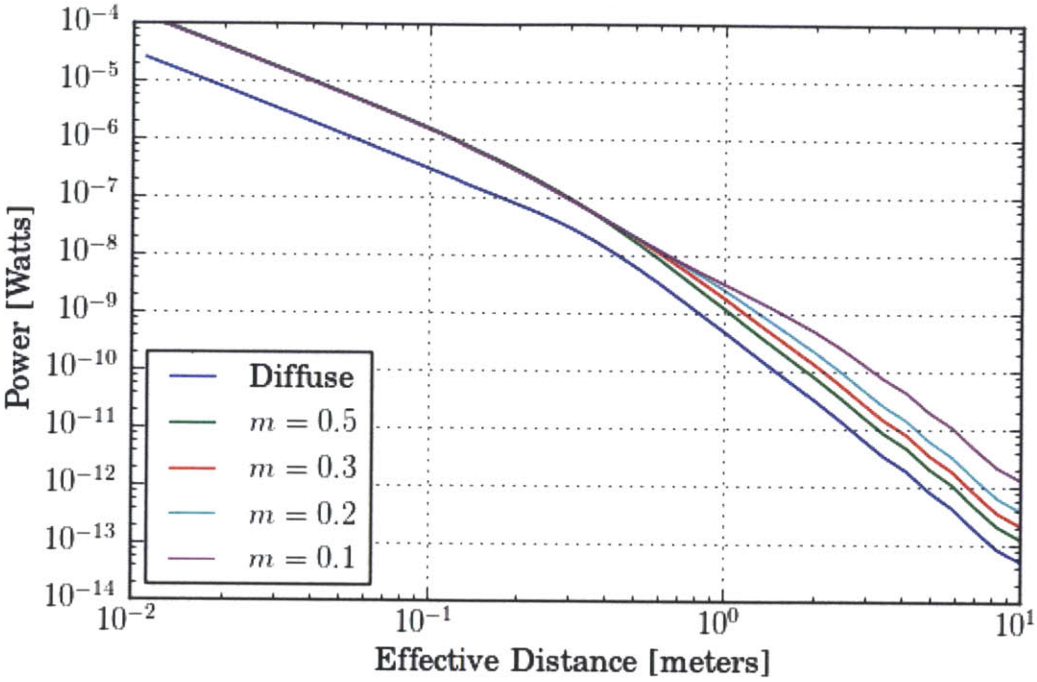

Figure 3-6: Effective Distance v.s. Intensity for Rectangles of Different Surface Properties

3.2.6 Compound Motion

The results shown above are quite promising, but it would be a gross over simplification to say that the parameters c_0, c_1, and c_2 can be considered constant. The simplest example is off axis linear motion, where an object moves linearly in space, but not as a simple radial motion with respect to the sensor. In this case, both the radial distance and the zenith angle changes, resulting in a change in the effective distance r_e as well as potentially all of the the object parameters c_0 through c_2. Figure 3-7 illustrates 4 sets of linear motion, where the motion indicated in red (i.e. C.D) are *off-axis* motions, and those indicated in black (i.e. A, B) are *on-axis*. Figure 3-8 shows an example of the effective distance v.s. intensity relationship that can result from off-axis linear motion.

Even when the object motion is on-axis, the effective reflectivity can drastically change depending on the shape of the object. Figure 3-9 shows an example of this

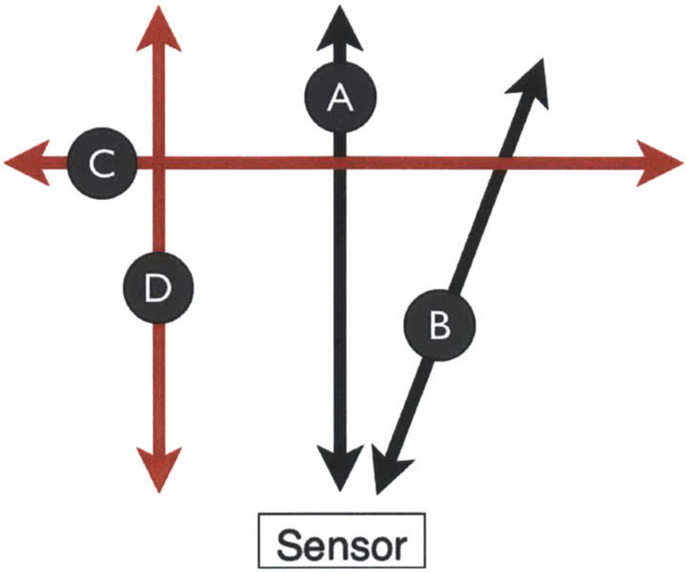

Figure 3-7: Off-axis linear motion causes a change in zenith angle, while on-axis linear motion doesn't.

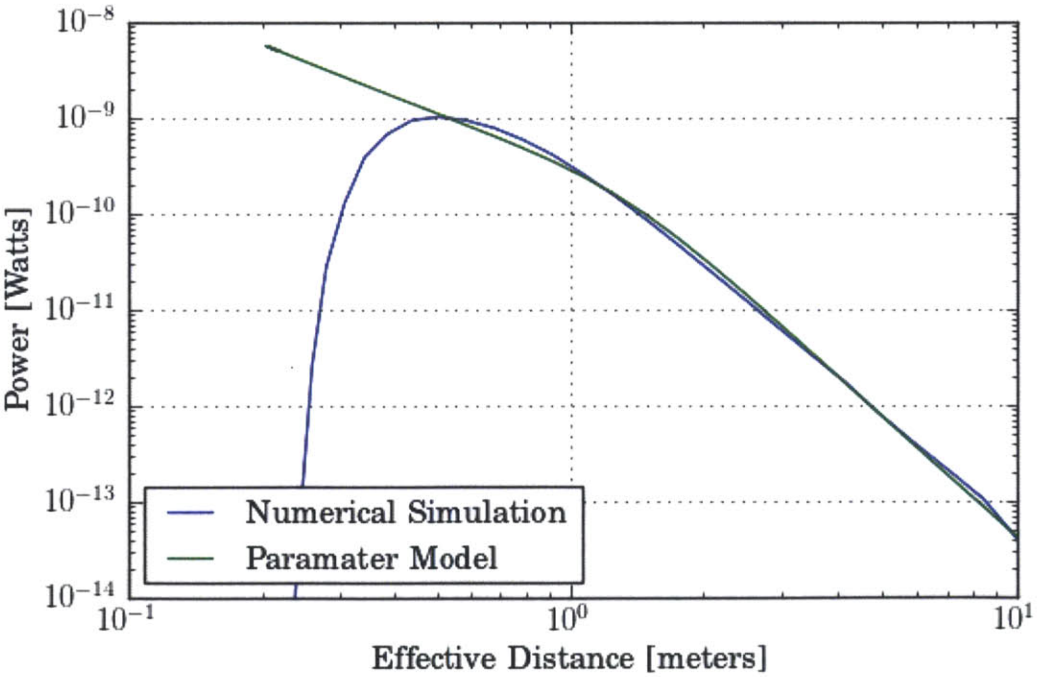

Figure 3-8: Effective Distance v.s. Intensity for an Example of Off-axis Linear Motion.

where a smooth object whose face is not orthogonal to the direction of motion. When the object is close, part of the face is directly orthogonal to the rays, contributing a large part of the reflected intensity. When the object is far, none of the object is orthogonal to the incident rays, and the intensity decays much steeper. This can be interpreted as the object's effective reflectivity c_2 changing as well as the effective distance r_e.

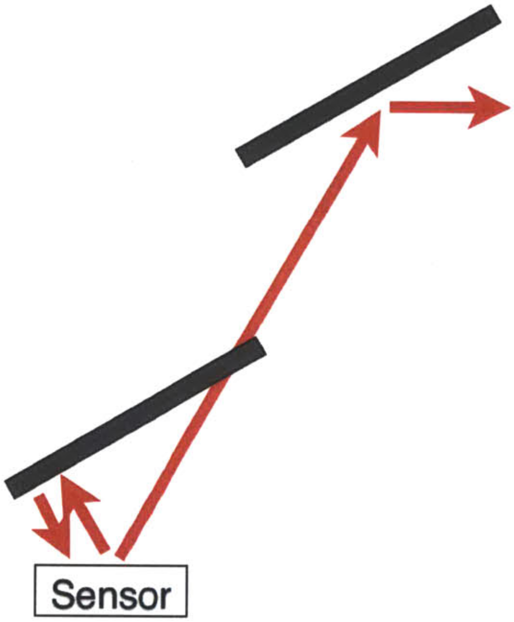

Figure 3-9: An object whose face is at an angle may present a change in effective reflectivity.

3.2.7 Parameterizing Objects in SWM TOF Systems

The analysis above was conducted for a pulsed TOF system. However, a similar analysis applies to directly for a SWM TOF system. the major difference between the two is how the components add linearly for a Pulsed TOF system, where as components add as vectors for SWM TOF systems. This manifests itself in a slightly different relationship between physical distance and the effective distance parameter. This relationship will depend on the frequency of the modulation, and is given by the

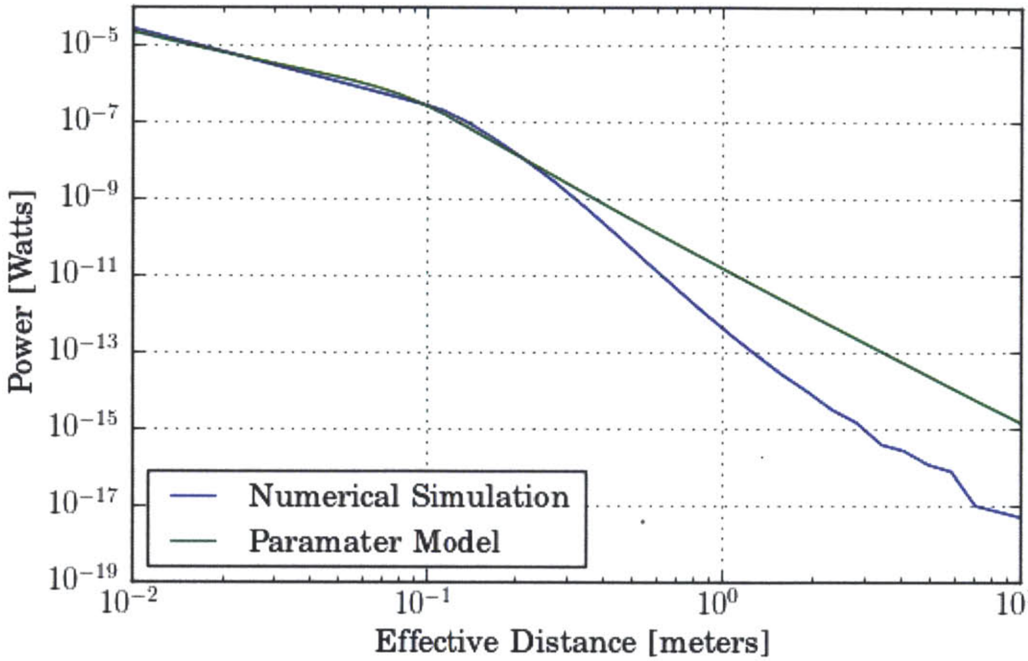

Figure 3-10: Effective Distance v.s. Intensity for an Example of a Changing Effective Reflectivity

solution to the equation:

$$
\begin{aligned}
r_e &= \frac{c}{4\pi f} \angle \iint\limits_{O} d\Phi_{obj}(\mathbf{r}_s) e^{jk(||\mathbf{r}_i||+||\mathbf{r}_o||)} \\
&= \frac{c}{4\pi f} \tan^{-1}\left(\frac{\iint\limits_{O} d\Phi_{obj}(\mathbf{r}_s) \sin(k(||\mathbf{r}_i|| + ||\mathbf{r}_o||))}{\iint\limits_{O} d\Phi_{obj}(\mathbf{r}_s) \cos(k(||\mathbf{r}_i|| + ||\mathbf{r}_o||))} \right)
\end{aligned}
\tag{3.19}
$$

Using this modified definition, we can now express the two measurable quantities x_I and x_Q as the following:

$$
\begin{aligned}
x_I &= \Phi_0 A_D \frac{c_0 c_2}{r_e^2(r_e^2 + c_1 r_e + c_0)} \pi \cos(k r_e + \phi_0) \\
x_Q &= \Phi_0 A_D \frac{c_0 c_2}{r_e^2(r_e^2 + c_1 r_e + c_0)} \pi \sin(k r_e + \phi_0)
\end{aligned}
\tag{3.20}
$$

where $k = 2\frac{\omega_m}{c} = \frac{4\pi f}{c}$

or, in complex notation:

$$\begin{aligned}
x &= \Phi_0 A_D \frac{c_0 c_2}{r_e^2(r_e^2 + c_1 r_e + c_0)} \pi e^{j(kr_e + \phi_0)} \\
x_I &= \Re(x) \\
x_Q &= \Im x
\end{aligned} \tag{3.21}$$

In the case of the time-of-flight distance sensor IC ISL29200, the modulation frequency is 5MHz, and has a detection range of 2m. For this system, the range of distances detectable by the system only occupies a range of 24 degrees in phase, due to noise considerations. This is a sufficiently small enough range in phase such that the effective distance becomes approximately the same as that in a pulsed TOF system. In a numerical simulation similar to those shown in Tables B.1 through B.4 for a SWM system with a modulation frequency of 5MHz, and similarly low error rates are achieved with an average error of less than 0.1%. However, in the general case, if designing a SWM TOF system that utilizes much more of it's phase range, this approximation may not be appropriate.

3.3 Compound Scenes

The models developed above describes a planer facet as a function of it's position and orientation. However, a typical scene consists of more than just the a single object (or to be more specific, a single face of an object). Thus we must consider how multiple faces, multiple objects, and backgrounds behave in more complex scenes. In addition to these additional components of the optical scene, we will also study the effect of electrical and optical crosstalk in the system.

3.3.1 Crosstalk

Cross talk in TOF systems come in two forms, electrical and optical. Electrical crosstalk is caused by electrical coupling between driver circuitry and the sensing circuitry. Both capacitive and inductive (magnetic) coupling is possible, resulting in the injection of a signal in to the detector. Regardless of the exact mechanism, the result is a signal that behaves much like a TOF signal, superimposed on top of the actual signal.

Optical crosstalk can be considered as part of the scene, but is worth special note since it can be quite significant and is highly systematic. For many assemblies, light from the emitter of the system reflects inside the internal structure of the sensor or sensor housing, resulting in a some signal at the detector even in the complete absence of reflective objects in the sensor's field of view. This is a known problem for many amplitude based proximity sensors, especially for those used in electronics with a glass cover such as smart phones. Glass has an index of refraction of approximately 1.5, resulting in approximately 4% reflection *per air-glass interface*, for a total of 8% reflection. 3D structures and anti-reflective coatings can be used to minimize these reflections, but typically at the expense of field of view and higher manufacturing costs. Even industry standard practices result in some residual internal reflections, limiting the dynamic range for amplitude based proximity sensors.

For both forms of crosstalk, the crosstalk simply linearly superimposes itself to any real TOF signal received by the sensor. For Pulsed TOF, this implies that the two windows will now be given as follows:

$$\begin{aligned} W_1' &= W_1 + CT_1 \\ W_2' &= W_2 + CT_2 \end{aligned} \tag{3.22}$$

Similarly, for SWM TOF, the two demodulated signals would result in the following:

$$\begin{aligned} x_I' &= x_I + CT_I \\ x_Q' &= x_Q + CT_Q \end{aligned} \tag{3.23}$$

If this crosstalk is not considered in the time of flight computation, it will create an error in the computed time of flight, and consequently any distance measurement based on such measurement. The combined signal computes to a effective distance with a systematic error that is dependent on both the strength and the timing or phase or the crosstalk.

However, this problem is relatively simple to calibrate. If the two quantities CT_1 and CT_2 (or CT_I and CT_Q for SWM TOF) can be quantified, they can be subtracted out from the measured signal.

For Pulsed TOF, the expression becomes:

$$\begin{aligned} r_e' &= \frac{c\Delta t}{2} = \frac{c}{2}T_p\frac{W_1'}{W_2'} \\ &= \frac{c\Delta t}{2} = \frac{c}{2}T_p\frac{W_1 + CT_1}{W_2 + CT_2} \end{aligned} \tag{3.24}$$

For SWM TOF, the expression is:

$$\begin{aligned} r_e' &= \frac{c}{4\pi f}tan^{-1}\left(\frac{x_I'}{x_Q'}\right) \\ &= \frac{c}{4\pi f}tan^{-1}\left(\frac{x_I + CT_I}{x_Q + CT_Q}\right) \end{aligned} \tag{3.25}$$

Figure 3.3.1 below show how crosstalk can adversely impact the distance response of a time of flight system.

3.3.2 Multiple Objects

Multiple objects, or multiple faces of an object, will each behave as the model developed through this chapter. Since this model was developed by specifying the limits of integration, we can expect multiple objects to simply add together, as long as their respective regions or limits do not intersect. The combined signal will have an

Figure 3-11: Effects of Crosstalk of Different Strengths

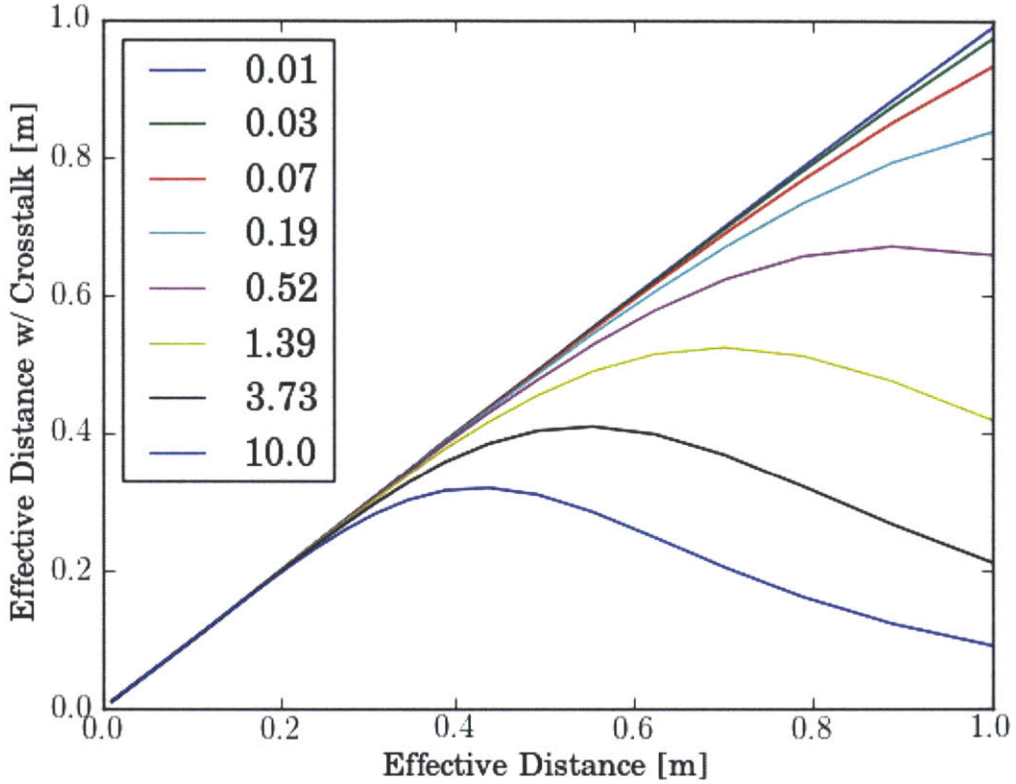

effective distance as follows:

$$
\begin{aligned}
r_e &= \frac{c\Delta t}{2} = \frac{c}{2}T_p\frac{W_{1A}+W_{1B}}{W_{2A}+W_{2B}} && \text{for Pulsed TOF} \\
r_e &= \frac{c}{4\pi f}tan^{-1}\left(\frac{x_{IA}+x_{IB}}{x_{QA}+x_{QB}}\right) && \text{for SWM TOF} \qquad (3.26)
\end{aligned}
$$

The effective distance computed from the combined signal can be understood as a "vector sum" of the two objects. For SWM TOF, this is literally the case, as the two signal is represented as two orthogonal components, and the phase can be understood as the argument of the signal in the complex plain. The effective distance of a combined signal for Pulsed TOF is similar in mechanism, although not as mathematically elegant. In principle, it is possible to have two objects that cancel each other for SWM. If an object that is sufficiently far enough such that the phase contribution is 180 degrees apart from a small object, it is conceivable

Figure 3-12: Effects of Crosstalk of Different Timing/Phases

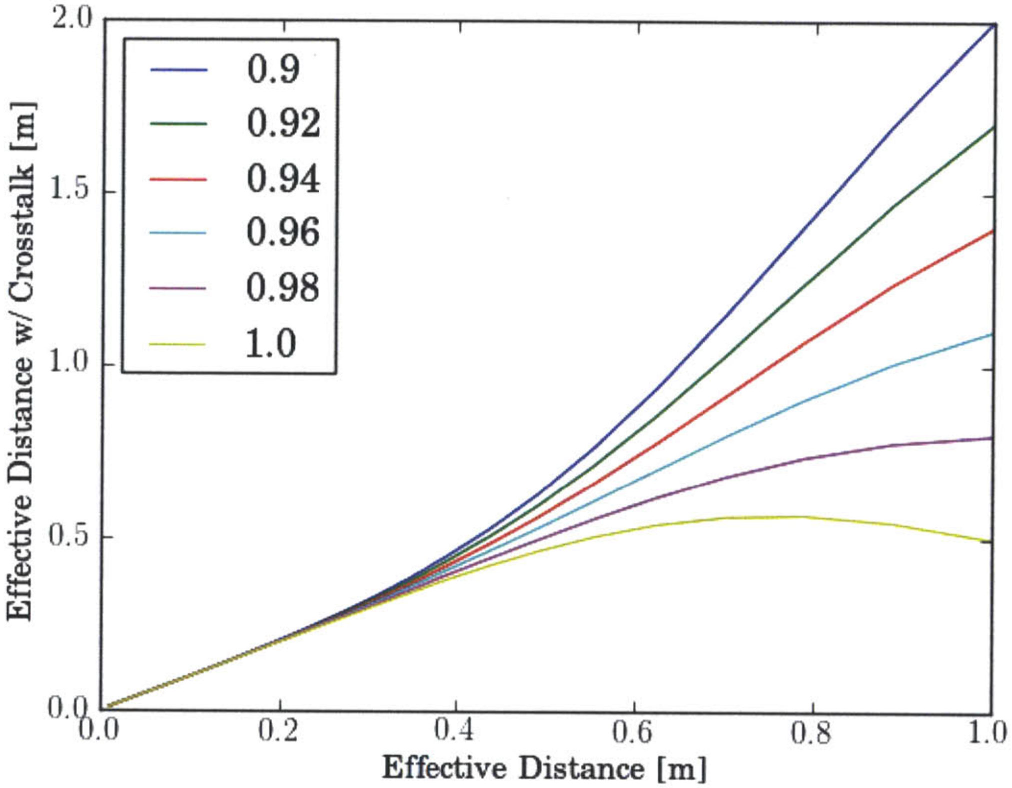

for the two components to cancel each other out. For the ISL29200 the signal from any reflector would drop below the noise floor before reaching full phase inversion, thus, interpreting the combined effective distance as the weighted average is sensible. However, this would not be the case for systems that operate over the full range of phase, often called the *unambiguous detection range* in distance. This implies that the use of very high frequency modulation can be problematic for systems that employ a high degree of spatial averaging such as the ISL29200, as the computed combined signal may not accurately represent any object in the field of view, or even a sensible combination of objects in the field of view.

3.3.3 Uniform Background

Up until this point, we have assumed that the light that falls off the edge of the object simply disappears. However, in reality, the light must hit something, however far away, and some of that light, is bound to make it back to the sensor. Although at first site, the background may seem similar to the problem of multiple objects, there is one fundamental difference; the background reflection is dependent on the object's shadow. For example, if the object is very close to the sensor and is occupying the entire field of view, there would be no signal contribution from the background. conversely, as the object is farther away, the background occupies most of the scene's field of view, resulting in being the dominant contribution to the signal.

We will first consider the case of a uniform background. In this scenario, we will assume that the background is effectively a uniform sphere surrounding the sphere at some distance R.

The total signal intensity Φ_{BG} from such a background would be given by the expression:

$$\Phi_{BG} = \int_{-\pi}^{\pi} \int_{0}^{\frac{\pi}{2}} fr_{BG}(\theta) I_e(\theta) A_D \frac{\cos\theta \sin\theta d\theta d\phi}{R^2} \tag{3.27}$$

and the time of flight would simply be $\Delta t = 2cR$.

However, in the presence of an object, the background is limited to the perimeters of the object, and the integral is evaluated over the region $O' = \Omega - O$, the compliment of the region O used in defining the object parameter model above. We will denote this signal intensity as Φ_{bg}:

$$\begin{aligned} \Phi_{bg} &= \iint\limits_{O'} fr_{BG} I_e(\theta) A_D \frac{\cos\theta \sin\theta d\theta d\phi}{R^2} \\ &= \Phi_{BG} - \iint\limits_{O} fr_{BG} I_e(\theta) A_D \frac{\cos\theta \sin\theta d\theta d\phi}{R^2} \end{aligned} \tag{3.28}$$

Compare this to the signal intensity for the reflection from an object:

$$\Phi_{obj} = \iint\limits_{O} fr_{\theta}(\theta) I_e(\theta) A_D \frac{\cos\theta \sin\theta d\theta d\phi}{r^2} \tag{3.29}$$

We will apply the exact same approximation that led us to the object parameter model, and obtain:

$$\begin{aligned}\Phi_{bg} &= \Phi_{BG} - \Phi_{BG}\frac{c'_0}{(r_e^2 + c'_1 r_e + c'_0)} \\ &= \Phi_{BG}\frac{r_e^2 + c_1 r_e}{(r_e^2 + c'_1 r_e + c'_0)} \qquad (3.30)\end{aligned}$$

where in the general case c_0, c_1 are related to c'_0 and c'_1, but are not necessarily equal. In the case where $fr(\theta)$ is constant for all r_e, the two expressions converge. This condition is only met if the object is perfectly diffuse, or for a metasurface such as a retro reflector. Note that for $\lim_{r_e \to 0}$, the expression converges to 0, indicating that the background is completely shadowed by the object.

This background signal superimposes itself with the signal from the object similar to the fashion of crosstalk or multiple objects.

$$\Phi = \Phi_{bg} + \Phi_{obj} \qquad (3.31)$$

We can quantify the effects this additional term has on the measured quantities W_1 and W_2 for a Pulsed TOF system, by integrating over the window for each case:

$$\begin{aligned}BG_1 &= \int_{W_1} \Phi_{bg}(r_e, c'_0, c'_1)dt \\ &= \Phi_{bg}(r_e, c'_0, c'_1)T_p\left(1 - \frac{R}{r_0}\right) \\ BG_2 &= \int_{W_2} \Phi_{bg}(r_e, c'_0, c'_1)dt \\ &= \Phi_{bg}(r_e, c'_0, c'_1)T_p \qquad (3.32)\end{aligned}$$

Now, our total measured quantities W'_1 and W'_2 can be expressed as a superposition of the desired components and the background component.

$$\begin{aligned} W_1' &= W_1 + BG_1 \\ W_2' &= W_2 + BG_2 \end{aligned} \tag{3.33}$$

Similarly, for a SWM TOF system:

$$\begin{aligned} x_I' &= x_I + BG_I \\ x_Q' &= x_Q + BG_Q \\ BG_I &= \Phi_{bg}(r_e, c_0', c_1')\pi \sin(kR) \\ BG_Q &= \Phi_{bg}(r_e, c_0', c_1')\pi \cos(kR) \\ x_I' &= x_I + BG_I \\ x_Q' &= x_Q + BG_Q \end{aligned} \tag{3.34}$$

We will use these models to help us estimate the parameters in the next chapters.

3.3.4 Non-uniform Backgrounds, Multiple Overlapping Objects, and Beyond

Of course the real world is not quite so simple, and is really a continuous 3d structure with multiple independently moving objects. Although it is conceivable to extend our model to cover multiple overlapping objects, or a non-uniform background, it is impossible to do so with out introducing new parameters that are dependent on the geometry between the two objects. However, for the scope of this work, we will limit the complexity to models developed up to this point.

3.4 Summary of Object Parameter Model

In this chapter, we have identified the effective distance r_e as a natural metric to characterize the contribution of an object on a TOF system. We have considered a wide range of possible objects and have found that objects can typically be modeled using the object parameter model by introducing the three parameters c_0, c_1, and c_2. The physical significance of each of these parameters were examined, identifying trends and properties of each. For many physical scenarios, it was shown that these three parameters can be considered constant while equally many other scenarios cause the parameters to change.

Chapter 4

Real Time Parameter Extraction Techniques

We will now focus on the original problem at hand, to extract the distance and other information from intensity and time of flight information. Although there are many ways to process the information acquired, we will classify them into two categories; real time techniques, and algorithmic techniques. This chapter will discuss the first of the two, where information from only the current samples and it's derivatives are used. These techniques are generally have a low computational cost, but often will often require some prior knowledge of the scene in question.

Many circuit level concerns such as noise, phase jitter, and changes in frequency and gain through thermal drift are not included in this analysis for the sake of simplicity, but would need to be considered for implementation in a physical system. In general, the techniques developed in this chapter are still applicable in the presence of these circuit non-idealities, but they may required to be adapted to account for their effect.

4.1 Redundancy from Intensity Information

The basic principle behind all hybrid Intensity/Time-Of-Flight techniques is redundancy. Time-of-flight is sufficient for extracting distance in a conventional system, but by looking at the intensity information, we can remove the effects of error sources or extract more information about the scene than is possible using a conventional system. This redundancy can be illustrated using our object parameter model developed in Chapter 3.

The time-of-flight naturally provides a way to compute the effective distance. However, the amplitude of the signal also provides information of the effective distance, as shown in equation 3.16, reproduced below:

$$\Phi_{obj} = \Phi_0 A_D \frac{c_0 c_2}{r_e^2(r_e^2 + c_1 r_e + c_0)}$$

4.1.1 Extracting Effective Distance From Intensity Information

In principle, if the intensity contributed from an object and object parameters c_0, c_1, c_2 can be quantified, we would be able to solve for r_e, enabling us to find the effective distance with out the use of time of flight information. The most straight forward method of doing this is to convert the expression to a polynomial in r_e, and find the roots of the polynomial.

$$\Phi_{obj} r_e^4 + \Phi_{obj} c_1 r_e^3 + \Phi_{obj} c_0 r_e^2 - \Phi_0 A_D c_0 c_2 = 0 \tag{4.1}$$

Where Φ_0, A_D, and T_p are known constants, and c_0, c_1, c_2 are the object parameters which we will assume are known for now. It can be shown that for positive real values of Φ_{obj}, c_0, c_1, and c_2, there will always only be one positive real root of r_e. This allows one to compute the effective distance based off of the only the intensity and the object parameters, such that $r_e = f(\Phi_{obj}, c_0, c_1, c_2)$.

This technique can be directly applied to the Pulsed TOF component W_2 as follows:

$$W_2 r_e^4 + W_2 c_1 r_e^3 + W_2 c_0 r_e^2 - \Phi_0 A_D c_0 c_2 T_p = 0 \tag{4.2}$$

$$r_e = f(W_2, c_0, c_1, c_2)$$

For SWM TOF, we can apply the technique to the amplitude of the signal as follows:

$$|x| = \sqrt{x_I^2 + x_Q^2} = \Phi_0 A_D \pi \frac{c_0 c_2}{r_e^2(r_e^2 + c_1 r_e + c_0)}$$

converting to polynomial form:

$$|x| r_e^4 + |x| c_1 r_e^3 + |x| c_0 r_e^2 - \Phi_0 A_D \pi c_0 c_2 = 0 \tag{4.3}$$

$$r_e = f(x_I, x_Q, c_0, c_1, c_2)$$

4.1.2 Application to Time-Of-Flight Components

This concept of solving for the effective distance using our object parameter model can be extended to any of the measurable quantities of the system. For example, W_1 can be represented as a polynomial resulting in the expression:

$$W_1 r_0 r_e^3 + W_1 c_1 r_0 r_e^2 + W_1 c_0 r_0 r_e - \Phi_0 A_D c_0 c_2 T_p = 0 \tag{4.4}$$

$$r_e = f(W_1, c_0, c_1, c_2) \tag{4.5}$$

To take the concept yet further, we can take multiple equations and solve a system of equations. For example, between equations 4.2 and 4.4, we have two vequations with three parameters (c_0, c_1, c_2) and one unknown (r_e). This allows us to combine the equations to eliminate some of the parameters, in the following way:

$$W_1 r_0 r_e^3 - W_1 c_1 r_0 r_e^2 + W_1 c_0 r_0 r_e = \Phi_0 A_D c_0 c_2 T_p \tag{4.6}$$

$$W_2 r_e^4 + W_2 c_1 r_e^3 - W_2 c_0 r_e^2 = \Phi_0 A_D c_0 c_2 T_p \tag{4.7}$$

Equating the LHS for Eq. 4.6 and Eq. 4.7 :

$$W_1 r_0 r_e^3 - W_1 c_1 r_0 r_e^2 + W_1 c_0 r_0 r_e = W_2 r_e^4 + W_2 c_1 r_e^3 - W_2 c_0 r_e^2 \tag{4.8}$$

Dividing $r_e^3 + c_1 r_e^2 + c_0 r_e$ from both sides:

$$W_1 r_0 = W_2 r_e$$

$$r_e = r_0 \frac{W_1}{W_2} = f(W_1, W_2) \tag{4.9}$$

As expected, we reach the definition of r_e, which can be solved from the two quantities W_1 and W_2 without any dependance on the object parameters. Although this result was trivial, we can apply the same concept to any predictably manipulated form of the TOF components, and more importantly, when sources of error or introduced.

4.2 Differentiation of Time-Of-Flight Signals

Another important tool we will introduce is the derivative form of the TOF components. The derivative information of an intensity based sensor is often used in the form of a motion sensor where changes in the signal level are set to trigger a binary detection of motion. While these sensors are simple and effective at detecting motion, they do so at cost of losing information about the distance, as fast motion is indistinguishable from close motion. However, in a hybrid intensity/time-of-flight system, we will find that the derivatives are not only immune to crosstalk, but that they also retain information about the distance.

In this section, we will analytically solve for the time based derivative of the two orthogonal components of the time of flight measurements, assuming that each of the parameters can potentially changing as a function of time. We will first study the effects of differentiation of the intenisty response of the parameter based object model developed in Chapter 3. Then, we will extend the analysis to the differentiated TOF components for both Pulsed TOF and SWM TOF, and characterize their relationship.

It is worth noting that differentiation is a inherently noisy process, and typically degrades the signal integrity of the system. These effects are not included in this analysis. However, the analysis for derivatives can also be applied to band limited operations such as a first order high pass filter, and a strict differentiation operation is not necessarily required to apply these concepts.

As shown in Chapter 3, the intensity of the signal contribution of an object in the field of view can be approximated by the expression:

$$\Phi_{obj}(r_e, c_0, c_1, c_2) = \Phi_0 A_D \frac{c_0 c_2}{r_e^2(r_e^2 + c_1 r_e + c_0)} \tag{4.10}$$

where all four parameters, (i.e. r_e, c_0, c_1, and c_2) are potentially a function of time. To fully differentiate this expression, we must apply the chain rule for each parameter.

$$\begin{aligned}
\frac{\partial \Phi_{obj}}{\partial r_e} &= \Phi_{obj}\left(-\frac{4r_e^3 + 3c_1 r_e^2 + 2c_0 r_e}{r_e^2(r_e^2 + c_1 r_e + c_0)}\right) \\
\frac{\partial \Phi_{obj}}{\partial c_0} &= \Phi_{obj}\left(\frac{1}{c_0} - \frac{1}{r_e^2 + c_1 r_e + c_0}\right) \\
\frac{\partial \Phi_{obj}}{\partial c_1} &= \Phi_{obj}\left(\frac{-r_e}{r_e^2 + c_1 r_e + c_0}\right) \\
\frac{\partial \Phi_{obj}}{\partial c_2} &= \Phi_{obj}\frac{1}{c_2}
\end{aligned} \tag{4.11}$$

The full time derivative is given by the sum of all these components:

$$\frac{\partial \Phi_{obj}}{\partial t} = \frac{\partial \Phi_{obj}}{\partial r_e}\frac{\partial r_e}{\partial t} + \frac{\partial \Phi_{obj}}{\partial c_0}\frac{\partial c_0}{\partial t} + \frac{\partial \Phi_{obj}}{\partial c_1}\frac{\partial c_1}{\partial t} + \frac{\partial \Phi_{obj}}{\partial c_2}\frac{\partial c_2}{\partial t} \tag{4.12}$$

We will focus on these derivatives term by term to understand their behaviors.

4.2.1 Differentiation with respect to Effective Distance r_e

The first of these terms is possibly the most interesting of the four. This term $\frac{\partial \Phi_{obj}}{\partial r_e}\frac{\partial r_e}{\partial t}$ represents the component of the derivative caused by an object moving closer or farther from the sensor, all other parameters held constant. A small subset of applications could be physically constrained to this condition, making this term the dominant term in an application. Furthermore, objects that move radially with respect to the sensor are likely to be the objects of most interest to the host system. We will mathematically analyze the expression for these derivatives, and study what properties they may have that can be exploited to estimate the object's parameters.

4.2.1.1 Intensity

We will first consider how the derivative of the intensity with respect to effective distance behaves. Using the object parameter model, we obtain:

$$\frac{\partial \Phi_{obj}}{\partial r_e} = \Phi_{obj}\left(-\frac{4r_e^3 + 3c_1 r_e^2 + 2c_0 r_e}{r_e^2(r_e^2 + c_1 r_e + c_0)}\right) \tag{4.13}$$

In itself, this measure does not appear particularly revealing. However, taking another look at the effective distance v.s. intensity curves from Chapter 3, we recall that the logarithmic slope off the effective distance and intensity revealed important features about the objects size and shape. Thus, we will evaluate an expression that best describes the logarithmic slope: $\frac{\partial \Phi_{obj}}{\partial r_e}\frac{r_e}{\Phi_{obj}}$

$$\begin{aligned}\frac{\partial \Phi_{obj}}{\partial r_e}\frac{r_e}{\Phi_{obj}} &= \Phi_{obj}\left(-\frac{4r_e^3 + 3c_1 r_e^2 + 2c_0 r_e}{r_e^2(r_e^2 + c_1 r_e + c_0)}\right)\frac{r_e}{\Phi_{obj}} \\ &= \left(-\frac{4r_e^2 + 3c_1 r_e^1 + 2c_0}{r_e^2 + c_1 r_e + c_0}\right)\end{aligned} \tag{4.14}$$

This expression ranges from -2 to -4, and describes the logarithmic slope of the effective distance.

4.2.1.2 Pulsed TOF

For Pulsed TOF, the effective distance was derived from the ratio of the two windows W_1 and W_2 as following:

$$r_e = r_0 \frac{W_1}{W_2} \tag{4.15}$$

From Chapter 3, the windows W_2 and consequently W_1 can be described in terms of $\Phi_{obj}(r_e, c_0, c_1, c_2)$

$$\begin{aligned} W_2 &= \Phi_{obj}(r_e, c_0, c_1, c_2) T_p \\ W_1 &= \Phi_{obj}(r_e, c_0, c_1, c_2) T_p \frac{r_e}{r_0} \end{aligned} \tag{4.16}$$

We will now differentiate these quantities with respect to effective distance:

$$\begin{aligned} \frac{\partial W_1}{\partial r_e} &= \frac{\partial \Phi_{obj} T_p \frac{r_e}{r_0}}{\partial r_e} \\ &= \left(\frac{\partial \Phi_{obj}}{\partial r_e} \frac{r_e}{r_0} + \Phi_{obj} \frac{1}{r_0} \right) T_p \\ &= \frac{\Phi_{obj}(r_e) T_p}{r_0} \frac{3r_e^4 + 2c_1 r_e^3 + c_0 r_e^2}{r_e^2 (r_e^2 + c_1 r_e + c_0)} \end{aligned} \tag{4.17}$$

$$\begin{aligned} \frac{\partial W_2}{\partial r_e} &= \frac{\partial}{\partial r_e} \Phi_{obj} T_p \\ &= \left(\frac{\partial \Phi_{obj}}{\partial r_e} \right) T_p \\ &= \Phi_{obj}(r_e) T_p \frac{4r_e^3 + 2c_1 r_e^2 + 2c_0 r_e}{r_e^2 (r_e^2 + c_1 r_e + c_0)} \end{aligned} \tag{4.18}$$

If we take the ratio of these two quantities just as we would do for their non-differentiated forms, we obtain:

$$\begin{aligned} \frac{\frac{\partial W_1}{\partial r_e}}{\frac{\partial W_2}{\partial r_e}} &= \frac{\frac{\Phi_{obj}(r_e) T_p}{r_0} \frac{3r_e^4 + 2c_1 r_e^3 + c_0 r_e^2}{r_e^2 (r_e^2 + c_1 r_e + c_0)}}{\Phi_{obj}(r_e) T_p \frac{4r_e^3 + 2c_1 r_e^2 + 2c_0 r_e}{r_e^2 (r_e^2 + c_1 r_e + c_0)}} \\ &= \frac{r_e}{r_0} \frac{3r_e^2 + 2c_1 r_e + c_0}{4r_e^2 + 2c_1 r_e + 2c_0} \end{aligned} \tag{4.19}$$

Compare this two a standard time of flight measurement obtained by the non-differentiated forms:

$$\frac{W_1}{W_2} = \frac{\Phi_{obj}(r_e)T_p\frac{r_e}{r_0}}{\Phi_{obj}(r_e)T_p} \tag{4.20}$$

$$= \frac{r_e}{r_0} \tag{4.21}$$

We notice two things. First, the time of flight term $\frac{r_e}{r_0}$ term persists through the differentiation process. Secondly, the result has another dimensionless term dependent on the object parameters c_0, c_1 and r_e. We will revisit this term later.

4.2.1.3 SWM TOF

For Sine Wave Modulated Time of Flight, the time of flight information is encoded in the phase of the received signal. This phase is obtained ratiometricly by measuring two orthogonal components of the signal. These two orthogonal components can be approximated similarly to Pulsed TOF as follows:

$$x_I = \Phi_{obj}(r_e)\cos(kr_e - \phi_0) \tag{4.22}$$

$$x_Q = \Phi_{obj}(r_e)\sin(kr_e - \phi_0) \tag{4.23}$$

where $k = 2\frac{\omega_c}{c}$, representing the conversion factor between phase and effective distance. Note the factor of two due to the incident and return path of the optical signal, differing from the optics definition of wave number.

We will now study the properties of the derivative, $\frac{\partial x}{\partial r_e}$ using the polar form notation as shown in equation 3.21:

$$\frac{\partial x}{\partial r_e} = \frac{\partial}{\partial r_e}\left(\Phi_{obj}(r_e)e^{j(kr_e-\phi_0)}\right) \tag{4.24}$$

$$= \frac{\partial \Phi_{obj}}{\partial r_e}\frac{\partial r_e}{\partial t}e^{j(kr_e-\phi_0)} + jk\Phi_{obj}(r_e)e^{j(kr_e-\phi_0)} \tag{4.25}$$

$$= \left(\frac{\partial \Phi_{obj}}{\partial r_e} + jk\Phi_{obj}\right)e^{j(kr_e-\phi_0)} \tag{4.26}$$

Substituting our expression for $\frac{\partial \Phi_{obj}}{\partial r_e}$, we get:

$$\frac{\partial x}{\partial r_e} = \left(\frac{4r_e^3 + 3c_1 r_e^2 + 2c_0 r_e}{r_e^2(r_e^2 + c_1 r_e + c_0)} + jk \right) \Phi_{obj}(r_e) e^{j(kr_e - \phi_0)} \tag{4.27}$$

the phase of this signal is given by:

$$\angle \frac{\partial x}{\partial r_e} = \tan^{-1}\left(-kr_e \frac{r_e^2 + c_1 r_e + c_0}{4r_e^2 + 3c_1 r_e + 2c_0} \right) + kr_e - \phi_0 \tag{4.28}$$

$$\tag{4.29}$$

We are once again left with an expression that closely resembles the non-differentiated time of flight response, but with an additional dimensionless term that is a function of c_0. c_1, and r_0. In fact, if the range of distances present in the system are relatively small such as is the case for the ISL29200, we can make the small angle approximation $tan(x) \approx x$, resulting in the following expression:

$$\angle \frac{\partial x}{\partial r_e} \approx \left(1 - \frac{r_e^2 + c_1 r_e + c_0}{4r_e^2 + 3c_1 r_e + 2c_0} \right) kr_e - \phi_0 \tag{4.30}$$

$$\approx \left(\frac{3r_e^2 + 2c_1 r_e + c_0}{4r_e^2 + 3c_1 r_e + 2c_0} \right) kr_e - \phi_0 \tag{4.31}$$

the same exact dimensionless term as that for Pulsed TOF. We will name this dimensionless term *Distortion Coeffecient*, and will discuss it's significance in further detail in section 4.2.3.

4.2.2 Differentiation with respect to Object Parameters c_0, c_1, and c_2

Although differentiation with respect each of the Object Parameters result in a different expression, their effects are all similar in that they affect the intensity, but not the time of flight. To illustrate this, we will once again consider the derivative of the components for each type of system.

For a Pulsed TOF system, the derivative with respect to the parameters become:

$$\frac{\partial W_2}{\partial c_0} = \frac{\partial \Phi_{obj}}{\partial c_0} T_p \;,\; \frac{\partial W_1}{\partial c_0} = \frac{\partial \Phi_{obj}}{\partial c_0} T_p \frac{r_e}{r_0} \tag{4.32}$$

$$\frac{\partial W_2}{\partial c_1} = \frac{\partial \Phi_{obj}}{\partial c_1} T_p \;,\; \frac{\partial W_1}{\partial c_1} = \frac{\partial \Phi_{obj}}{\partial c_1} T_p \frac{r_e}{r_0} \tag{4.33}$$

$$\frac{\partial W_2}{\partial c_2} = \frac{\partial \Phi_{obj}}{\partial c_2} T_p \;,\; \frac{\partial W_1}{\partial c_2} = \frac{\partial \Phi_{obj}}{\partial c_2} T_p \frac{r_e}{r_0} \tag{4.34}$$

$$\frac{\frac{\partial W_1}{\partial c_0}}{\frac{\partial W_2}{\partial c_0}} = \frac{\frac{\partial W_1}{\partial c_1}}{\frac{\partial W_2}{\partial c_1}} = \frac{\frac{\partial W_1}{\partial c_2}}{\frac{\partial W_2}{\partial c_2}} = \frac{r_e}{r_0} = \frac{W_1}{W_2} \tag{4.35}$$

As can be seen, all of the derivative terms with the exception of r_e have no effect on the time of flight computed. A similar effect is true for SWM TOF systems:

$$\frac{\partial x_I}{\partial c_0} = \frac{\partial \Phi_{obj}}{\partial c_0} \cos(kr_e) \;,\; \frac{\partial x_Q}{\partial c_0} = \frac{\partial \Phi_{obj}}{\partial c_0} \sin(kr_e) \tag{4.36}$$

$$\frac{\partial x_I}{\partial c_1} = \frac{\partial \Phi_{obj}}{\partial c_1} \cos(kr_e) \;,\; \frac{\partial x_Q}{\partial c_1} = \frac{\partial \Phi_{obj}}{\partial c_1} \sin(kr_e) \tag{4.37}$$

$$\frac{\partial x_I}{\partial c_2} = \frac{\partial \Phi_{obj}}{\partial c_2} \cos(kr_e) \;,\; \frac{\partial x_Q}{\partial c_2} = \frac{\partial \Phi_{obj}}{\partial c_2} \sin(kr_e) \tag{4.38}$$

$$\angle\left(\frac{\partial x}{\partial c_0}\right) = \angle\left(\frac{\partial x}{\partial c_1}\right) = \angle\left(\frac{\partial x}{\partial c_2}\right) = kr_e = \angle(x) \tag{4.39}$$

This indicates that for a change in only one or more of the object parameters c_0, c_1, or c_2, computing the time-of-flight of the derivative results in the exact same result as the original signal.

4.2.3 Differential TOF and Distortion Coeffecient

The implications of these results are quite surprising. First of all, we find that when we differentiate the components of an TOF measurement (i.e. W_1/W_2 for Pulsed TOF, x_I/x_Q for SWM TOF), the ratio of the two differentiated measurements form a one to one relationship between effective distance given a the object parameters c_0, c_1 and c_2. Secondly, this function is the same function for solving for a standard TOF with a relatively simple correction term, which we will call the *Distortion Coeffecient* ζ.

$$\zeta = \frac{\frac{\partial W_1}{\partial t}}{\frac{\partial W_2}{\partial t}} \frac{r_0}{r_e} \quad \text{for Pulsed TOF} \tag{4.40}$$

$$\zeta = \left(\angle \frac{\partial x}{\partial t} + \phi_0 \right) \frac{1}{k r_e} \quad \text{for SMW TOF} \tag{4.41}$$

This term is dimensionless, and is different depending on the kind of change observed. For a change in one or more of the parameters c_0, c_1, or c_2, this factor is simply unity. For a change only in effective distance r_e (i.e. $\frac{\partial c_i}{\partial t} = 0$ for $i = 0, 1, 2$), this term is

$$\zeta_r = \frac{3r_e^2 + 2c_1 r_e + c_0}{4r_e^2 + 2c_1 r_e + 2c_0} \tag{4.42}$$

This value is bounded between $\frac{1}{2}$ and $\frac{3}{4}$. In fact, it traces from $\frac{1}{2}$, to $\frac{2}{3}$, and then to $\frac{3}{4}$ exactly as the logarithmic slope traces from -2 to -3, and finally to -4. This can be proven by locally modeling our signal intensity as follows:

$$\Phi_{obj}(r_e) = A(r_e)(r_e)^b \tag{4.43}$$

$$\frac{\partial \Phi_{obj}}{\partial r_e}(r_e) = bA(r_e)(r_e)^{b-1} \tag{4.44}$$

$$\Phi_{obj}(r_e + \delta r_e) \approx A(r_e)(r_e + \delta r_e)^b \tag{4.45}$$

The solution to this equation is given by:

$$\begin{aligned} b &= \frac{r_e \frac{\partial \Phi_{obj}}{\partial r_e}}{\Phi_{obj}} \\ &= \frac{1}{1 - \zeta_r} \end{aligned} \tag{4.46}$$

This is consistent with the observations made in the paper attached in Appendix A, where the differentiated signal has a time of flight of $1 - \frac{1}{N}$, where N is the power law of the signal with respect to distance.

This indicates that if the values of c_0 and c_1 are known *a priori*, it is possible to obtain the effective distance with *only knowledge of the differentiated time of flight signals.*

4.3 Use Cases and Examples of Real Time Extraction Techniques

Using the identities developed above, we will now consider methods to extract properties of the object including distance in various scenarios. The techniques involved will depend highly on the scenario, so we will consider several use cases and discuss possible techniques that can be used in each case. For Pulsed TOF, we will consider the quantities W_1 and W_2 (and as a result, W_1) to be readily available, as well as their derivatives $\frac{\partial W_1}{\partial t}$, $\frac{\partial W_2}{\partial t}$. We will also introduce their object parameters c_0, c_1, c_2 as necessary. Φ_0, A_D, T_p, r_0, and are all considered to be known fixed constants.

For SWM TOF we will consider the quantities x_I, x_Q, $\frac{\partial x_I}{\partial t}$, $\frac{\partial x_Q}{\partial t}$, readily available, and will introduce c_0, c_1, c_2 as necessary. Φ_0, A_D, k, and ϕ_0 are known fixed constants.

4.3.1 Single Object

We will first consider the simple scenario where there is only a single object in the field of view. In a physical system, this occurs when the background is is sufficiently far or sufficiently non-reflective (at least in the direction of the sensor), such that for the range of interest, the background term is negligible compared to the reflections from the object. (i.e. $\Phi_{bg}(r_e) << \Phi_{obj}(r_e)$ for $r_e < r_m ax$).

Under this scenario, the effective distance is trivial to extract by definition. Thus, we would simply apply the conversion equations for the particular time of flight system, and obtain the effective distance.

$$r_e = r_0 \frac{W_1}{W_2} \qquad \text{for Pulsed TOF} \tag{4.47}$$

$$r_e = \frac{1}{k} \tan^{-1}\left(\frac{x_Q}{x_I}\right) \qquad \text{for SWM TOF} \tag{4.48}$$

However, due to the redundant information in the intensity, we can do a little better than this. We will first obtain the time derivative of the intensity $\frac{\partial A}{\partial t}$, the instantaneous intensity Φ_{obj}, the effective distance r_e, and the derivative of the effective distance $\frac{\partial r_e}{\partial t}$. Now, if we assume that the change in object parameters c_0, c_1, and c_2 are small, we can estimate the effective power law b by examining the ratio of normalized rate of change of intensity and effective distance:

$$b' = \frac{1}{\Phi_{obj}} \frac{\partial \Phi_{obj}}{\partial t} \left(\frac{1}{r_e} \frac{\partial r_e}{\partial t}\right)^{-1} \tag{4.49}$$

When $\frac{\partial \Phi_{obj}}{\partial t}$ is purely due to change in effective distance (i.e. $\frac{\partial \Phi_{obj}}{\partial t} = \frac{\partial \Phi_{obj}}{\partial r_e} \frac{\partial r_e}{\partial t}$), this becomes equal to the power law b as shown in equation 4.46

Change in c_0, c_1 or c_2 will result in an inflation or deflation in $\frac{\partial \Phi_{obj}}{\partial t}$. This effect can be essentially ignored if all of the following is true:

$$\left|\frac{\partial \Phi_{obj}}{\partial c_0} \frac{\partial c_0}{\partial t}\right| << \left|\frac{\partial}{\partial r_e} \Phi_{obj} \frac{\partial r_e}{\partial t}\right| \tag{4.50}$$

$$\left|\frac{\partial \Phi_{obj}}{\partial c_1} \frac{\partial c_1}{\partial t}\right| << \left|\frac{\partial}{\partial r_e} \Phi_{obj} \frac{\partial r_e}{\partial t}\right| \tag{4.51}$$

$$\left|\frac{\partial \Phi_{obj}}{\partial c_2} \frac{\partial c_2}{\partial t}\right| << \left|\frac{\partial}{\partial r_e} \Phi_{obj} \frac{\partial r_e}{\partial t}\right| \tag{4.52}$$

We will substitute and simply each expression, and it can be shown that it is sufficient for the following to be true:

$$\left|\frac{1}{c_0}\frac{\partial c_0}{\partial t}\right| << \left|2\frac{1}{r_e}\frac{\partial r_e}{\partial t}\right| \tag{4.53}$$

$$\left|\frac{\partial c_1}{\partial t}\right| << \left|4\frac{\partial r_e}{\partial t}\right| \tag{4.54}$$

$$\left|\frac{1}{c_2}\frac{\partial c_2}{\partial t}\right| << \left|2\frac{1}{r_e}\frac{\partial r_e}{\partial t}\right| \tag{4.55}$$

This means that if the precent change in each parameter is significantly smaller than the percent change in effective distance, the estimated power law b' estimated from $\frac{\partial}{\partial t}\Phi_{obj}$ is valid. For example, if the effective distance changes by 10% from 1m to 0.9m, and c_0 changes 2% from $1m^2$ to $0.98m^2$, the error introduced in the estimated power law b' is on the order of $\frac{1}{2}\frac{2\%}{10\%} = 0.1$. On the other hand, if both parameters change by the same rate, the error introduced would be upwards of 50%, making the difference between a square law and forth law.

A similar technique can be done by using the Differential TOF. The TOF computed from the differentiated components ($\frac{\partial W_2}{\partial t}$, $\frac{\partial W_1}{\partial t}$ for Pulsed TOF, $\frac{\partial x_I}{\partial t}$, $\frac{\partial x_Q}{\partial t}$ for SWM TOF) has the property that it is equal to the TOF computed form the non-differentiated values, but scaled by the distortion coeffecient ζ. Thus, we can solve for ζ as follows:

$$\zeta = \frac{\partial W_1}{\partial t}\left(\frac{\partial W_2}{\partial t}\right)^{-1}\frac{W_2}{W_1} \qquad \text{for Pulsed TOF} \tag{4.56}$$

$$\zeta = \frac{\angle\left(\frac{\partial x}{\partial t}\right)}{\angle x} \qquad \text{for SMW TOF} \tag{4.57}$$

$$\tag{4.58}$$

If the if the object parameters are kept constant, (i.e. $\frac{\partial}{\partial t}c_i = 0$ for $i = 0, 1, 2$), $\zeta = \zeta_r$, and this value can than be converted to an estimate of the power law using the identity:

$$b \approx 1 - \frac{1}{\zeta_r(r_e)} \tag{4.59}$$

This technique is also limited by the constrains set in Equation 4.53.

4.3.2 Single Object w/ Crosstalk

We will now consider the scenario where crosstalk is superimposed on top of the desired signal. From Equation 3.22 and 3.23 , we have:

$$\begin{aligned}
W_1' &= W_1 + CT_1 \\
W_2' &= W_2 + CT_2 && \text{for Pulsed TOF} \\
x_I' &= x_I + CT_I \\
x_Q' &= x_Q + CT_Q && \text{for SWM TOF}
\end{aligned}$$

where W_1', W_2' and x_I', x_Q' are the two observed quantities, and W_1, W_2 and x_I, x_Q are the natural response in the absence of crosstalk. In the existence of crosstalk, both the time of flight information and intensity information are contaminated, and will result in erroneous time of flight and parameter information if the same technique as a single object scenario is used. We will consider several scenarios and discuss the techniques that can mitigate this error.

4.3.2.1 Known Crosstalk

Although this technique does not strictly rely on the concepts developed in this chapter, we will include this here to contrast with what is to come. If the crosstalk can be quantified, it can simply be subtracted out of the signal, and the problem reduces itself to the Single Object Problem. This is contrasted with cases where the crosstalk cannot be quantified *a priori*.

$$r_e = \left(1 - \frac{W_1' - CT_1}{W_2' - CT_2}\right) r_0 \qquad \text{for Pulsed TOF} \tag{4.60}$$

$$r_e = \frac{1}{k} \tan^{-1}\left(\frac{x_Q' - CT_Q}{x_I' - CT_I}\right) \qquad \text{for SWM TOF} \tag{4.61}$$

4.3.2.2 Unknown Crosstalk

This is now a much more difficult problem, as we must remove the effect of an unknown but constant signal. However, we are not completely powerless as we would be if only time-of-flight information was recorded. Because crosstalk does not change over time, differentiating the TOF components with respect to time would make the crosstalk terms vanish. We will also include the convenience function $W_1 = W_2 - W_1$ for clarity.

$$\begin{aligned} \frac{\partial W_1'}{\partial t} &= \frac{\partial (W_1 + CT_1)}{\partial t} = \frac{\partial W_1}{\partial t} \\ \frac{\partial W_2'}{\partial t} &= \frac{\partial (W_2 + CT_2)}{\partial t} = \frac{\partial W_2}{\partial t} \\ \frac{\partial W_1'}{\partial t} &= \frac{\partial (W_2' - W_1')}{\partial t} = \frac{\partial W_1}{\partial t} \qquad \text{for Pulsed TOF} \end{aligned} \tag{4.62}$$

Similarly,

$$\begin{aligned} \frac{\partial x_I'}{\partial t} &= \frac{\partial (x_I + CT_I)}{\partial t} = \frac{\partial x_I}{\partial t} \\ \frac{\partial x_Q'}{\partial t} &= \frac{\partial (x_Q + CT_Q)}{\partial t} = \frac{\partial x_Q}{\partial t} \qquad \text{for SWM TOF} \end{aligned} \tag{4.63}$$

Now, by using the differentiated TOF components, we are still able to extract the time of flight with a factor of the distortion coeffecient $\zeta(r_e)$.

$$\frac{\frac{\partial W_1}{\partial t}}{\frac{\partial W_2}{\partial t}} = \frac{r_e}{r_0}\zeta \qquad \text{for Pulsed TOF} \tag{4.64}$$

$$\angle\frac{\partial x}{\partial t} \approx k r_e \zeta(r_e) - \phi_0 \qquad \text{for SMW TOF} \tag{4.65}$$

Case 1: Fixed Distance The first scenario we will consider is the case where the effective distance of the target object stays constant (i.e. $\frac{\partial r_e}{\partial t} = 0$). Examples of this include when the object is traversing the field of view at a fixed radius, or a small object rotating around it's own axis. A person shifting around in the field of view of the sensor would likely approximate to this scenario. In this case, the Distortion Coeffecient is equal to unity, ($\zeta = 1$), indicating that the time-of-flight computed from the differential components are equal to the time-of-flight that would have been computed in the absence of crosstalk. In this case, the effective distance is given by a function interns of just the differential components, i.e. $r_e = f(\frac{\partial W_1}{\partial t}, \frac{\partial W_2}{\partial t})$ for Pulsed TOF, $r_e = f(\angle\frac{\partial x}{\partial t})$ for SWM TOF.

$$\begin{aligned} r_e &= \zeta \frac{\frac{\partial W_1}{\partial t}}{\frac{\partial W_2}{\partial t}} \\ &= \frac{\frac{\partial W_1}{\partial t}}{\frac{\partial W_2}{\partial t}} \end{aligned} \tag{4.66}$$

$$\begin{aligned} r_e &= \zeta \frac{1}{k}\left(\angle\frac{\partial x}{\partial t} + \phi_0\right) \\ &= \frac{1}{k}\left(\angle\frac{\partial x}{\partial t} + \phi_0\right) \end{aligned} \tag{4.67}$$

Case 2: Change in distance, w/ known $\zeta(r_e)$ If the object parameters c_0 and c_1 are known fixed constants, ζ can be fully described as a function of r_e. In this scenario, it is possible to solve for r_e given a particular combination of $\frac{\partial W_1}{\partial r_e}$ and $\frac{\partial W_2}{\partial r_e}$, or $\frac{\partial x_I}{\partial r_e}$ and $\frac{\partial x_Q}{\partial r_e}$.

For the case of Pulsed TOF, we must simply solve the equation 4.19. This relationship reduces to a third order polynomial in r_e, which can be explicitly solved.

Although third order polynomials generally have 3 solutions, choosing the only real and positive solution will result in the correct effective distance r_e. This results in an equation for r_e in terms of the derivatives $\frac{\partial W_1}{\partial t}$, $\frac{\partial W_2}{\partial t}$, and the object parameters c_0, c_1, i.e. $r_e = f(\frac{\partial W_1}{\partial t}, \frac{\partial W_2}{\partial t}, c_0, c_1)$

$$a_3 r_e^3 + a_2 r_e^2 + a_1 r_e + a_0 = 0 \tag{4.68}$$

where:

$$\begin{aligned}
a_3 &= \frac{3}{r_0}\frac{\partial W_2}{\partial r_e} \\
a_2 &= \frac{2c_1}{r_0}\frac{\partial W_2}{\partial r_e} - 4\frac{\partial W_1}{\partial r_e} \\
a_1 &= \frac{c_0}{r_0}\frac{\partial W_2}{\partial r_e} - 3c_1\frac{\partial W_1}{\partial r_e} \\
a_0 &= -2c_0\frac{\partial W_1}{\partial r_e}
\end{aligned}$$

In the case of SWM TOF, analytic solutions do not exist for the general case, but numerical solutions can be obtained to Equation 4.28. Alternatively, using the small approximations as shown in Equation 4.31, we can reduce this relation to a third order polynomial similar to the Pulsed TOF case. Similarly to the Pulsed TOF case, we obtain $r_e = f(\frac{\partial x_I}{\partial t}, \frac{\partial x_Q}{\partial t}, c_0, c_1)$

$$a_3 r_e^3 + a_2 r_e^2 + a_1 r_e + a_0 = 0 \tag{4.69}$$

where:

$$\begin{aligned}
a_3 &= 3k \\
a_2 &= 2kc_1 - 4\left(\angle\frac{\partial x}{\partial r_e} + \phi_0\right) \\
a_1 &= kc_0 - 3c_1\left(\angle\frac{\partial x}{\partial r_e} + \phi_0\right) \\
a_0 &= -2c_0\left(\angle\frac{\partial x}{\partial r_e} + \phi_0\right)
\end{aligned}$$

Case 3: Change in distance, w/ unknown $\zeta(r_e)$ Unfortunately, $\zeta(r_e)$ is typically an unknown parameter. The $\zeta(r_e)$ contributed from a change in effective distance is bounded between $\frac{1}{2}$ and $\frac{3}{4}$, and the ζ contributed from changes in one of the object parameters c_0, c_1, or c_2 is equal to unity. Thus, if we can constrain the object such that there is change in at most one of these parameters, we can definitively constrain the effective distance to within a factor of two. However, if there is a change in more than one of these parameters, there is a risk of the contributions canceling each other out. This occurs when $\frac{\partial \Phi_{obj}}{\partial r_e}\frac{\partial r_e}{\partial t}$ is not the same sign as $\frac{\partial \Phi_{obj}}{\partial c_x}\frac{\partial c_x}{\partial t}$, resulting in the change in amplitude canceling each other out. An clear example of this is visible in Figure 3-8 depicting the effective distance v.s. intensity curve for off-axis linear motion. In this graph, one can see a region where the logarithmic slope is flat. Using the differentiated components to measure time-of-flight relies on the existence of change in intensity of the signal, and thus any region where the intensity of the signal is constant with a change in effective distance is a clear problem. Due to the ratiometric nature of the conversion, a positive logarithmic slope is not necessarily a problem as long as it is sufficiently steep, but a flat region indicates a region where ζ is ill behaved.

Although the general case has it's limitations, limiting the scope to certain surface types, and certain distances can also result in powerful capabilities. For example, limiting the scope to diffuse objects (thereby decreasing the variability in c_0, c_1 and c_2) alone allows the effective distance to be determined within a factor of 25%, by asserting $\zeta = 0.6123\%$. If one limits this to short range uses where the ζ is always around $\frac{1}{2}$, the effective distance can be determined with a fair amount of accuracy with out calibration. Alternatively, using the techniques for known $\zeta(r_e)$ with a very rough approximation of c_0 and c_1 can also be effective, For example, even with an order of magnitude error in each of c_0 and c_1, error is limited to around 20%.

Figures 4-1 and 4-2 show hese results for a typical set of signals, for a range of values for r_e with a modest levels of crosstalk. We will collectively refer to the techniques that use the ratios of the differential forms of the TOF components as *Differential Time-Of-Flight* (DTOF).

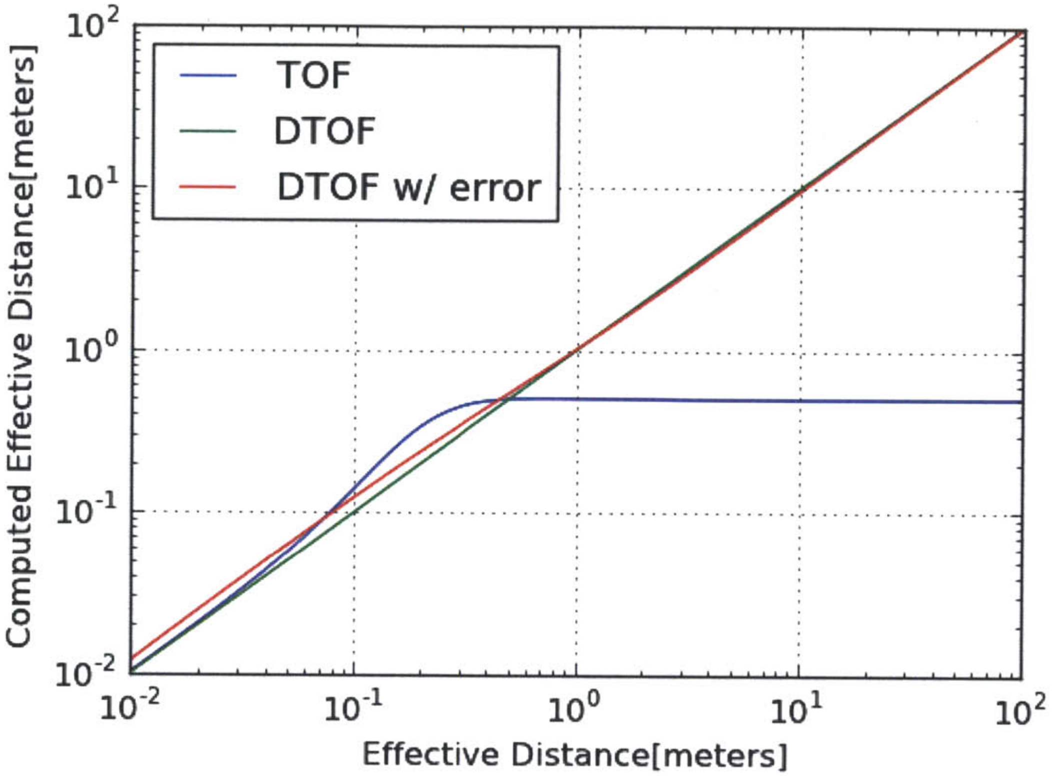

Figure 4-1: Comparison of Conventional TOF and DTOF techniques in the presence of a Unknown Cross Talk

4.3.3 Single Object w/ Uniform Background

The presence of a uniform background is a yet even more difficult problem to solve. The signal intensity of the contribution from the background is dependent on the effective distance, and therefore shows up as another error source. For a pure time-of-flight system or an intensity based sensor, this problem is hopeless, as the signals are completely indistinguishable from an object at a different distance. However, using the redundant information available in both information, we can do much better using hybrid techniques.

From Chapter 3, the background signal is characterized in the following way:

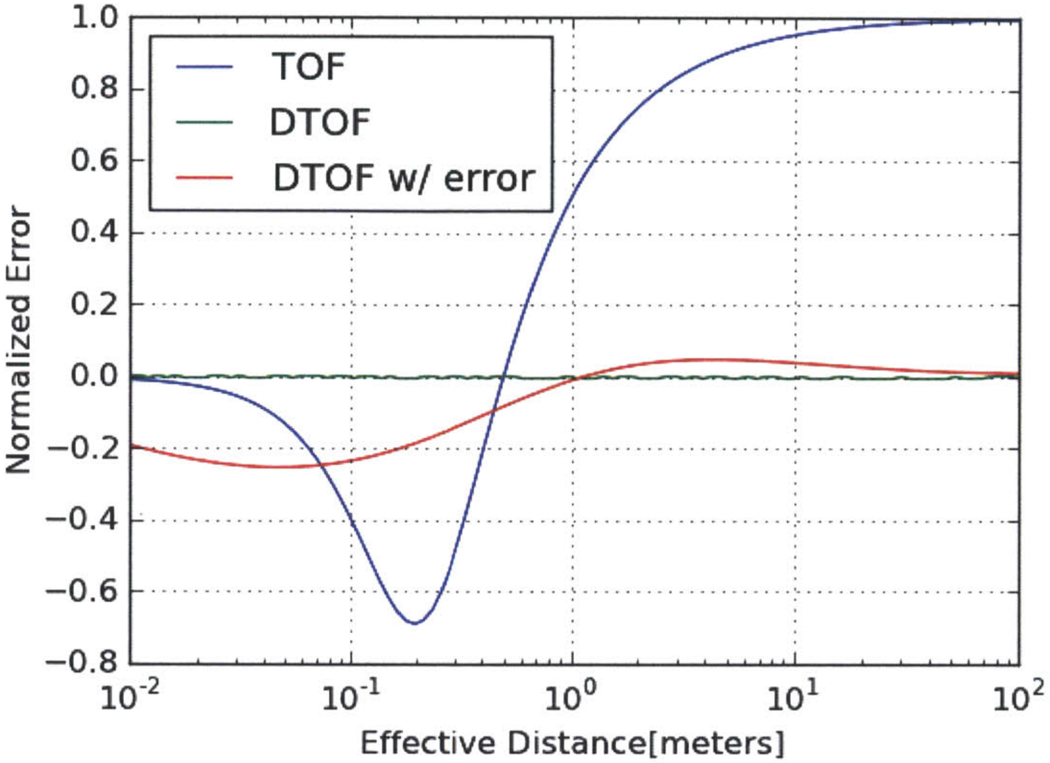

Figure 4-2: Error from Conventional TOF and DTOF techniques in the presence of Unknown Cross Talk

$$
\begin{aligned}
BG_1 &= \Phi_{bg}(r_e, \Phi_{BG}, c_0', c_1')T_p\left(1 - \frac{R}{r_0}\right) \\
BG_2 &= \Phi_{bg}(r_e, \Phi_{BG}, c_0', c_1')T_p \qquad (4.70) \\
W_1' &= W_1(r_e, c_0, c_1, c_2) + BG_1(r_e, c_0', c_1') \\
W_2' &= W_2(r_e, c_0, c_1, c_2) + BG_2(r_e, c_0', c_1') \qquad (4.71)
\end{aligned}
$$

We once again have two equations, one unknown, but with up to seven parameters, $c_0, c_1, c_2, c_0', c_1', \Phi_{BG}, R$. However, we can eliminate some of these with some algebra. We have two options: one is to eliminate the background term, the other is to eliminate the object term.

4.3.3.1 Eliminating the Background Term

$$W_2' = W_2(r_e, c_0, c_1, c_2) + \Phi_{bg}(r_e, \Phi_{BG}, c_0', c_1')T_p$$
$$W_1' = W_1(r_e, c_0, c_1, c_2) + \Phi_{bg}(r_e, \Phi_{BG}, c_0', c_1')T_p\frac{R}{r_0}$$

Isolating the background term:

$$W_2' - W_2(r_e, c_0, c_1, c_2) = \Phi_{bg}(r_e, \Phi_{BG}, c_0', c_1')T_p$$
$$\frac{r_0}{R}(W_1' - W_1(r_e, c_0, c_1, c_2)) = \Phi_{bg}(r_e, \Phi_{BG}, c_0', c_1')T_p$$

Equating both LHS:

$$W_2' - W_2(r_e, c_0, c_1, c_2) = \frac{r_0}{R}(W_1' - W_1(r_e, c_0, c_1, c_2))$$

Writing out the full equations:

$$W_2' - \Phi_0 A_D \frac{c_0 c_2}{r_e^2(r_e^2 + c_1 r_e + c_0)}T_p = \frac{r_0}{R}\left(W_1' - \Phi_0 A_D \frac{c_0 c_2}{r_e^2(r_e^2 + c_1 r_e + c_0)}T_p \frac{r_e}{r_0}\right) \quad (4.72)$$

Converting this to polynomial form, we reach a 4th order polynomial.

$$a_4 r_e^4 + a_3 r_e^3 + a_2 r_e^2 + a_1 r_e + a_0 = 0 \quad (4.73)$$

where:

$$a_4 = W_2' - \frac{r_0}{R}W_1'$$
$$a_3 = \left(W_2' - \frac{r_0}{R}W_1'\right)c_1$$
$$a_2 = \left(W_2' - \frac{r_0}{R}W_1'\right)c_0$$
$$a_1 = \Phi_0 A_D T_p c_0 c_2 \frac{1}{R}$$
$$a_0 = -\Phi_0 A_D T_p c_0 c_2$$

Solving this polynomial would result in the successful extraction of the effective distance r_e. This requires the object parameters c_0, c_1, c_2 and the distance of the background to be known *a priori* (i.e. $r_e = f(W_1', W_2', c_0, c_1, c_2, R)$), but enables the system to compute the effective distance much further than the range allowed by a conventional TOF system. However, this polynomial potentially has multiple positive real roots, and it may be up to the user or higher level algorithms to select the correct root. We will refer to this technique as *Background Cancelling Time-Of-Flight* (BCTOF).

Figures 4-3 and 4-4 show the results of applying these equations for a typical set of signals, for a range of values for r_e with a background located at a distance of 10m. When an error is introduced in each of the parameters, the solutions start to diverge as the background signal gets stronger, but an order of magnitude improvement in usable range is still seen compared to conventional TOF. In general, the errors seem to be proportionally large for an error in c_2 and R, but are relatively small for an error in c_0 and c_1.

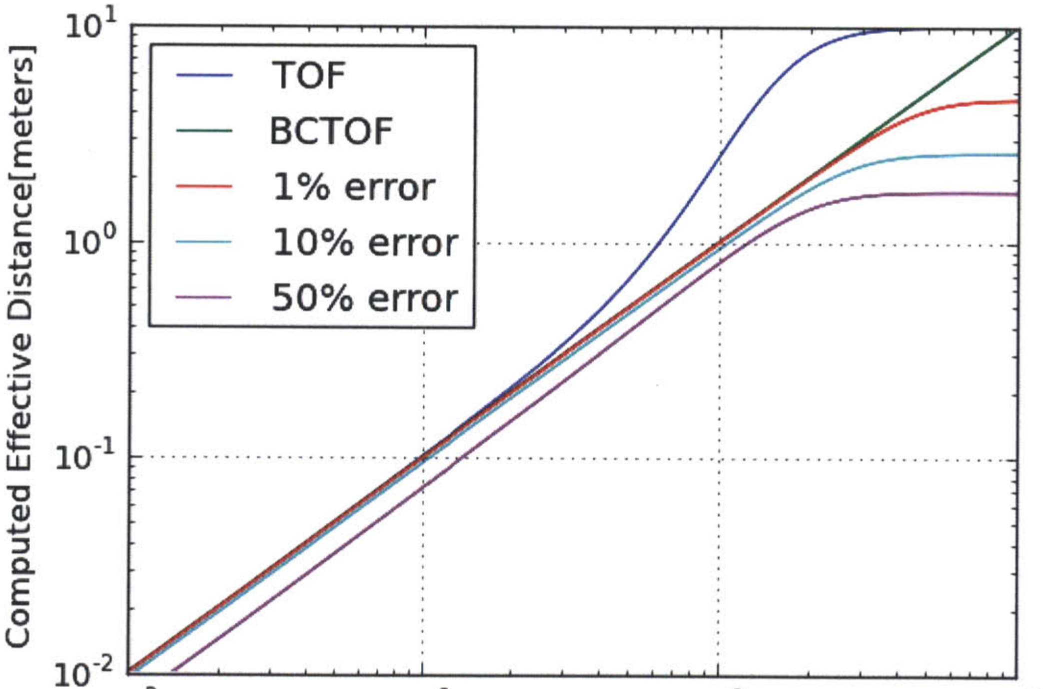

Figure 4-3: Effective Distance Computed from BCTOF

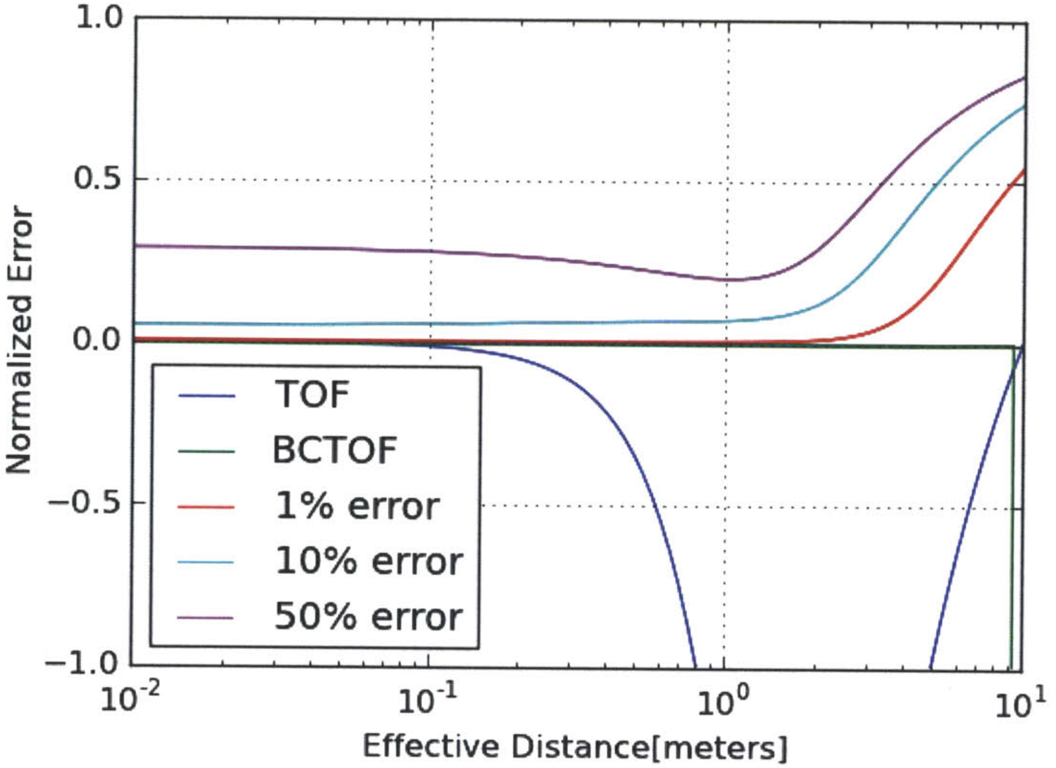

Figure 4-4: Normalized Error from BCTOF

4.3.3.2 Eliminating the Object Term

Similarly to the background term case, we will eliminate the dependancy on c_0, c_1, c_2 from both equations.

$$W_2' - BG_2(r_e, c_0', c_1') = W_2(r_e, c_0, c_1, c_2) \tag{4.74}$$

$$\begin{aligned} W_1' - BG_1(r_e, c_0', c_1') &= W_1(r_e, c_0, c_1, c_2) \\ &= W_2(r_e, c_0, c_1, c_2)\frac{r_e}{r_0} \end{aligned} \tag{4.75}$$

Solving for $W_2(r_e, c_0, c_1, c_2)$

$$W_2' - BG_2(r_e, c_0', c_1') = \frac{r_0}{r_e}(W_1' - BG_1(r_e, c_0', c_1'))$$

Writing out the full equations:

$$W_2' - \Phi_{BG}\frac{r_e^2 + c_1' r_e}{r_e^2 + c_1' r_e + c_0'}T_p = \frac{r_0}{r_e}\left(W_1' - \Phi_{BG}\frac{r_e^2 + c_1' r_e}{r_e^2 + c_1' r_e + c_0'}T_p\frac{R}{r_0}\right) \tag{4.76}$$

Transforming this to polynomial form will result in a 3rd order polynomial in r_e, resulting in an equation for effective distance in the form $r_e = f(W_1', W_2', c_0', c_1', \Phi_{BG}, R)$ Because this technique essentially relies on the intensity behavior of the background, we will refer to this technique as *Background Intensity.*

4.3.4 Single Object w/ Uniform Background and Unknown Crosstalk

We will now consider when both a uniform background and crosstalk are present.

$$\begin{aligned} W_1' &= W_1(r_e, c_0, c_1, c_2) + BG_1(r_e, c_0', c_1') + CT_1 \\ W_2' &= W_2(r_e, c_0, c_1, c_2) + BG_2(r_e, c_0', c_1') + CT_2 \end{aligned} \tag{4.77}$$

In this scenario, the background cancellation method above will result in erroneous results. Using Differential TOF as we did in the scenario with only crosstalk won't work either, as the background is also a function of effective distance. Figure 4-5 shows the results of applying Differential TOF and Background Canceling TOF techniques on a signal that contains both background and crosstalk. As can be seen, both perform better than conventional Time-Of-Flight, but become unusable as the unexpected error source becomes more significant.

If the crosstalk can be measured independently, this problem simples down to a background cancellation problem, by simply subtracting the crosstalk. If this is not possible, we must consider a different approach, using concepts from both Differential TOF and Background cancellation techniques.

We will use the TOF components W_2 and W_1 in their differentiated form:

$$\frac{\partial W_2}{\partial t} = \frac{\partial W_2}{\partial r_e}\frac{\partial r_e}{\partial t} + \sum_{i=0}^{2} \frac{\partial W_1}{\partial c_i}\frac{\partial c_i}{\partial t} \tag{4.78}$$

$$\frac{\partial W_1}{\partial t} = \frac{\partial W_1}{\partial r_e}\frac{\partial r_e}{\partial t} + \sum_{i=0}^{2} \frac{\partial W_1}{\partial c_i}\frac{\partial c_i}{\partial t} \tag{4.79}$$

However, the actual measured signal includes the background signal, resulting in

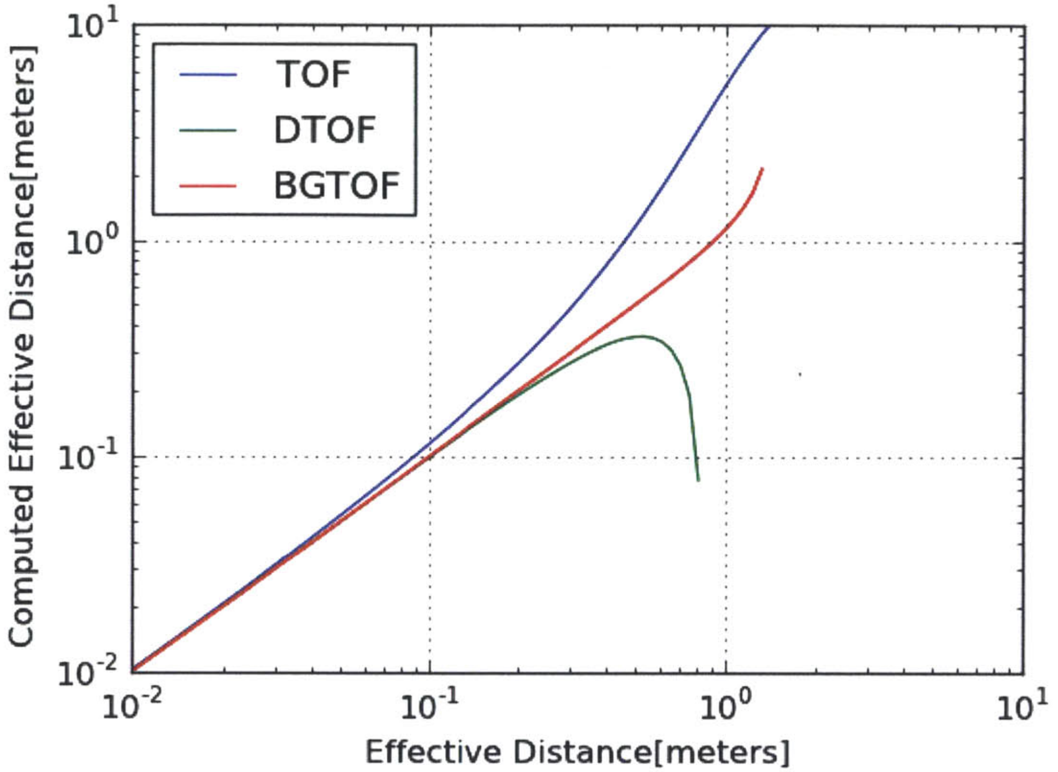

Figure 4-5: TOF, D-TOF and BC TOF Techniques on a signal containing both Background and Crosstalk

the following measured quantities:

$$\begin{aligned} \frac{\partial W_2'}{\partial t} &= \frac{\partial W_2}{\partial t} + \frac{\partial BG_2}{\partial t} \\ &= \frac{\partial W_2}{\partial t} + \frac{\partial \Phi_{bg}}{\partial t} T_p \qquad (4.80) \\ \frac{\partial W_1'}{\partial t} &= \frac{\partial W_1}{\partial t} + \frac{\partial BG_1}{\partial t} \\ &= \frac{\partial W_1}{\partial t} + \frac{\partial \Phi_{bg}}{\partial t} T_p \frac{R}{r_0} \qquad (4.81) \end{aligned}$$

Once again, we have a two equations, which we can combine to eliminate some parameters. Now solving this expression completely requires us to know all the relative strengths of the partial derivatives $\frac{\partial r_e}{\partial t}$, $\frac{\partial c_0}{\partial t}$, $\frac{\partial c_0}{\partial t}$, and $\frac{\partial c_0}{\partial t}$. We will solve this for the case where the object parameters are kept constant (i.e. $\frac{\partial c_i}{\partial t} = 0$ for $i = 0, 1, 2$).

$$\begin{aligned}
\frac{\partial W_2'}{\partial t} &= \left(\frac{\partial W_2}{\partial r_e} + \frac{\partial \Phi_{bg}}{\partial r_e} T_p \right) \frac{\partial r_e}{\partial t} \\
\frac{\partial W_1'}{\partial t} &= \left(\frac{\partial W_1}{\partial r_e} + \frac{\partial \Phi_{bg}}{\partial r_e} T_p \frac{R}{r_0} \right) \frac{\partial r_e}{\partial t} \\
\frac{\frac{\partial W_2'}{\partial t}}{\frac{\partial W_2}{\partial r_e} + \frac{\partial \Phi_{bg}}{\partial r_e} T_p} &= \frac{\partial r_e}{\partial t} \\
\frac{\frac{\partial W_1'}{\partial t}}{\frac{\partial W_1}{\partial r_e} + \frac{\partial \Phi_{bg}}{\partial r_e} T_p \frac{R}{r_0}} &= \frac{\partial r_e}{\partial t}
\end{aligned}$$

Equating both LHS and multiplying through:

$$\frac{\partial W_2'}{\partial t} \left(\frac{\partial W_1}{\partial r_e} + \frac{\partial \Phi_{bg}}{\partial r_e} T_p \frac{R}{r_0} \right) = \frac{\partial W_1'}{\partial t} \left(\frac{\partial W_2}{\partial r_e} + \frac{\partial \Phi_{bg}}{\partial r_e} T_p \right) \tag{4.82}$$

Writing this out fully results in:

$$\begin{aligned}
&\frac{\partial W_2'}{\partial t} \left(\Phi_0 A_D T_p \frac{c_0 c_2 (3r_e^3 + 2c_1 r_e^2 + c_0 r_e)}{r_e^4 (r_e^2 + c_1 r_e + c_0)^2} \frac{r_e}{r_0} + \Phi_{BG} \frac{(r_e^2 + c_1' r_e)(2c_1 r_e' + c_0')}{(r_e^2 + c_1' r_e + c_0')^2} \frac{R}{r_0} T_p \right) \\
&= \frac{\partial W_1'}{\partial r_e} \left(\Phi_0 A_D T_p \frac{c_0 c_2 (4r_e^3 + 3c_1 r_e^2 + 2c_0 r_e)}{r_e^4 (r_e^2 + c_1 r_e + c_0)^2} + \Phi_{BG} \frac{(r_e^2 + c_1' r_e)(2c_1 r_e' + c_0')}{(r_e^2 + c_1' r_e + c_0')^2} T_p \right)
\end{aligned} \tag{4.83}$$

As can be seen from this expression, this equation can be converted to a 10th order polynomial and solved for r_e. However, it is quite likely that multiple positive real roots are possible, and this technique requires both the strength of the background Φ_{BG} and the distance of the background R to be known, as well as the object parameters $c_0, c_1, c_2, c_0', c_1'$. In any practical system, it is likely much easier to quantify the crosstalk than it is to measure additional parameters. We will refer to this technique as *Background Canceling Differential TOF* (BC D-TOF).

4.4 Summary of Real Time Techniques

Table 4.4 summarizes the real time techniques discussed in this chapter. Besides the conventional TOF and intensity based techniques that are commonly used, analysis and simulations shows the feasibility of alternative techniques provide good results even in the presence of crosstalk or background, in exchange for further information about the scene at hand. All of these techniques require the object parameters c_0, c_1, and c_2 to be fixed. Error or changes in these parameters introduce an error in the computed time-of-flght, the significance of which is largely correlated to the complexity of the technique.

While conventional time-of-flight techniques only require the two measurable time-of-flight parameters to compute effective distance, intensity based sensors require one the the two measurable parameters and all three object parameters. Differential TOF uses the differentiated form of the components and is immune to crosstalk but requires c_0 and c_1 for best results. Because this technique is only based off the relative intensities of the two windows, it is quite tolerant of incorrect parameter values. Background Canceling TOF requires all three object parameters and the distance of the background. This technique relies on the intensity heavily, and thus requires an accurate estimate of the object parameters including c_2. All of the above techniques can adjust to crosstalk if the crosstalk information (i.e. $CT_1, CT_2/CT_I, CT_Q$) is known, with the exception of Differential TOF, which is natively immune to crosstalk.

While the conventional time-of-flight technique is by far the most robust of all techniques listed, Differential TOF and Background Canceling TOF in particular are likely to be useful for a few select use cases. The largest challenge associated with these techniques is the dependency on the hidden parameters that characterize the object parameter model. We will revisit this aspect in Chapter 5.

Of course, each of these techniques also introduce another performance constraint regarding computational cost. While differential TOF can be estimated with a simple ratio, all other techniques require some sort of polynomial root solver in order to compute the effective distance, which can be potentially limiting in it's application.

Some of this can be mitigated by precomputing the roots based off the known parameters, and only keeping a lookup table or polynomial approximation on the local system. This, as well as much of the implementation level concerns such as the effect of circuit non-idealities, are subjects of future research.

Table 4.1: Summary of Real Time Techniques for extracting Effective Distance

Technique	Components and Parameters	Immunity		
	Pulsed TOF / SWM TOF	CT	BG	Both
Conventional TOF	$f(W_1, W_2)$ $f(x_I, x_Q)$	No	No	No
Intensity	$f(W_2, c_0, c_1, c_2)$ $f(\|x\|, c_0, c_1, c_2)$	No	No	No
Differential TOF	$f(\frac{\partial W_1}{\partial t}, \frac{\partial W_2}{\partial t}, c_0, c_1)$ $f(\frac{\partial x_I}{\partial t}, \frac{\partial x_Q}{\partial t}, c_0, c_1)$	Yes	No	No
BC TOF	$f(W_1, W_2, c_0, c_1, c_2, R)$ $f(x_I, x_Q, c_0, c_1, c_2, R)$	No	Yes	No
Background Intensity	$f(W_1, W_2, c_0', c_1', \Phi_{BG}, R)$ $f(x_I, x_Q, c_0', c_1', \Phi_{BG}, R)$	No	Yes	No
BC D-TOF	$f(\frac{\partial W_1}{\partial t}, \frac{\partial W_2}{\partial t}, c_0, c_1, c_2, c_0', c_1', \Phi_{BG}, R)$ $f(\frac{\partial x_I}{\partial t}, \frac{\partial x_Q}{\partial t}, c_0, c_1, c_2, c_0', c_1', \Phi_{BG}, R)$	Yes	Yes	Yes

Chapter 5

Algorithmic Parameter Extraction

In the previous chapter, we developed several techniques for extracting object properties based off the current reading and it's derivatives. We will extend this to multiple measurements, where we are no longer solely rely on arithmetic identities. Once again, we will take advantage of redundancy, but this time in the parameters that are kept constant with the use of least square estimation and optimization algorithms.

5.1 Introduction to Least Square Estimation and Numerical Optimization

Least Square Estimation is the technique of estimating a finite number of parameters from an overdetermined system, or a system with more equations than unknowns. Least square estimation and more generally, numerical optimization, is invaluable for fitting data to a model. These techniques take advantage of redundancy in the data to solve for parameters in the presence of noise. For linear systems, this technique results in a closed form solution, and is easily solved using linear algebra. Non-linear systems do not have closed form solutions, but can typically be solved numerically using iterative methods. Linear least square techniques do not require any initial guesses, are not guaranteed to converge on the minimum least square error due to local minima.

We will use these techniques to estimate the effective distance and object parameters from a series of intensity and time-of-flight measurements. It is important to note here that in order for most of these techniques to work, the number of observations must be greater than the number of parameters. Although fitting a model with more parameter than observations is not impossible, it typically relies on the data being sparse and compressible. Thus, we will limit the scope of models to those that have less parameters than observations.

Specifically, each instance allows two measurements: the time of flight and the intensity. Equivalently, we can use the two components used for acquiring the time of flight measurement, W_1 and W_2 for Pulsed TOF, or x_I and x_Q for SWM TOF. If we model a series of N measurements using less than N parameters, least squares techniques can be used.

It is important to note that this chapter does not seek to find the best algorithm nor attempts to achieve unbiased results, but rather seeks to show implementations of simple algorithms that illustrate the potential for using optimization techniques in the implementation of hybrid intensity/TOF systems.

5.2 Estimations Techniques for Object Property Extraction

Once again, we will come up with several use cases, and examine techniques that can be used to extract parameters. The basic advantage from using multiple samples stems from the fact that while we expect the effective distance r_e to change, we are assuming the object parameters c_0, c_1, and c_2 to be fixed. This creates redundancy in the data, and allows us to extract parameters with less information that we would have needed otherwise.

5.2.1 Single Moving Object

Simarly to the previous section, we will begin by examining the case of a single object in the field of view of the sensor. As we established last time, the effective distance r_e can be obtained trivially:

$$
\begin{aligned}
r_e &= r_0 \frac{W_1}{W_2} && \text{for Pulsed TOF} \qquad (5.1)\\
r_e &= \frac{1}{k} \tan^{-1}\left(\frac{x_Q}{x_I}\right) && \text{for SWM TOF} \qquad (5.2)
\end{aligned}
$$

We also know the intensity of the signal $\Phi = \Phi_{obj}$:

$$
\begin{aligned}
\Phi &= \frac{W_2}{T_p} && \text{for Pulsed TOF} \qquad (5.3)\\
\Phi &= \sqrt{x_I^2 + x_Q^2} && \text{for SWM TOF} \qquad (5.4)
\end{aligned}
$$

We also know that $\Phi = \Phi_{obj}$ can be modeled using our object parameter model:

$$\Phi = \Phi_{obj} = \Phi_0 A_D \frac{c_0 c_2}{r_e^2 (r_e^2 + c_1 r_e + c_0)} \qquad (5.5)$$

We will now seek to solve for c_0, c_1, and c_2 using least square estimation. The fundamental assumption we make here is that the parameters c_0, c_1, and c_2 remain constant while the effective distance r_e varies. This problem can be reduced to a linear system, using the following transformation:

$$\begin{aligned} x_1 &= \frac{1}{c_2} \\ x_2 &= \frac{c_1}{c_0 c_2} \\ x_3 &= \frac{1}{c_0 c_2} \\ b_i &= 1/\Phi_{obj-i} \\ A_{i,j} &= r_{e-i}^{j+1} \text{ for } j = 1, 2, 3 \end{aligned} \tag{5.6}$$

$$A = \begin{pmatrix} r_{e-1}^2 & r_{e-1}^3 & r_{e-1}^4 \\ r_{e-2}^2 & r_{e-2}^3 & r_{e-2}^4 \\ r_{e-3}^2 & r_{e-3}^3 & r_{e-3}^4 \\ \vdots & \vdots & \vdots \\ r_{e-N}^2 & r_{e-N}^3 & r_{e-N}^4 \end{pmatrix} \qquad x = \begin{pmatrix} \frac{1}{c_2} \\ \frac{c_1}{c_0 c_2} \\ \frac{1}{c_0 c_2} \end{pmatrix} \qquad b = \begin{pmatrix} \frac{1}{\Phi_{obj-1}} \\ \frac{1}{\Phi_{obj-2}} \\ \frac{1}{\Phi_{obj-3}} \\ \vdots \\ \frac{1}{\Phi_{obj-N}} \end{pmatrix}$$

We are interested in solving for x such that $Ax = b$, which is generally an over constrained system, and generally is not solvable in the presence of noise such as this case. Instead, we will find the value $\hat{x} = \frac{A^T b}{A^T A}$, which is the least square error estimate of x [9]. Solving this minimizes the total error in $\frac{1}{\Phi_{obj}}$ for each of the sample data. If we wish to minimize the percent error, we need to normalize the weighting such that each row of contributes equally. This can be achieved by multiplying both sides of the equation with the diagonal matrix $C_{i,j} = \frac{1}{b_i}$

$$C = \begin{pmatrix} \frac{1}{b_1} & & & & \\ & \frac{1}{b_2} & & & \\ & & \ddots & & \\ & & & \frac{1}{b_{N-1}} & \\ & & & & \frac{1}{b_N} \end{pmatrix}$$

The new equation we now wish to solve becomes $A'x' = b'$, where

$$\begin{aligned} A' &= CA \\ b' &= Cb \end{aligned}$$

solved by the estimator given by:

$$\begin{aligned} \hat{x'} &= \frac{A'^T b'}{A'^T A'} \\ &= \frac{(CA)^T b}{(CA)^T (CA)} \\ &= \frac{A^T C^T b}{A^T C^T C A} \end{aligned} \tag{5.7}$$

The parameters c_0,c_1,and c_2 can be derived from these results using these relationships:

$$\begin{aligned} c_0 &= \frac{x_0}{x_2} \\ c_2 &= \frac{1}{x_0} \\ c_1 &= \frac{x_1}{x_2} \end{aligned} \tag{5.8}$$

This technique is possible for a minimum of three samples, which is when A is a square matrix, making A invertible and $x = \hat{x}$. For greater number of measurements, redundancy in the data allows us to reduce the effects of noise and measurement error. However, it should be noted that because of the nature of the parameters being solved for, this technique does not produce accurate values of c_0 unless a sample is taken from the region where the model displays forth law behavior, and similarly does not produce accurate values of c_1 unless third law behavior or the transition point between square and forth law behaviors is recorded.

The main limitation of this technique is that it is only accurate if the object parameters are constant, or equivalently, the motion is purely radial. Simultaneous rotation and translation, or other complex motions will likely result in erroneous results. However, this technique is relatively robust, as can be seen in Figures 3-7 and 3-10 show the technique estimating a set of parameters that be closely approximate a similar object undergoing linear on-axis motion.

5.2.2 Single Object with Unknown Crosstalk or Second Stationary Object

We will now consider the problem of removing an unknown offset from our signal. In Chapter 4, we solved this problem by using computing the TOF from differential components, and making assumptions of the time of flight v.s. effective distance relationships. Here we will do similar, but with optimization algorithms using many samples.

In this problem, the number of known parameters are much greater than that for a single object, because effective distance of the target object is not trivially extractable like it was for the single object scenario.

As discussed in Chapter 3, in the presence of crosstalk, the measured components are composed of composed of the signal components as well as some unknown crosstalk. For Pulsed TOF, this relation is summarized by:

$$\begin{aligned} W_1' &= W_1 + CT_1 \\ &= \frac{c_0 c_2}{r_e^2(r_e^2 + c_1 r_e + c_0)} \frac{r_e}{r_0} T_p + CT_1 \qquad (5.9) \\ W_2' &= W_2 + CT_2 \\ &= \frac{c_0 c_2}{r_e^2(r_e^2 + c_1 r_e + c_0)} T_p + CT_2 \qquad (5.10) \end{aligned}$$

For SWM TOF,

$$\begin{aligned} x'_I &= x_I + CT_I \\ &= \frac{c_0 c_2}{r_e^2(r_e^2 + c_1 r_e + c_0)} \cos(kr_e + \phi_0) + CT_I \end{aligned} \tag{5.11}$$

$$\begin{aligned} x'_Q &= x_Q + CT_Q \\ &= \frac{c_0 c_2}{r_e^2(r_e^2 + c_1 r_e + c_0)} \sin(kr_e + \phi_0) + CT_Q \end{aligned} \tag{5.12}$$

where k and ϕ_0 are known constants, although the technique can still be applied if they are unknown by considering them as parameters.

We know have up fixed parameters (CT_I, CT_Q), and up to four parameters (r_e, c_0, c_1,c_2) per sample, but with only two observable quantities per sample (x_I,x_Q). To limit the complexity of the problem, we will once again assume constant object parameters c_0, c_1 and c_2. This would limit the problem to five fixed parameters and one parameter per sample. This is less parameters than observable quantities if more than three samples (or equivalently, six observations) are collected.

However, unlike the Single Object case, we are unable to transform the system into a linear system. Thus, non-linear techniques must be used. A straight forward but inefficient method of solving for the unknown parameters would be to simply set up an optimization algorithm with all of the unknowns, including the effective distance for each reading, set as parameters. This results in an optimization algorithm with $N + 5$ parameters for for series of N measurements.

Although this technique could theoretically work, the objective function must be very carefully chosen, and the initial guess of the parameters must be fairly close for the method to converge. Furthermore, computation time becomes rather large for data sets of modest size, due to the high dimensionality of the problem. This motivates us to find more efficient algorithms to solve for the parameters.

One particularly effective method is a direct extension of the DTOF method introduced in Section 4.3.2.2. In this section, we introduced a method of solving for the effective distance given a set of DTOF measurements and the object parameters c_0 and c_1. Conceptually, we can iteratively pick a value of c_0 and c_1, solve for the distance using the DTOF method, compare the results for a good fit, and adjust c_0 and c_1 accordingly.

The most straightforward method of doing this is to use another linear least square estimator to evaluate the fit. Given a particular choice of estimates for c_0 and c_1, we can represent Equation 5.9 as a series of 2N equations with three unknowns(c_2, CT_1, CT_2). We will solve this once again with a linear least square estimator as follows:

$$A = \begin{pmatrix} 1 & 0 & \frac{1}{c_2}\hat{W}_{1-1} \\ 0 & 1 & \frac{1}{c_2}\hat{W}_{2-1} \\ 1 & 0 & \frac{1}{c_2}\hat{W}_{1-2} \\ 0 & 1 & \frac{1}{c_2}\hat{W}_{2-2} \\ \vdots & \vdots & \vdots \\ 1 & 0 & \frac{1}{c_2}\hat{W}_{1-N} \\ 0 & 1 & \frac{1}{c_2}\hat{W}_{2-N} \end{pmatrix} \qquad x = \begin{pmatrix} CT_1 \\ CT_2 \\ c_2 \end{pmatrix} \qquad b = \begin{pmatrix} W'_{1-1} \\ W'_{2-1} \\ W'_{1-2} \\ W'_{2-2} \\ \vdots \\ W'_{1-N} \\ W'_{2-N} \end{pmatrix}$$

where:

$$\begin{aligned} \frac{1}{c_2}\hat{W}_{1-i} &= \frac{c_0}{r_{e-i}^2(r_{e-i}^2 + c_1 r_{e-i} + c_0)} \frac{r_{e-i}}{r_0} \\ \frac{1}{c_2}\hat{W}_{2-i} &= \frac{c_0}{r_{e-i}^2(r_{e-i}^2 + c_1 r_{e-i} + c_0)} \end{aligned} \tag{5.13}$$

We will once again minimize the normalized error, obtained by Equation 5.7. The accuracy of this best fit relies on correctly chosen values for c_0 and c_1. Therefore, error of the least square estimator $||b' - A'\hat{x}||^2$ is minimized when $c_0 = \hat{c_0}$ and $c_1 = \hat{c_1}$. We will use this fact to run a second optimization algorithm to minimize the best case error in the linear least square estimator. The result of this nested optimization is a complete set of optimized parameters, c_0, c_1, c_2, CT_1, and CT_2. The effective distance is computed with the DTOF technique using the final optimized parameters.

The choice of optimization algorithm is not important, but for the purpose of demonstration, SLSQP Optimization in the scipy.optimize library for Python was used to verify this algorithm. Figures 5-1 and 5-2 show the results for fitting a model with parameters $c_0 = 0.1$, $c_1 = 10$, $c_2 = 0.1$, and $CT_1 = CT_2 = \Phi_0 \frac{A_D}{1m^2} T_p$. For a data set of 40 points, solution were obtained in around 30 iterations. Convergence was confirmed for as few as 6 data points, or 12 observations.

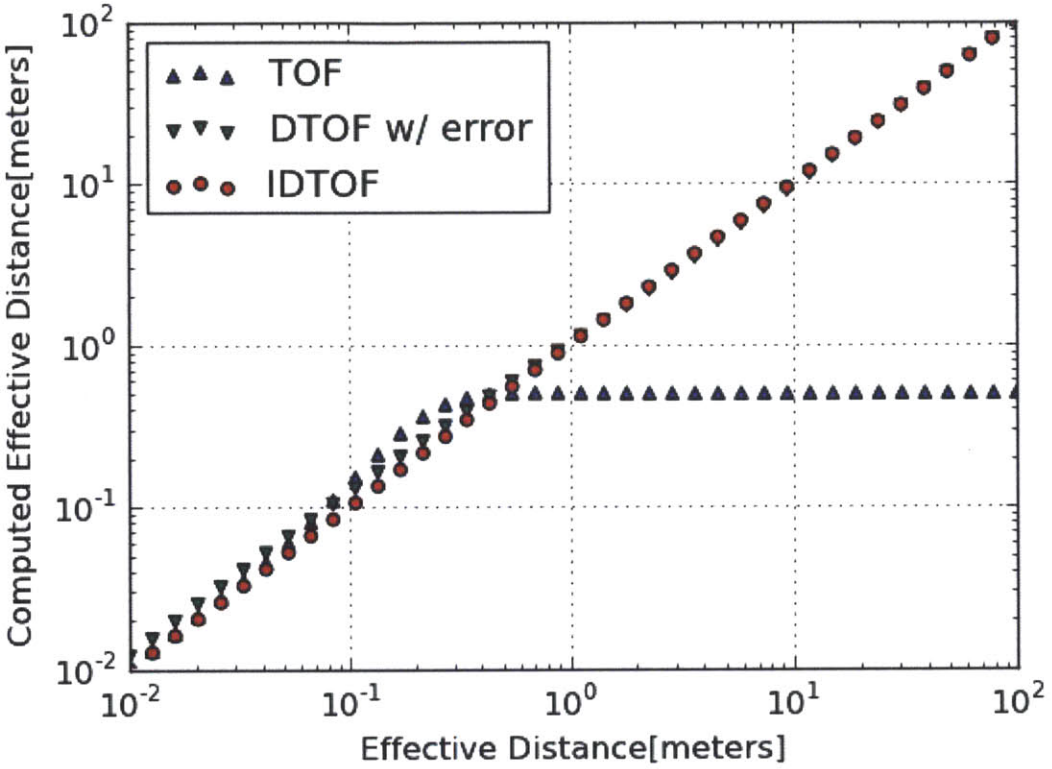

Figure 5-1: Effective Distance Computed using Iterative DTOF

5.2.3 Single Object with Uniform Background

We will now consider the case of a uniform background. In Chapter 4, we developed a method of extracting distance given information of the distance of the background R, and the object parameters c_0, c_1, and c_2. Here, we will consider scenarios and techniques where we can estimate the effective distance with less information.

From Section 3.3, we have:

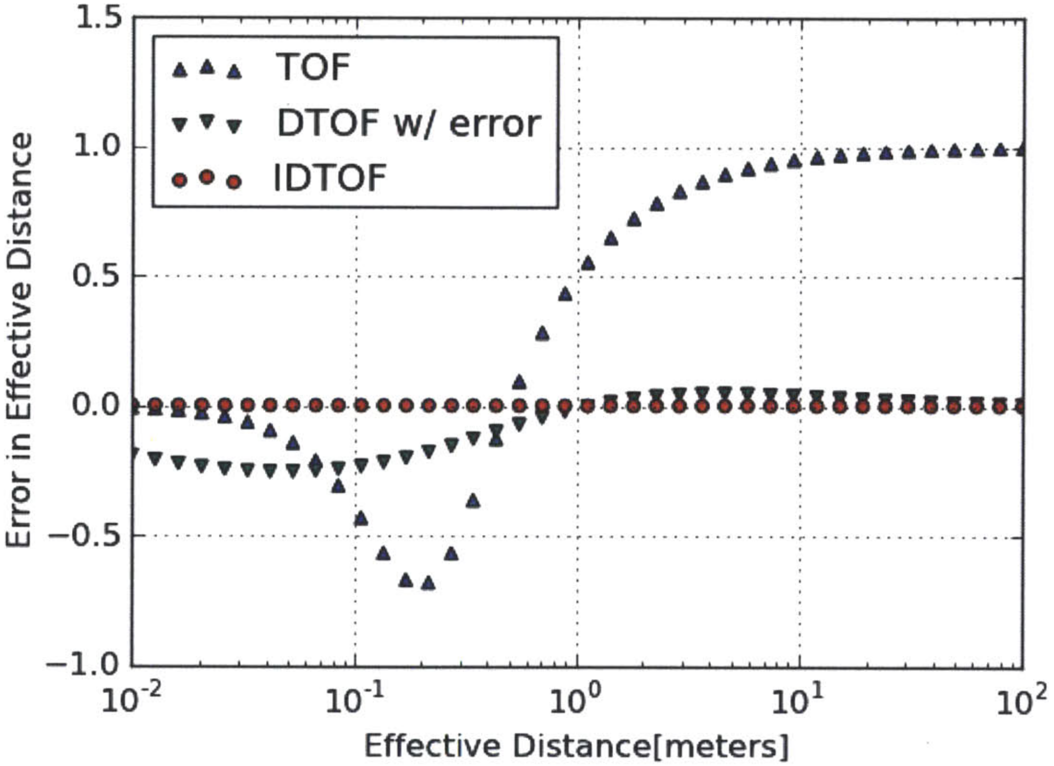

Figure 5-2: Normalized Error using Iterative DTOF

$$
\begin{aligned}
W_1' &= W_1 + BG_1 \\
&= \Phi_{obj}(r_e, c_0, c_1, c_2) T_p \frac{r_e}{r_0} + \Phi_{bg}(r_e, \Phi_{BG}, c_0', c_1') T_p \frac{R}{r_0} \\
&= \Phi_0 A_D \frac{c_0 c_2}{r_e^2(r_e^2 + c_1 r_e + c_0)} \frac{r_e}{r_0} T_p + \Phi_{BG} \frac{r_e^2 + c_1' r_e}{r_e^2 + c_1' r_e + c_0'} T_p \frac{R}{r_0} \qquad (5.14)\\
W_2' &= W_2 + BG_2 \\
&= \Phi_{obj}(r_e, c_0, c_1, c_2) T_p + \Phi_{bg}(r_e, \Phi_{BG}, c_0', c_1') T_p \\
&= \Phi_0 A_D \frac{c_0 c_2}{r_e^2(r_e^2 + c_1 r_e + c_0)} T_p + \Phi_{BG} \frac{r_e^2 + c_1' r_e}{r_e^2 + c_1' r_e + c_0'} T_p \qquad (5.15)
\end{aligned}
$$

In Chapter 4. we observed that the entire background term $\Phi_{bg}(r_e, \Phi_{BG} c_0', c_1')$ can be eliminated from the expression given the background distance R, resulting in an a polynomial expression that resulted in the solution $r_e = f(W_1', W_2', c_0, c_1, c_2, R)$. We also saw that the object parameter model term $\Phi_{obj}(r_e, c_0, c_1, c_2)$ could be eliminated from the equation in a similar process, giving a solution of the form $r_e = f(W_1', W_2', c_0', c_1', \Phi_{BG}, R)$. Here, we will attempt to estimate the missing parameters and reduce the number of input arguments required by taking advantage of muiltiple samples.

5.2.3.1 Known Distance, Unknown Object Parameters, $c_0' = c_0$, $c_1' = c_1$.

Let us recall the behavior of the background term Φ_{bg}:

$$
\Phi_{bg} = \Phi_{BG} \frac{r_e^2 + c_1' r_e}{r_e^2 + c_1' r_e + c_0'} \qquad (5.16)
$$

Although in general the shadow's parameters c_0' and c_1' are not known, there exists a special case where $c_0' = c_0$ and $c_1' = c_1$. Physically, this happens when the surface properties of the background and the object are identical. For all practical purposes, this only occurs when both the background and the target object are perfectly diffuse objects. The relative reflectivity may differ between the two, but the angular redistribution as a result of the reflection off of the surface must behave similarly.

In this special case, we can set up the following matrix:

$$A = \begin{pmatrix} \frac{r_{e-1}^2+c_1 r_{e-1}}{r_{e-1}^2+c_1 r_{e-1}+c_0} \\ \frac{r_{e-1}^2+c_1 r_{e-1}}{r_{e-1}^2+c_1 r_{e-1}+c_0} \frac{R}{r_0} \\ \frac{r_{e-2}^2+c_1 r_{e-2}}{r_{e-2}^2+c_1 r_{e-1}+c_0} \\ \frac{r_{e-2}^2+c_1 r_{e-2}}{r_{e-2}^2+c_1 r_{e-1}+c_0} \frac{R}{r_0} \\ \vdots \\ \frac{r_{e-N}^2+c_1 r_{e-N}}{r_{e-N}^2+c_1 r_{e-N}+c_0} \\ \frac{r_{e-N}^2+c_1 r_{e-N}}{r_{e-N}^2+c_1 r_{e-N}+c_0} \frac{R}{r_0} \end{pmatrix} \qquad x = \Phi_{BG} \qquad b = \begin{pmatrix} W'_{1-1} - \hat{W}_{1-1} \\ W'_{2-1} - \hat{W}_{2-1} \\ W'_{1-2} - \hat{W}_{1-2} \\ W'_{2-2} - \hat{W}_{2-2} \\ \vdots \\ W'_{1-N} - \hat{W}_{1-N} \\ W'_{2-N} - \hat{W}_{2-N} \end{pmatrix}$$

Finding the least square estimate of $x = \Phi_{BG}$, obtained through the $\hat{x} = \frac{A^T b}{A^T A}$ will give us the only remaining unknown parameter. The resultant error can be further minimized algorithmically by iteratively executing this process for various values of c_0, c_1, and c_2.

A successful minimization of this problem results in a solution where the effective distance is obtained only from the time-of-flight measurements W'_1, W'_2 and the background distance R, i.e. $r_e = f(W'_1, W'_2, R)$. However, simple simulations using the numerical simulation model developed based on the results of Chapter 2 show that although c_0 and c'_0 tend to scale together, they can be up to an order of magnitude different from differences in surface properties and orientation. Under these variations, this technique still successfully converges, but can easily be 20% 50% off.

5.2.3.2 $c_0 \neq c'_0, c_1 \neq c'_1$, Known Background

If we let the shadow parameters c'_0 and c'_1 take any value, this problem increases it's complexity drastically. Even if the completely characterized background, where the both parameters Φ_{BG} and R are known, no stable algorithm was found.

In principle it is possible to iteratively solve for the unknown parameters. One method that was tried using idealized signals was to use a linear least square estimator on the results of the Background Intensity Method from section 4.3.3.2. Because this model fully predicts the behavior of the background signal, we can simply subtract it from the measured signal, giving us an estimate of the signal contributions from the object. We can then use the technique from section 5.2.1 to estimate the object parameters c_0, c_1, c_2. This technique is especially worthy of note in that it provides a way to systematically identify the most plausible solution for r_e when multiple real positive roots exist to the polynomial. The error associated in this least square estimation can conceivably be further minimized by iteratively applying the Background Intensity method with various values of c_0', c_1', but this algorithm was found to be generally unstable.

The symmetric technique would be to use Background Canceling TOF (BC TOF) and estimate c_0', c_1'. Although this technique successfully differentiated between the roots provided by BC TOF that adhered to the expected background behavior, further minimization of the error using optimization algorithms were unsuccessful, due to similar convergence issues.

Both of these algorithms, as well as the brute force method of applying an optimization algorithm on all of the 5 unknown parameters $(c_0, c_1, c_2, c_0\prime, c_1')$ successfully converged when all of the ideal parameters were set as the initial estimate, but had trouble converging when any of the parameters were more $1\% \sim 10\%$ off, depending on the algorithm.

5.2.3.3 Unknown Background

Although it would be useful to extract distance without prior knowledge of the background distance, this is not possible. This can be shown by attempting elimination of the background distance R from or simultaneous equations.

$$W_1' = W_1 + \Phi_{BG} T_p \frac{R}{r_0}$$

$$W_2' = W_2 + \Phi_{bg} T_p$$

Because there is only one term in one equation that involves R, it is impossible to eliminate R from your series of equations. This means that any equation we form in order to solve for effective distance r_e will always result in a function depending on R. This indicates that it becomes impossible to distinguish between an infinite set of signals caused by a different background/signal combinations. This makes this problem impossible, regardless of choice of algorithm.

5.3 Summary of Algorithmic Techniques

Table 5.3 summarizes the successful algorithms discussed in this chapter. Linear least square estimation proved invaluable for estimating the values of the hidden parameters when effective distance over a set of data is known. Furthermore, it provides a method for systematically identifying the correct root to the solutions to the polynomials that result from the techniques in Chapter 4.

Iteratively using one of the real time techniques from Chapter 4, and applying least square estimation to check the compliance with modeled behavior provides a natural way to optimize the choice of hidden parameters with out prior knowledge. Especially for Differential TOF, an iterative approach showed excellent convergence properties, and worked for a wide range of inputs and initial vectors. This implies that if the differential components of a Hybrid Intensity/Time-Of-Flight system can be measured with sufficient accuracy, a system that responds to the distance of any moving object can be made, regardless of crosstalk. However, this technique and all others discussed in this chapter rely on the parameters remaining constant through out the motion, limiting the application space of the technique.

Iteratively tuning techniques that involve backgrounds proved difficult at best. For the special case where $c_0 = c_0'$, and $c_1 = c_1'$, a stable algorithm was found, but convergence was an issue all other cases. Furthermore, dependance on the background distance is inherent for all of the proposed algorithms, severely limiting the use cases of such algorithm.

The use of linear least square estimators requires doing algebraic computation with large matrices. Although this is a simple task for a full processor equipped with

MATLAB, Python, or similar, this is a daunting task for any System-On-Chip(SOC), and would likely require a dedicated digital signal processor. The iterative techniques such as Iterative D-TOF and Iterative BC TOF required computations on the order of 3 $\sim$ 30 seconds on a 2.4GHz Intel Quad-Core i7. Due to their iterative nature, these algorithms require solving up to hundreds of polynomial roots and linear least squares, and likely require computational resources that are impractical to be implanted by any SOC, any would require intense resources from the host system. For this reason, it is likely that these techniques are best used sparingly, if at all.

Table 5.1: Summary of Real Time Techniques for extracting Effective Distance

Technique	Components and Parameters	Immunity		
	Pulsed TOF / SWM TOF	CT	BG	Both
LLS Estimation	$\{c_0, c_1, c_2\} = f(W_1, W_2, r_e)$ $\{c_0, c_1, c_2\} = f(x_I, x_Q, r_e)$	No	No	No
	$\{c_2, CT_1, CT_2\} = f(W_1, W_2, r_e, c_0, c_1)$ $\{c_2, CT_I, CT_Q\} = f(x_I, x_Q, r_e, c_0, c_1)$	Yes	No	No
	$\{c_0, c_1, c_2\} = f(W_1, W_2, r_e, c'_0, c'_1, \Phi_{BG}, R)$ $\{c_0, c_1, c_2\} = f(x_I, x_Q, r_e, c'_0, c'_1, \Phi_{BG}, R)$	No	Yes	No
	$\{c'_0, c'_1\} = f(W_1, W_2, r_e, c_0, c_1, c_2, \Phi_{BG}, R)$ $\{c'_0, c'_1\} = f(x_I, x_Q, r_e, c_0, c_1, c_2, \Phi_{BG}, R)$	No	Yes	No
Iterative D-TOF	$\{r_e, c_0, c_1, c_2, CT_1, CT_2\} = f\left(\frac{\partial W_1}{\partial t}, \frac{\partial W_2}{\partial t}\right)$ $\{r_e, c_0, c_1, c_2, CT_I, CT_Q\} = f\left(\frac{\partial x_I}{\partial t}, \frac{\partial x_Q}{\partial t}\right)$	Yes	No	No
Iterative BC TOF	$\{r_e, c_0 = c'_0, c_1 = c'_1, c_2\} = f(W_1, W_2, \Phi_{BG}, R)$ $\{r_e, c_0 = c'_0, c_1 = c'_1, c_2\} = f(x_I, x_Q, \Phi_{BG}, R)$	No	Yes	No

Chapter 6

Conclusion

This thesis has explored several classes of techniques made possible by combining intensity and time-of-flight information for an active IR distance sensor. Starting from modeling the reflections from an arbitrary scene as developed in Chapter 2, a model that characterizes signals contributed from objects, crosstalk, and backgrounds was developed and verified using analytical examples and numerical simulations. These models were then used to develop techniques for mitigating the effects of crosstalk and backscatter, in Chapters 4 and 5. The results show that using both time-of-flight and intensity information, one can extract distance even when subject to crosstalk or backscatter, with some limited knowledge about the scene.

6.1 Summary of Hybrid Intensity/Time-Of-Flight Techniques

Table 6.1 summarizes the plain language descriptions of the computational cost and information required for of the major techniques discussed in this work.

6.1.1 Capabilities

There are three main capabilities that hybrid intensity/time-of-flight techniques provide.

Table 6.1: Summary of Hybrid Intensity/Time-Of-Flight Techniques

Technique	Information Required	Comp. Cost
Conventional TOF	TOF	Low
Intensity	Intensity, Object Properties	Moderate
Differential TOF	Intensity, TOF, Object Properties	Low/Moderate
Iterative D-TOF	Intensity, TOF	High
BC TOF	Intensity, TOF, Background, Object	Moderate
Background Intensity	Intensity, TOF, Background, Object	Moderate
Iterative BC-TOF	Intensity, TOF, Background	High

Immunity to unknown crosstalk Use of Differential TOF and Iterative D-TOF grants immunity to crosstalk.

Performance under known background. Use of Background Intensity Method or Iterative BC TOF allows effective distance to be extracted in the presence of a background as long as the background signal can be measured and quantified.

Ability to extract properties of the target object. Use of least square approximations allow the estimation of object parameters that are indicative of the size, shape, and reflectivity of the object.

6.1.2 Requirements and Limitations

The underlying requirement for almost all of the techniques developed in this work require the target object to under go radial motion. Redundancy accumulated from multiple readings and/or derivative information is the fundamental basis of the techniques, and radial motion ensures that appropriate redundant information is generated and acquired. Non radial motion and other irregularities will introduce an error for most hybrid techniques.

In addition, all techniques require an approximate knowledge of some properties of the target object and/or background. Iterative techniques will use these estimates as an initial vector for an optimization algorithm, ideally converging on the optimal approximation. Non-iterative techniques will use these parameters in their polynomial expressions, and any inaccuracies in these parameters will contribute an error to the results.

Computational costs of hybrid techniques are typically much greater than that of a conventional system. A conventional Pulsed TOF system only requires one division operation. For SWM TOF, the CORDIC algorithm and similar approaches allow conversion with relatively low computational cost. The techniques classified introduced in Chapter 4 all generally require a polynomial root solver, or at least a lookup table with it's contents pre-computed. However, for the techniques that involve a background component, the tables would need to be a two variable look up table, making the storage and computational costs quite large even as a lookup table. As for the techniques introduced in Chapter 5, these require linear algebra and may require up to hundreds of least square estimators and polynomials to be solved, making the computational costs unsuitable for most applications.

The precision requirements for signals are also of concern for these techniques. In particular when the signal strength contributed from the target object is small compared to crosstalk or background, the system is likely to suffer from Signal-to-Noise-Ratio issues. Thus higher performance front end circuitry will be likely required.

6.1.3 Applications

Applications for these techniques are not entirely obvious, as the requirements and limitations are potentially restrictive. The high computational cost causes these techniques to loses some of the advantages that a a spatially averaged sensor has. However, it is likely that using a combination of techniques including conventional TOF, real time techniques and algorithmic techniques will provide a good compromise between performance and power. For example, using computationally costly algorithmic techniques in a calibration phase, and relying only on real time or conventional techniques for real time measurements can reduce power requirements where it is important. Alternatively, real time techniques can be used to acquire a "first pass" measurement that is used to trigger an event to "wake up" the host when appropriate, and the host can use algorithmic techniques to verify the event. Combining techniques of various computational requirements can potentially create efficient solutions to traditionally difficult problems.

6.2 Future Work

6.2.1 Implementation Level Concerns

This work focused on identifying plausible techniques and ignored sources of error and noise for the majority of the analysis. For implementing in a real life system, these non-idealities may become important. Particularly interesting are the effects of drift in time delay/phase of the front circuitry, as well as the overall gain of the system. Another important concern is how noise effects the hybrid techniques, in particular the least square estimators. Optimal least square estimators depend on the shape of the error distribution, and the techniques will likely need to be modified according to the actual distribution of noise and error. Convergence issues associated with noise and error for the optimization algorithms is also important for a real system, and one that is ill understood.

6.2.2 Taking Advantage of Time Domain Information

One potential venue to take the results of this work further is to introduce the significance of the time domain in the base band. Real time techniques are only concerned with instantaneous measurements, and treated each sample as a separate problem. Algorithmic techniques took multiple readings, but treated it as unsorted data. However, we know that physical objects can only move at finite speeds, and that motion is more likely to have smooth transitions. One approach would be to take the frequency domain transform (z-transform, Laplace transform) of the effective distance, and assume that the frequency content of the motion is band limited. This could even by applied to multiple parameters, allowing potentially all of the parameters (i.e. r_e, c_0,c_1,c_2, etc.) to change over time, but with low frequency content. This would reduce the number of variables in the system, and potentially give rise to techniques that can estimate distance and object properties for a wider range of physical scenarios, potentially accounting for non-radial motion and objects that dynamically change in reflectivity or size.

6.3 Concluding Remarks

This work pioneered a completely new class of distance sensing technology which combines the information from an intensity based and time-of-flight sensor. While implementation details and specific applications are still up for discussion, a clear scope of capabilities were analyzed and discussed. Although the technology has very specific limitations, in the right application, hybrid intensity/time-of-flight sensors have the strong potential to provide unique performance traits in otherwise difficult environments.

Appendix A

Internal Conference Paper

The following paper was written by Dave Ritter and the author of this work, and submitted to an internal company conference called the Intersil Engineering Conference (IEC). Titled *Vector Domain Differentiation: IR Motion Detection in High Backscatter Environments*, this paper discusses a first pass at some of the techniques discussed in this work.

Vector Domain Differentiation: IR Motion Detection in High Backscatter Environments

David W. Ritter
Sr Principal Engineer
Intersil Corporation
Milpitas, CA
David.Ritter@intersil.com

Itaru L. Hiromi
Former Intern & Student
MIT
Cambridge, MA
ihiromi@MIT.EDU

Abstract— ***This paper describes a signal processing scheme, called Vector Domain Differentiation (VDD), for active IR distance sensing of moving objects in the presence of significant environmental backscatter. In particular VDD applies to a coherent (sinusoidally modulated) time of flight system comprising a modulated LED and PIN diode detector. VDD is based on a critical and generally non-intuitive result: there is a simple relationship between the first derivative of the received signal in the IQ domain and the desired distance result. This will be shown theoretically in the paper and simulation results presented.***

I. INTRODUCTION

A category of monolithic devices is emerging that allows electronic products to sense their environment [1][2]. These include such diverse devices as accelerometers, monolithic gyroscopes, light sensors and imagers. In particular multiple market segments have increasing interest in proximity sensing: detecting the presence and/or distance of a user to the product for the purpose of controlling power, displays, or other interface options. Intersil is a leader in the ALS (Ambient Light Sensor) and Active IR Proximity devices. ALS's are used in portable equipment to modulate the backlight levels of displays to conserve battery power. Proximity detectors are used in cell phones (for example) to disable displays when the unit is held to the ear during phone calls (further conserving battery power). Intersil's current state of the art in integrated proximity sensors is limited to <50 cm [3]. The following discussion and derivation is part of an advanced active IR proximity sensor project, the ISL29200, intended to extend the range of the product line to 2 meters using Time of Flight (TOF) techniques.

Many schemes exist for 3D imaging or distance sensing using time of flight (TOF) techniques [4]. These methods either directly measure the delay of a pulse from a laser or LED, or measure the phase delay of a modulated IR source. In both cases the delay is proportional to distance and independent of reflectivity of the object of interest. These techniques perform well in a controlled optical environment, and many systems use a lens to focus the field of view onto an image plane. However, in a simple proximity detector there is only a single sensor with no focusing optics. It receives a signal that is the aggregate of all reflections from all objects in the field of view. There is no image, and there is no array of sensors: there is a single, fuzzy pixel. None the less it is desirable to respond to moving objects and determine their distance while ignoring the static objects in the field (and other static contributors such as electrical crosstalk). Vector Domain Differentiation (VDD) will be shown to achieve these goals with simple signal processing in a practical system.

II. ACTIVE IR PROXIMITY DETECTION SYSTEM

Active IR proximity detectors can be implemented using IR LED emitters and PIN diode detectors. The ISL29200 uses a high frequency (5 MHz) modulated LED and a tuned PIN receiver to detect the presence of objects in the field of view and determine their distance. Figure 1 shows a simplified diagram of the system. Details of much of the signal processing are included in another paper at this conference [5], but for present purposes it is only necessary to note that the ISL29200 observes the field of view through a single sinusoid received at the PIN diode. The only information available about the field of view is encoded in the amplitude and phase of this signal and its evolution in time.

ISL29200 Block Diagram

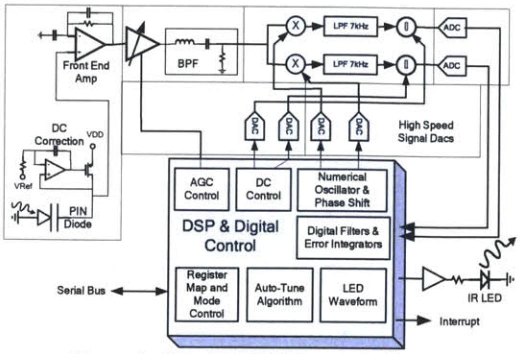

Figure 1 – The ISL29200 Proximity Sensor

Figure 2 shows the components of received signal at any time: a) electrical crosstalk, b) optical crosstalk due to the glass covering, c) static backscatter, and d) the object of interest.

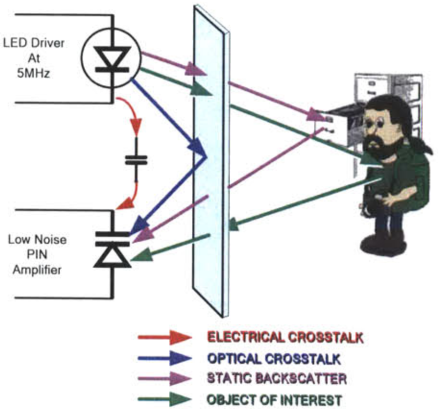

Figure 2 - Received Signal Elements in Active IR Proximity Detector

One goal of the ISL29200 is to determine the distance to the object of interest while compensating for the above interferers. Both electrical and optical crosstalk can be approximated to be relatively constant through the life time of the device, and may be calibrated at the manufacturing or development stage of the application. Environmental backscatter poses a much more difficult problem. Objects such as a cabinet surface are not useful targets, but will show up as a significant component of the signal. The primary difference between a useful target (user approaching a laptop), and other objects (filing cabinets, soda cans, cubical walls) in the environment is motion: the user moves relative to the laptop while other objects are still. A traditional approach to discriminating steady, 'DC', content from changing, 'AC', content is the application of a high pass filter. While it is clear that some of the signal will pass through such a filter, it is not clear how such a filter will distort the distance information in a TOF system. What happens to the phase of a signal when the demodulated components are passed through a high pass filter?

III. THE SIGNAL MODEL

The received signal is the sinusoidal voltage and/or current (of natural frequency ω_0) induced in the PIN diode. It is proportional to the incident IR photonic signal reflected from the environment. Various parasitic capacitances and signal processing delays will cause phase and amplitude variations in the received signal, but for our purposes we will assume that these are corrected by a system calibration. Relative to the transmitted signal at the IR LED, the received signal is delayed in phase (and diminished in amplitude) and therefore has both I and Q components (In-phase and Quadrature). For mathematical convenience we will represent the I component by the real part of a complex variable x, and the Q component by the imaginary part of x. We will further consider that x is in general the sum of a constant term x_0, representing the static contributors to the signal (backscatter and crosstalk as discussed above), and a time varying signal x_s, representing a moving object (the object of interest: the laptop user). [Note: the time varying nature of x_s does not include the high speed oscillations of the modulating sinusoid, but only captures the variations in amplitude and phase of that sinusoid.]

$$x_s = x - x_0 . \tag{1}$$

According to the physics of light propagation, the phase and amplitude of x_s will vary according to the distance of the object. In addition, x_s will vary with angle to the sensor since the LED is directional. We further allow that both the distance, r, and angle of incidence to LED, α, are in general time varying, giving us:

$$x_s[r(t),\alpha(t)] = x[r(t),\alpha(t)] - x_0 . \tag{2}$$

Equation (2) is a significant assumption regarding the signal model: x_s varies with time if and only if r or α varies with time. This is equivalent to stating that the object reflectivity is constant. We will include notation showing dependence of x_s on r, α and t as necessary in the context of the development.

We can further express x_s in terms of its magnitude and phase components:

$$A_s = |x_s| = |x - x_0| , \tag{3a}$$

$$\varphi = \angle x_s = \angle(x - x_0) , \tag{3b}$$

or equivalently:

$$x_s = x - x_0 = A_s e^{j\varphi} . \tag{4}$$

Invoking the physics of light propagation once again, we can determine the specific variation of phase with distance. Given the speed of light c, and natural operating frequency ω_0, φ becomes:

$$\varphi(r) = r\frac{\omega_0}{c} = rk , \tag{5}$$

where $k = \frac{\omega_0}{c}$ *is the wave number.*

While the phase varies linearly with the distance, r, the magnitude function is more complex since it varies with both distance and angle. We begin by assuming that A_s is the product of two functions, one due to the distance from the sensor, and one due to the angle of incidence to the LED (which has a limited angle of illumination).

$$A_s(r,\alpha) = A_r(r)A_\alpha(\alpha) , \tag{6}$$

The details of an appropriate model are contained in Appendix 1 at the end of this paper. Appendix 1 is a physical model using simplifications for the LED illumination profile (raised cosine), the object of interest (an ellipse), and the reflection rule (Lambertian: simple cosine function). This physical model predicts a curve for the magnitude of x_s vs distance. The results, for reasonable sized objects (25cm to 2m) are easily fitted to the reciprocal of a fourth order polynomial in r. The LED illumination profile provides the spatial angular dependence. Both terms are included in (7).

$$A_s(r,a) = \frac{A_0}{r^2\left(r^2+ar+b\right)}\left(\tfrac{1}{2}+\tfrac{1}{2}\cos\left(\tfrac{\alpha}{\alpha_0}\pi\right)\right); \qquad (7)$$

This model is useful for creating continuous signal models for simulations, but it is difficult to work with for the analytic purposes. For those purposes, Appendix 1 shows a piecewise linear fit to the magnitude function. This version allows simple differentiation over restricted domains, but gives clear indications of behaviour from the analytic results. We repeat it here as Equations (8a) and (8b).

$$\begin{aligned}&A_s(r,a) = A_0 \bullet \\ &if(r<r_1, 1/r^2, if(r<r_2, r_1/r^3, r_1r_2/r^4)) \bullet \\ &\left(\tfrac{1}{2}+\tfrac{1}{2}\cos\left(\tfrac{\alpha}{\alpha_0}\pi\right)\right)\end{aligned} \qquad (8a)$$

Or:

$$A_s(r,a) = A_0\frac{R}{r^N}\left(\tfrac{1}{2}+\tfrac{1}{2}\cos\left(\tfrac{\alpha}{\alpha_0}\pi\right)\right) \qquad (8b)$$

giving:

$$A_r(r) = A_0\frac{R}{r^N} \qquad (9a)$$

$$A_\alpha(\alpha) = \left(\tfrac{1}{2}+\tfrac{1}{2}\cos\left(\tfrac{\alpha}{\alpha_0}\pi\right)\right) \qquad (9b)$$

where:

$R = 1$ *and* $N = 2$ *for* $r < r_1$

$R = r_1$ *and* $N = 3$ *for* $r_1 < r < r_2$;

$R = r_1 * r_2$ *and* $N = 4$ *for* $r > r_2$.

For human sized (ellipse: 1.5m x 0.5m) objects: $A_0=0.95\times10^{-9}$, $r_1=1.125$m, $r_2=2.8$m for a human sized object. The function "if(a,b,c)" in (8a) is to be understood as a conditional statement wherein "a" is a logical condition, b is the value of the function if "a" is true, and "b" is the value if "a" is false. Nesting two "if" functions provides two breakpoints in the power curve: the first at the transition from square law to cube law, and the second at the transition to fourth order law. Equation (8b) is a simpler syntax for analytic purposes. Equations (9a) and (9b) show the radial and angular components of A_s. We can now update the earlier signal definition in (4):

$$x_s(r,\alpha) = x - x_0 = A_r(r)A_\alpha(\alpha)e^{j\varphi}. \qquad (10)$$

Computing the derivatives of the magnitude components:

$$\frac{\partial A_r(r)}{\partial t} = -NA_0\frac{R}{r^{N+1}}v_r(t); \qquad (11a)$$

$$\frac{\partial A_\alpha(\alpha)}{\partial t} = -\frac{\pi}{2\alpha_0}\sin\left(\tfrac{\alpha}{\alpha_0}\pi\right)v_\alpha(t); \qquad (11b)$$

where:

$v_r(t) = \partial r/\partial t$ *is the radial velocity of the object, and*

$v_\alpha(t) = \partial\alpha/\partial t$ *is the angular velocity of the object.*

Using this magnitude model we can now write a full signal model showing both the amplitude and phase dependencies on r and α:

$$x_s(r) = x(r) - x_0 = A_0\frac{R}{r^N}\left(\tfrac{1}{2}+\tfrac{1}{2}\cos\left(\tfrac{\alpha}{\alpha_0}\pi\right)\right)e^{j\left(\frac{r}{c}\right)\omega_0}. \qquad (12)$$

IV. DIFFERENTIATION IN THE I/Q DOMAIN

We begin by considering a simple time derivative applied to the reflected signal.

A. Definition and Derivation

We begin with the time derivative of Eq(4):

$$x_s(r,\alpha) = x - x_0 = A_r(r)A_\alpha(\alpha)e^{j\varphi}$$

$$\frac{dx_s}{dt} = \left(\frac{dA_s}{dt} + jA_s\frac{d\varphi}{dt}\right)e^{j\varphi}. \qquad (13)$$

We can express this in terms of the partial spatial derivatives which include radial and angular velocity:

$$\frac{dx}{dt} = \frac{dx_s}{dt} = \left[\left(\frac{\partial A_s}{\partial r} + jA_sk\right)v_r(t) + \frac{\partial A_s}{\partial\alpha}v_\alpha(t)\right]e^{j\varphi} \qquad (14)$$

where $\partial\varphi/\partial r = \omega_0/c = k$ *(wave number) is from (5).*

We now consider three cases:

1) Radial Velocity = 0 – [$v_r(t) = \partial r/\partial t = 0$]

An object moves into the field of view at a constant distance from the sensor,

$$\frac{dx_s}{dt} = \frac{\partial A_s}{\partial\alpha}v_\alpha(t)\,e^{j\varphi} = A_r\frac{\partial A_\alpha}{\partial\alpha}v_\alpha(t)\,e^{j(\varphi+\theta)} \qquad (15)$$

where: $\theta = 0$ (16)

2) Angular Velocity = 0 – [$v_\alpha(t) = \partial\alpha / \partial t = 0$]

An object moves toward or away from the sensor along a radial line.

$$\frac{dx_s}{dt} = \left[\left(\frac{\partial A_s}{\partial r} + jA_s k\right) v_r(t)\right] e^{j\varphi} = \left[\left| A_\alpha \frac{\partial A_r}{\partial r} + jA_\alpha A_r k \right| v_r(t)\right] e^{j(\varphi+\theta)} \quad (17)$$

where: $$\theta = \tan^{-1}\left(\frac{A_r k}{\partial A_r / \partial r}\right) \quad (18)$$

3) General Case

$$\frac{dx_s}{dt} = \left|\left(A_\alpha \frac{\partial A_r}{\partial r} + jA_r A_\alpha k\right) v_r(t) + A_r \frac{\partial A_\alpha}{\partial \alpha} v_\alpha(t)\right| e^{j(\varphi+\theta)} \quad (19)$$

where: $$\theta = \tan^{-1}\left(\frac{A_r A_\alpha k\, v_r(t)}{A_\alpha \frac{\partial A_r}{\partial r} v_r(t) + A_r \frac{\partial A_\alpha}{\partial \alpha} v_\alpha(t)}\right) \quad (20)$$

From (16) through (20) we see that the phase of the derivative of x can be expressed as:

$$\angle\, {}^{dx}\!/_{dt} = \varphi + \theta, \quad (21)$$

where $\varphi = \varphi(r(t))$ and $\theta = \theta(r(t), \alpha(t))$.

Equation 21 is the major point of the derivation: the phase of the derivative of the signal in [I, Q] space is the phase of the original signal, φ, plus a phase distortion term θ. We need to bound the distortion term and determine its affect on the processed signal.

B. The phase distortion term

θ is the corrupting element in our scheme. If θ has a predictable and stable relation to φ, (21) becomes a useful means to determine the phase (and thereby the distance) of a moving object. For the case of radial motion, we can gain some insight from finite difference approximations:

$$\theta \approx \tan^{-1}\left(\frac{k\,\Delta r}{\Delta A_s / A_s}\right), \text{ or,}$$

$$\theta \approx \tan^{-1}\left(\frac{\Delta\varphi}{\Delta A_s / A_s}\right). \quad (22)$$

Equation 22 shows that the phase distortion is related to both the change in phase and the percentage change in amplitude.

C. Behaviour in Time-of-Flight systems

Case 1: angular motion, radial velocity is zero.

This is the simplest case represented in Eq.15, the phase distortion term, θ, is zero. The phase is unchanged in the VDD signal versus the original I/Q signal. If a user steps into the field of view from outside the field of view, the system responds with no phase distortion.

Case 2: radial motion, angular velocity is zero.

Motion along a radial line generates a more complicated result. Collecting results from (5), (9a), (11a), (18) and (21) we find:

$$\varphi(r) = r\frac{\omega_0}{c} = rk, \quad (5)$$

$$A_r(r) = A_0 \frac{R}{r^N} \quad (9a)$$

$$\frac{\partial A_r(r)}{\partial t} = -NA_0 \frac{R}{r^{N+1}} v_r(t); \quad (11a)$$

$$\theta = \tan^{-1}\left(\frac{A_r k}{\partial A_r / \partial r}\right) \quad (18)$$

$$\angle\, {}^{dx}\!/_{dt} = \varphi + \theta, \quad (21)$$

$$\angle\, {}^{dx}\!/_{dt} = rk + \tan^{-1}\left(-\frac{A_0 R k r^{N+1}}{r^N N A_0 R}\right) = rk + \tan^{-1}\left(-\frac{kr}{N}\right). \quad (23)$$

Applying the small angle approximation,

$$\underset{x\to 0}{Limit}\,(\tan^{-1}(x)) = x,$$

we have:

$$\angle\, {}^{dx}\!/_{dt} \approx rk - \left(\frac{rk}{N}\right), \quad (24a)$$

$$\angle\, {}^{dx}\!/_{dt} \approx rk\left(1 - \frac{1}{N}\right), \quad (24b)$$

$$\angle\, {}^{dx}\!/_{dt} \approx \varphi\left(1 - \frac{1}{N}\right), \quad (24c)$$

or, for N=2,

$$\angle\, {}^{dx}\!/_{dt} \approx \varphi\left(1 - \frac{1}{2}\right) = {}^1\!/_2\,\varphi. \quad (24d)$$

Equation (24c) shows that for radial motion the phase is directly proportional to the original phase via the proportionality constant, (1 - 1/N). For a square law system the phase is precisely half of the original phase [N=2, (1 – 1/N) = ½] as seen in (24d). Recalling the original signal model, the power law begins at N=2 for distances under 1m, changes to N=3 for distance between about 1m and 2.8m, and moves to N=4 at 2.8m and beyond. So the VDD processing compresses the distance vs phase shift curve such that objects moving radially appear closer, but the curve is very consistent for human sized objects within 1m of the sensor.

Case 3: Motion along the diagonal. Here we look at the 'in between' case where $v_\alpha = v_r$. [Note: we could also consider the case of $v_\alpha = -v_r$, but the sense of the a component changes sign across the center line, and effectively gives both results at the extreme angles.] Again collecting results from (5), (9a), (11a/b), (18) and (21) we find:

$$\varphi(r) = r\frac{\omega_0}{c} = rk\,, \tag{5}$$

$$A_r(r) = A_0\frac{R}{r^N} \tag{9a}$$

$$A_\alpha(\alpha) = \left(\tfrac{1}{2} + \tfrac{1}{2}\cos\left(\tfrac{\alpha}{\alpha_0}\pi\right)\right) \tag{9b}$$

$$\frac{\partial A_r(r)}{\partial t} = -NA_0\frac{R}{r^{N+1}}v_r(t); \tag{11a}$$

$$\frac{\partial A_\alpha(\alpha)}{\partial t} = -\frac{\pi}{2\alpha_0}\sin\left(\tfrac{\alpha}{\alpha_0}\pi\right)v_\alpha(t); \tag{11b}$$

$$\theta = \tan^{-1}\left(\frac{A_r A_\alpha k\, v_r(t)}{A_\alpha\frac{\partial A_r}{\partial r}v_r(t) + A_r\frac{\partial A_\alpha}{\partial \alpha}v_\alpha(t)}\right) \tag{18}$$

$$\angle\, {}^{dx}\!/_{dt} = \varphi + \theta\,, \tag{21}$$

and assuming $v_r(t) = v_\alpha(t)$;

$$\frac{\partial A_\alpha(\alpha)}{\partial t} = -\frac{\pi}{2\alpha_0}\sin\left(\tfrac{\alpha}{\alpha_0}\pi\right)v_\alpha(t); \tag{11b}$$

$$\begin{aligned}\angle\, {}^{dx}\!/_{dt} &= rk + \tan^{-1}\left(\left(\frac{A_r A_\alpha k}{A_\alpha\frac{\partial A_r}{\partial r} + A_r\frac{\partial A_\alpha}{\partial \alpha}}\right)\right)\\ &= rk + \tan^{-1}\left(-\frac{k}{\frac{\partial A_r/\partial r}{A_r} + \frac{\partial A_\alpha/\partial\alpha}{A_\alpha}}\right)\\ &= rk + \tan^{-1}\left(-\frac{rk}{N + \frac{\frac{\pi r}{2\alpha_0}\sin\left(\frac{\alpha}{\alpha_0}\pi\right)}{\left(\frac{1}{2} + \frac{1}{2}\cos\left(\frac{\alpha}{\alpha_0}\pi\right)\right)}}\right)\end{aligned} \tag{23}$$

Equation (23) shows that locations near the center line give the same result as radial velocities (the second term in the denominator goes to zero at the center), while locations at the edge of the field cause an effective modulation of the denominator. An object entering the field on a diagonal toward the sensor results in an increase in magnitude due to the α dependence that adds to the magnitude increase due to the power law r dependence. The denominator of the distortion term gets larger, and the phase distortion gets smaller. An object leaving the field along the same diagonal has decreasing magnitude due to the α dependence, but increasing magnitude due to the power law dependence. The denominator of the distortion term gets smaller, and the phase distortion larger. The net result is that the apparent distance entering the field is larger than the apparent distance leaving the field. This is what we would expect from the two velocities considered separately in (15) and (17).

The conclusion is that VDD represents a distortion of phase that can be viewed as weighted velocities. Objects moving toward the sensor appear closer, but they are generally more interesting objects. Objects moving across the field appear farther away, but they also have a distinct signature: the angle entering the field is positive on entering and negative on leaving, but otherwise of the same magnitude. On the other hand, the α dependence comes from the restricted angle of radiation of the LED. LED's with large radiation angles will exhibit much smaller α dependence, and most of the phase will be due to motion along r, ideal for determining the distance of moving objects in a large field of view. LED's with small radiation angles will show large a dependence and strong positive followed by negative signatures, ideal for counting objects crossing the field of view. VDD is therefore a useful technique to generate orthogonal and useful data in an active IR system, free from the corruption of steady state signals such as crosstalk and backscatter.

V. BANDLIMITED DERIVATIVES: REDUCING NOISE

Derivatives are noisy: in the frequency domain the ideal derivative has a zero at the origin (DC) and nothing else. The power spectral transfer function rises without limit as frequency increases creating an untenable noise situation in a real system. Something must be done to control the noise bandwidth of the system to make the technique usable. In such situations it is typical to apply bandlimiting to the derivatives to limit the noise. There are three ways to include bandlimiting in this system:

1) Bandlimit the original [I,Q] data to limit the input noise bandwidth to the derivative,

2) Filter the output of the derivative processing to limit the final output noise bandwidth, and,

3) Perform a discrete 'derivative' as a two sample difference, and modify the spacing of the samples to allow more phase difference to accumulate signal relative to the existing noise before calculating the distance.

In the following we explore all three, and find that all are related and useful in building a robust system.

A. Bandlimiting in the [I,Q] Space

In the current system the [I,Q] space is the result of several stages of signal processing and already contains almost 7 orders of magnitude of bandwidth reduction from the PIN diode input to the digital output. Although detailed analysis of the signal chain is beyond the scope of this paper, we can say that the signal chain limits bandwidth at 5 places to control noise amplitudes as gain increases along the chain. These include:

1) Front end bandlimiting to approximately 5MHz (rolling off at 6dB/oct above that frequency),
2) High Q bandpass filtering reducing bandwidth to 1MHz,
3) Demodulator limiting baseband output to 7kHz,
4) ADC output filtering reduces bandwidth to a few kHz, and,
5) the final digital lpf reduces bandwidth to 1Hz.

The result is that there is no significant noise aliasing in the signal chain up to the output and noise at the final output filter has a bandwidth of about 1Hz.

B. Bandlimiting the derivative

One of the fortunate properties of derivative processing is linearity, and it therefore inherits all of the traditional properties of linear systems. In particular, applying a linear filter either before or after the derivative block has a similar effect. We've already shown that there is significant bandlimiting applied in the [I,Q] space before the derivative processing, and we now consider applying bandlimiting afterward.

We begin by stating that the first difference is a valid approximation to the derivative and is often used in numerical solutions to differential equations [6][7]. In fact, its pedigree reaches back to the first definition of the derivative by Isaac Newtown [5]. For our purposes, the discrete first difference is identical to the first derivative, bandlimited to the appropriate Nyquist frequency range. As long as we are not aliasing our signals the two yield the same result.

In continuous time the derivative is often bandlimited by adding lowpass poles to the transfer function. In the discrete domain it is more convenient to apply a simple moving average filter. A moving average filter has a rectangular impulse response, and simply averages the last M samples of a given signal or data stream to create the new data stream. In the frequency domain it has a general lowpass characteristic, with a corner frequency falling as M increases, and transmission zeros creating a comb-like response. Figure 3 [8] shows the frequency domain behaviour of the moving average.

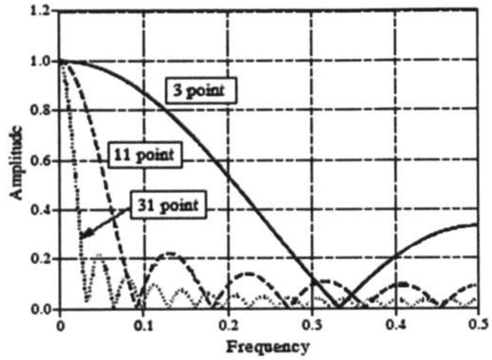

Figure 3: Frequency response of moving average

For our purposes, it is of interest to determine the affect of applying a moving average lpf to the discrete derivative (first difference). We begin with a definition of the discrete first difference:

$$\Delta x_i = x_i - x_{i-1} \tag{24}$$

A moving average filter can be implemented as a simple weighted sum over M samples:

$$\begin{aligned}\frac{1}{M}\sum_{j=i-M}^{i}\Delta x_j &= \frac{1}{M}\sum_{j=i-M}^{i}(x_j - x_{j-1}) \\ &= \frac{1}{M}\left(\sum_{j=i-M}^{i}x_j - \sum_{j=i-M}^{i}x_{j-1}\right)\end{aligned} \tag{25}$$

but the second sum can be rearranged:

$$\sum_{j=i-M}^{i}x_{j-1} = \sum_{j=i-M}^{i}x_j - x_j + x_{j-M-1} \ , \tag{26}$$

and substituted in (17) yielding:

$$\left(\frac{1}{M}\right)\sum_{j=i-M}^{i}\Delta x_j = \left(\frac{1}{M}\right)(x_j - x_{j-(M+1)}) \tag{27}$$

Equation (27) shows that bandlimiting the derivative can be accomplished simply by decreasing the sample rate applied to the first difference: we simply subtract samples separated by M periods. If the object is in uniform motion over the M samples, then the result of (27) is the same as the single sample difference, but the noise contritbution is reduced by a factor of M. If we don't divide by M, and just have a running sum of the first differences, the signal is amplified by a factor of M while the noise contribution remains constant. This makes intuitive sense: an object moving at constant velocity will show greater phase differences when samples are more widely spaced, while the noise contributions will be approximately the same in both cases (since the noise is white, the samples are uncorrelated and subtracting any two samples yields the same noise content regardless of where they occurred in the sequence). Larger phase differences and constant noise result in larger SNR. In fact, halving the sample rate will increase SNR by approximately 6dB. This approach is used to great effect in the adaptive sample rate method later on.

C. Issues of Amplitude, SNR, and Dynamic Range

SNR and Dynamic Range depend on the magnitude of the processed signal, so we should revisit the amplitude of the derivative. For the remainder of the paper we will restrict ourselves to objects in the center of the field of view with no α dependence. From (13) we have directly:

$$\left|\frac{dx}{dt}\right| = \left(\left(\frac{\partial A_s}{\partial r}\right)^2 + (A_s k)^2\right)^{1/2} v(t) \tag{28}$$

Substituting for the spatial derivative of A_s and performing some algebra we have:

$$\left|\frac{dx}{dt}\right| = \left(\left(\frac{N}{r}\right)^2 + (k)^2\right)^{1/2} A_s\, v(t) \tag{29}$$

Assuming we are within 1m (for a human sized object) our system is power law (N=2) and the operating frequency is 5MHz [$k = (2\pi \times 5 \times 10^6)/\ 3 \times 10^8 = 0.105$] this reduces to:

$$\left|\frac{dx}{dt}\right| = \left(\left(\frac{2}{r}\right)^2 + (0.105)^2\right)^{1/2} A_s\, v(t) \approx \frac{2A_s\, v(t)}{r}, \tag{30}$$

And further substituting for A_s as in (6):

$$\left|\frac{dx}{dt}\right| \approx \frac{2A_0\, v(t)}{r^{N+1}} = \frac{2A_0\, v(t)}{r^3}, \tag{31}$$

for N=2.

Equation (31) indicates that the amplitude of the derivative is proportional to the velocity and inversely proportional to the cube of the distance. If we devise a system where we reduce the sample rate for lower velocities and larger r, we can compensate for these losses.

D. Signal Processing Implementation

There is a deceptively simple method to accomplish the above sample rate variation: we take a first sample at some time t, and take another sample when the output changes by fixed amount. This automatically adjust the effective M of our derivative moving average in (27) to produce a signal of known amplitude. As stated above, the noise contribution is constant for any two samples (white assumption on noise), regardless of M, yielding a technique that puts lower bounds on the SNR.

The diagram below shows a block diagram of a possible implementation.

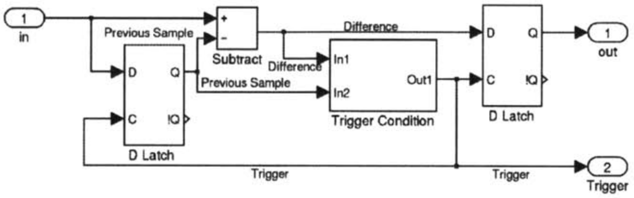

FIG. 4 DIFFERENTIATOR BLOCK DIAGRAM

Assume at the start that a previous sample has been acquired by the D Latch on the left. The Subtract block continuously monitors the difference between this previous sample and the current sample. When this difference satisfies the Trigger Condition block (the difference must be large enough, and the signal should be above some squelch level) it generates a trigger (sampling) pulse. The trigger latches the difference (our derivative of interest) into the output latch on the right, and acquires a new sample in the input latch on the left. The trigger can further be used to clock any subsequent filtering or any other signal processing. The triggering condition can be tuned to optimize speed, accuracy, and SNR. The resulting system is simple, but can optimally shift its gain and sampling rate to maintain a minimum SNR.

VI. DISTANCE-OF-MOTION SENSING

The system of Figure 4 is applied to the vector [I,Q] signal and effectively provides weighted average, lowpass filtered first difference [I,Q] signals at its output. The phase of that signal indicates the distance of the last motion sensed by the system.

In additional the information obtained from motion distance sensing can be used to dynamically calibrate the static distance sensing as shown in Fig.5. By using the phase of the derivative and the corresponding original I/Q vectors, it is possible to dynamically reconstruct the static component of the signal. Over time this allows us to obtain the environmental backscatter component and use it to improve the static proximity results. Further work is needed to determine whether the derivative processing is sufficient for most proximity applications, or whether an enhanced processor using the derivative method to calibrate the static sensor is advantageous. We are currently exploring all methods and their interaction.

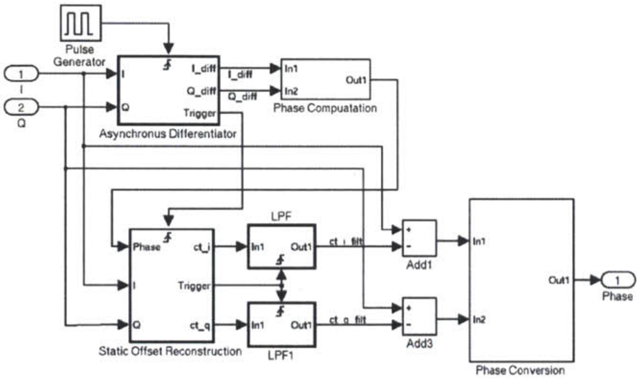

FIG. 5 DYNAMIC CALIBRATION BLOCK DIAGRAM

E. Simulation Results

Figure 6 shows the typical transfer characteristics of all three methods discussed so far: conventional, vector domain differentiation, and dynamic calibration.

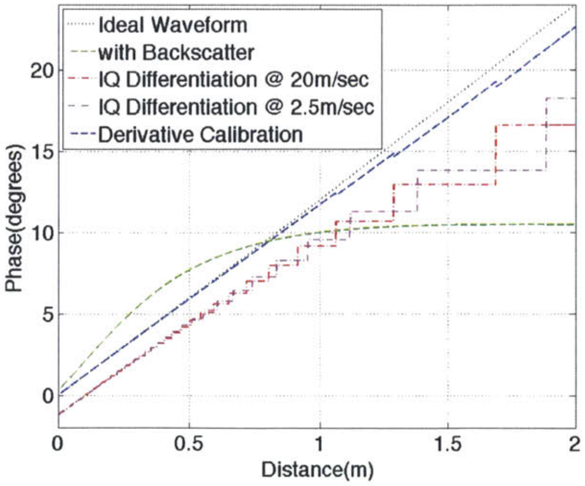

FIG. 6 - PHASE VS DISTANCE TRANSFER CHARACTERISTICS

1. The black line shows the ideal response: it is the phase delay due to the distance of the object of interest.
2. The green line shows the result of a conventional static TOF system with significant backscatter: an object at 40cm with 70% reflectivity.
3. The red line shows the result of vector domain differentiation with the same backscatter and the object of interest moving at 20 meters per second. This is equivalent to sensing a human sized object moving at 40 mph.
4. The orange line is the vector domain differentiation system with the same backscatter and the o.o.i. moving at 2.5 meters per second. This is equivalent to someone running by your laptop at 4mph.
5. The blue line represents the output of a static TOF prox system calibrated using the vector domain differentiation.

The plot below shows the time domain waveforms of the dynamic calibration obtained through the vdd system for a an object moving uniformly back and forth with a constant speed of four meters per second. It is clear that the static system benefits from the dynamic calibration, improving its accuracy with each cycle.

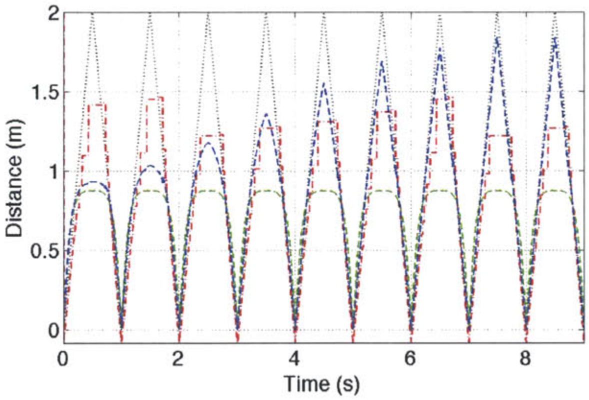

FIG. 7 - CALIBRATION WAVEFORMS

VII. CONCLUSIONS

This paper introduced a new technique applicable to active IR proximity sensing. The VDD: Vector Domain Differentiation technique provides more than traditional motion sensing, it combines motion sensing with distance sensing, and provides both in the presence of large environmental backscatter signals. As an added benefit, VDD has been used to calibrate a traditional TOF proximity system, learning over time the backscatter environment. We anticipate that these features will be valuable in future proximity sensors.

References

[1] "A special report on Smart Systems", The Economist, November 6th, 2010.

[2] G. C. M. Meijr et al., "Smart Sensor Systems", Wiley, 2008.

[3] ISL29028 Datasheet, available online at www.intersil.com

[4] S. Burak Goktak, H. Yalcin, C, Bamji, "A Time-Of-Flight Depth Sensor – System Description, Issues and Solutions", Canesta White paper, available at www. canesta.com

[5] D. W. Ritter et al., "Active IR Proximity Sensing Using Time of Flight Techniques", IEC, 2010.

[6] Newton, Isaac, *Principia*, Book III, Lemma V, Case 1

[7] William F. Ames, *Numerical Methods for Partial Differential Equations*, Section 1.6. Academic Press, New York, 1977. ISBN 0-12-056760-1

[8] Francis B. Hildebrand, *Finite-Difference Equations and Simulations*, Section 2.2, Prentice-Hall, Englewood Cliffs, New Jersey, 1968

[9] Stephen W. Smith, *The Scientist's and Engineer's Guide to Digital Signal Processing*, Figure 15-2 et al, copyright ©1997-1998 by Steven W. Smith. For more information visit the book's website at: www.DSPguide.com.

APPENDIX A:

Figure A.1 shows an idealized proximity model including most important factors in determining the signal received at a PIN diode from an LED.

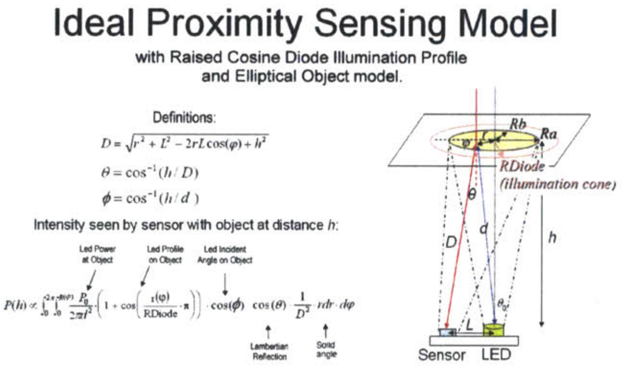

Ideal Proximity Sensing Model

with Raised Cosine Diode Illumination Profile
and Elliptical Object model.

Definitions:

$$D = \sqrt{r^2 + L^2 - 2rL\cos(\varphi) + h^2}$$

$$\theta = \cos^{-1}(h/D)$$

$$\phi = \cos^{-1}(h/d)$$

Intensity seen by sensor with object at distance *h*:

$$P(h) \propto \int_0^{2\pi}\int_0^{R(\varphi)} \underset{\text{Led Power at Object}}{\frac{P_0}{2\pi d^2}} \cdot \underset{\text{Led Profile on Object}}{\left(1 + \cos\left(\frac{r(\varphi)}{\text{RDiode}} \cdot \pi\right)\right)} \cdot \underset{\text{Led Incident Angle on Object}}{\cos(\phi)} \underset{\text{Lambertian Reflection}}{\cos(\theta)} \cdot \underset{\text{Solid angle}}{\frac{1}{D^2}} \, r dr \cdot d\varphi$$

Figure A.1 – Analytic Proximity Model

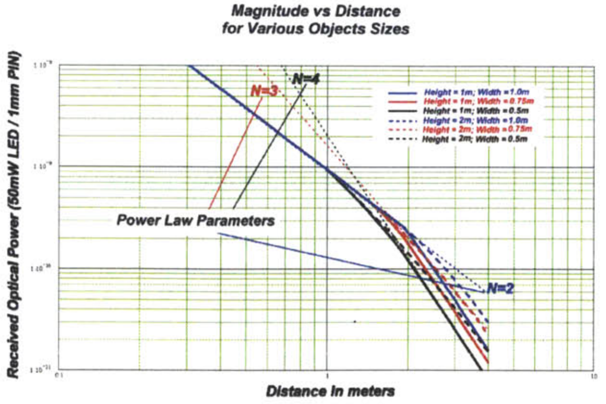

Figure A.2 – Magnitude vs Distance vs Object Size

Magnitude variations are shown in detail in Figure A.2. The kernel of the integral contains the following terms and definitions:

1) Definitions:
    a. P0: radiated power from LED
    b. d: distance from LED to point on object. Object assumed to be centered on LED axis.
    c. D: distance from point on object to PIN sensor.
    d. φ: polar coordinate angle spanning object
    e. r: polar coordinate radius spanning object
    f. RDiode: radius of illumination of LED at distance h.
    g. θ: angle from LED to point on object.
    h. ϕ: angle from point on object to PIN sensor.
2) Term : $(P_0/2\pi d^2)\times(1+\cos(\pi \times r(\phi)/\text{RDiode}))\cos(\phi)$: Led illumination profile across the object. Includes the inverse square (1/d2) and the loss due to glancing angle of incidence, cos(ϕ).
3) cos(θ): Lambertian reflection.
4) $1/D^2$: Inverse square loss from point source on object to PIN diode.
5) r dr dφ: polar differential area term on object.

From this model we can make an accurate reciprocal polynomial fit for human sized objects (1.5m x 0.5m), including the diode radiation profile for spatial angle dependence:

$$A_s(r) = \frac{A_0}{r^2\left(r^2 + ar + b\right)}\left(\tfrac{1}{2} + \tfrac{1}{2}\cos\left(\tfrac{\alpha}{\alpha_0}\pi\right)\right); \qquad \text{(A.1)}$$

where A_0=7.125e-09, a=-0.95, and b=3.1.

We can also generate a piecewise power law function for ease of analysis within the piecewise regions.

$$A_s(r,a) = A_0 \bullet if(r < r_1, 1/r^2, if(r < r_2, r_1/r^3, r_1 r_2/r^4)) \bullet \left(\tfrac{1}{2} + \tfrac{1}{2}\cos\left(\alpha/_{\alpha_0}\pi\right)\right) \tag{A.2}$$

Or:

$$A_s(r,a) = A_0 \frac{R}{r^N} \left(\tfrac{1}{2} + \tfrac{1}{2}\cos\left(\alpha/_{\alpha_0}\pi\right)\right) \tag{A.3}$$

where:

$R = 1$ *and* $N = 2$ *for* $r < r_1$

$R = r_1$ *and* $N = 3$ *for* $r_1 < r < r_2$;

$R = r_1 * r_2$ *and* $N = 4$ *for* $r > r_2$.

For human sized (ellipse: 1.5m x 0.5m) objects: $A_0 = 0.95 \times 10^{-9}$, $r_1 = 1.125$m, $r_2 = 2.8$m for a human sized object.

APPENDIX B:

We should include a brief note on the accuracy of the small angle approximation. For the current project, angles are small (< 22^0) and the approximation is well within the expected error of the system. A more general error bounding term can be derived from the Taylor series for the arctangent function and results in a maximum error bound of:

$$AngleError \le \left(\frac{1}{3}\left(\frac{rk}{N}\right)^3\right). \tag{14e}$$

Assuming a square law magnitude function, and substituting for the wave number we have:

$$AngleError \le \left(\frac{1}{24}\left(\frac{2\pi r}{\lambda}\right)^3\right). \tag{14e}$$

The percentage error is this error divided by (14b):

$$pError \le \left(\frac{1}{12}\left(\frac{2\pi r}{\lambda}\right)^2\right) = 3.29\left(\frac{r}{\lambda}\right)^2. \tag{14f}$$

For an error of less than 5%, we have:

$$0.05 \ge 3.29\left(\frac{r}{\lambda}\right)^2; \quad r \le 0.123\lambda. \tag{14f}$$

In the ISL29200 system $\lambda = 60$ meters, so $r < 7.38$ meters. The current system is designed to operate to 2 meters, giving a great deal of margin before the small angle approximation creates significant errors.

Appendix B

Data

Tables B.1 through B.4 show the least square estimate of the object parameters c_0, c_1, c_2 and the associated error, for a range of scenes simulated for a Pulsed TOF system. A total of 108 scenes with varying object size, shape and orientation were simulated, each scene representing series of simulation results for a rectangular sheet whose center is placed at a range of distances from the sensor. All scenes were simulated using an idealized point source with uniform radiant intensity. Each scene is marked with a 12 character "Scene Code", containing information of four parameters:

- Width: This parameters specifies the width of the rectangle. The width is oriented along the x-axis, which is also the direction that the diode is displace from the LED in the simulation. The scene code is in units of 0.1m, such that a width of 1.0m would be labeled as W10, a width of 40cm would be labeled as W04, etc.

- Height: This parameters specifies the height of the rectangle. The height is oriented along the y-axis, which is orthogonal to the direction the diode is displace from the LED in the simulation. The scene code is in units of 0.1m, such that a width of 1.0m would be labeled as H10, a width of 40cm would be labeled as H04, etc.

- Reflectivity: This parameter specifies the type of reflector the surface is modeled as. R00 indicates a diffuse object, R01 indicates an off-specular surface modeled using the Beckmann Distribution with $m = 0.1$, and R05 indicates a likewise off-specular surface modeled with $m = 0.5$.

- Object Orientation/Tilt: This parameter specifies the angle at which the object's surface is oriented with respect to the sensor, as well as as well the position of the object in the field of view. This tilt is in implemented by rotating the plane around the y-axis such that the surface normal is oriented at the sensor, and the center of the object is at a zenith angle equal to the tilt angle. The T00 represents tilt of 0 degrees, indicating the object is located along the z-axis, and the surface is parallel to the emittor/detector plane. T12, T06, and T04 represent a tilt of $\frac{\pi}{12}$, $\frac{\pi}{6}$, and $\frac{\pi}{4}$, respectively.

Tables B.5 through B.8 show similar results for a SWM TOF system for a 5MHz modulation frequency.

Table B.1: Object Parametrization of Systematically Generated Scenes for Pulsed TOF, Part 1 of 4

Scene Code	c_0	c_1	c_2	Error
W01H01R00T00	4.98E-03	-2.77E-02	9.66E-02	4.88E-04
W02H02R00T00	1.97E-02	-5.90E-02	9.57E-02	2.36E-04
W04H04R00T00	7.69E-02	-1.23E-01	9.57E-02	1.47E-04
W08H08R00T00	3.14E-01	-2.27E-01	9.69E-02	1.73E-04
W16H16R00T00	1.54E+00	-3.55E-01	9.84E-02	7.06E-05
W01H16R00T00	9.67E-02	9.63E-01	1.26E-01	3.32E-03
W02H08R00T00	8.17E-02	5.74E-02	1.03E-01	3.76E-04
W08H02R00T00	8.17E-02	5.74E-02	1.03E-01	3.76E-04
W16H01R00T00	9.67E-02	9.63E-01	1.26E-01	3.32E-03
W01H01R05T00	1.11E-02	-6.32E-02	2.75E-02	9.90E-04
W02H02R05T00	4.33E-02	-1.28E-01	2.76E-02	6.22E-04
W04H04R05T00	1.69E-01	-2.50E-01	2.79E-02	7.45E-04
W08H08R05T00	8.33E-01	-4.32E-01	2.86E-02	5.31E-04
W16H16R05T00	1.41E+01	-6.00E-01	2.93E-02	1.61E-05
W01H16R05T00	1.62E-01	7.22E-01	3.43E-02	5.97E-03
W02H08R05T00	1.79E-01	-2.12E-02	2.97E-02	5.36E-04
W08H02R05T00	1.79E-01	-2.12E-02	2.97E-02	5.36E-04
W16H01R05T00	1.62E-01	7.22E-01	3.43E-02	5.97E-03
W01H01R01T00	2.91E-01	-2.75E-01	2.58E-02	5.52E-04
W02H02R01T00	1.68E+00	-4.54E-01	2.63E-02	1.95E-04
W04H04R01T00	7.33E+01	-5.69E-01	2.66E-02	5.92E-07
W08H08R01T00	2.97E+07	-6.01E-01	2.67E-02	8.44E-18
W16H16R01T00	-2.61E+12	-8.46E-01	2.67E-02	9.19E-25
W01H16R01T00	8.15E-01	-2.22E-01	2.65E-02	1.11E-04
W02H08R01T00	3.50E+00	-4.54E-01	2.65E-02	4.05E-05
W08H02R01T00	3.50E+00	-4.54E-01	2.65E-02	4.05E-05
W16H01R01T00	8.15E-01	-2.22E-01	2.65E-02	1.11E-04

Table B.2: Object Parametrization of Systematically Generated Scenes for Pulsed TOF, Part 2 of 4

Scene Code	c_0	c_1	c_2	Error
W01H01R00T12	4.93E-03	-2.71E-02	9.36E-02	6.09E-04
W02H02R00T12	1.94E-02	-6.00E-02	9.22E-02	1.90E-04
W04H04R00T12	7.62E-02	-1.22E-01	9.26E-02	1.38E-04
W08H08R00T12	3.12E-01	-2.25E-01	9.37E-02	1.82E-04
W16H16R00T12	1.55E+00	-3.48E-01	9.51E-02	6.83E-05
W01H16R00T12	8.87E-02	8.42E-01	1.20E-01	3.18E-03
W02H08R00T12	8.11E-02	5.48E-02	9.96E-02	3.84E-04
W08H02R00T12	5.96E-02	2.47E-03	9.81E-02	2.19E-04
W16H01R00T12	1.50E-02	7.15E-03	9.98E-02	1.87E-04
W01H01R05T12	1.11E-02	-6.22E-02	2.66E-02	1.16E-03
W02H02R05T12	4.25E-02	-1.28E-01	2.66E-02	6.25E-04
W04H04R05T12	1.68E-01	-2.49E-01	2.70E-02	7.41E-04
W08H08R05T12	8.41E-01	-4.27E-01	2.77E-02	5.17E-04
W16H16R05T12	1.63E+01	-5.85E-01	2.83E-02	1.16E-05
W01H16R05T12	1.54E-01	6.52E-01	3.28E-02	5.74E-03
W02H08R05T12	1.77E-01	-2.45E-02	2.87E-02	5.44E-04
W08H02R05T12	1.30E-01	-8.13E-02	2.82E-02	2.56E-04
W16H01R05T12	3.35E-02	-3.29E-02	2.85E-02	3.14E-04
W01H01R01T12	2.95E-01	-2.70E-01	2.51E-02	4.82E-04
W02H02R01T12	1.72E+00	-4.42E-01	2.55E-02	1.61E-04
W04H04R01T12	9.39E+01	-5.53E-01	2.58E-02	3.40E-07
W08H08R01T12	5.82E+07	-5.82E-01	2.59E-02	1.95E-18
W16H16R01T12	-7.67E+12	-1.11E+00	2.59E-02	1.27E-25
W01H16R01T12	8.18E-01	-2.23E-01	2.57E-02	1.55E-04
W02H08R01T12	3.77E+00	-4.34E-01	2.57E-02	2.85E-05
W08H02R01T12	3.35E+00	-4.50E-01	2.57E-02	4.58E-05
W16H01R01T12	6.95E-01	-2.47E-01	2.56E-02	6.39E-05

Table B.3: Object Parametrization of Systematically Generated Scenes for Pulsed TOF, Part 3 of 4

Scene Code	c_0	c_1	c_2	Error
W01H01R00T06	4.77E-03	-2.71E-02	8.39E-02	6.26E-04
W02H02R00T06	1.85E-02	-6.10E-02	8.28E-02	1.72E-04
W04H04R00T06	7.31E-02	-1.18E-01	8.37E-02	1.66E-04
W08H08R00T06	3.06E-01	-2.10E-01	8.49E-02	1.88E-04
W16H16R00T06	1.60E+00	-3.02E-01	8.62E-02	4.39E-05
W01H16R00T06	8.60E-02	7.90E-01	1.06E-01	3.37E-03
W02H08R00T06	8.04E-02	5.35E-02	8.96E-02	2.99E-04
W08H02R00T06	3.03E-02	-5.94E-02	8.45E-02	3.41E-05
W16H01R00T06	7.73E-03	-2.78E-02	8.48E-02	2.06E-04
W01H01R05T06	1.07E-02	-6.26E-02	2.38E-02	1.06E-03
W02H02R05T06	4.03E-02	-1.30E-01	2.38E-02	6.63E-04
W04H04R05T06	1.63E-01	-2.44E-01	2.42E-02	8.05E-04
W08H08R05T06	8.89E-01	-4.08E-01	2.49E-02	4.37E-04
W16H16R05T06	2.80E+01	-5.38E-01	2.54E-02	3.26E-06
W01H16R05T06	1.38E-01	5.26E-01	2.89E-02	5.41E-03
W02H08R05T06	1.73E-01	-3.48E-02	2.56E-02	4.82E-04
W08H02R05T06	6.64E-02	-1.40E-01	2.43E-02	2.82E-04
W16H01R05T06	1.72E-02	-6.99E-02	2.41E-02	3.45E-04
W01H01R01T06	2.81E-01	-2.71E-01	2.24E-02	6.03E-04
W02H02R01T06	1.80E+00	-4.25E-01	2.29E-02	1.66E-04
W04H04R01T06	2.11E+02	-5.07E-01	2.32E-02	6.08E-08
W08H08R01T06	3.90E+09	-5.23E-01	2.32E-02	2.83E-22
W16H16R01T06	9.73E+11	-9.04E-01	2.32E-02	1.32E-25
W01H16R01T06	8.24E-01	-2.22E-01	2.30E-02	1.55E-04
W02H08R01T06	3.95E+00	-4.25E-01	2.31E-02	3.28E-05
W08H02R01T06	3.17E+00	-4.30E-01	2.30E-02	5.57E-05
W16H01R01T06	4.47E-01	-2.90E-01	2.27E-02	3.64E-04

Table B.4: Object Parametrization of Systematically Generated Scenes for Pulsed TOF, Part 4 of 4

Scene Code	c_0	c_1	c_2	Error
W01H01R00T04	4.38E-03	-2.44E-02	7.11E-02	7.16E-04
W02H02R00T04	1.72E-02	-5.17E-02	7.09E-02	2.18E-04
W04H04R00T04	6.84E-02	-1.00E-01	7.14E-02	1.29E-04
W08H08R00T04	2.95E-01	-1.71E-01	7.23E-02	1.00E-04
W16H16R00T04	1.53E+00	-2.39E-01	7.31E-02	1.81E-05
W01H16R00T04	7.90E-02	7.13E-01	8.74E-02	3.06E-03
W02H08R00T04	7.89E-02	7.39E-02	7.59E-02	2.74E-04
W08H02R00T04	2.09E-02	-5.53E-02	7.11E-02	1.97E-04
W16H01R00T04	5.28E-03	-2.75E-02	7.09E-02	4.52E-04
W01H01R05T04	1.01E-02	-6.14E-02	1.94E-02	1.25E-03
W02H02R05T04	3.88E-02	-1.24E-01	1.95E-02	7.77E-04
W04H04R05T04	1.61E-01	-2.31E-01	1.99E-02	7.84E-04
W08H08R05T04	1.10E+00	-3.69E-01	2.05E-02	2.33E-04
W16H16R05T04	1.27E+02	-4.53E-01	2.08E-02	1.01E-07
W01H16R05T04	1.12E-01	3.39E-01	2.29E-02	4.69E-03
W02H08R05T04	1.67E-01	-4.71E-02	2.09E-02	4.72E-04
W08H02R05T04	4.72E-02	-1.33E-01	1.96E-02	7.11E-04
W16H01R05T04	1.21E-02	-6.77E-02	1.94E-02	8.26E-04
W01H01R01T04	2.83E-01	-2.55E-01	1.84E-02	5.90E-04
W02H02R01T04	3.08E+00	-3.65E-01	1.88E-02	3.24E-05
W04H04R01T04	2.97E+03	-4.18E-01	1.89E-02	1.53E-10
W08H08R01T04	5.87E+11	-7.74E-01	1.89E-02	2.20E-25
W16H16R01T04	5.77E+11	-7.69E-01	1.89E-02	2.21E-25
W01H16R01T04	7.82E-01	-2.43E-01	1.88E-02	6.52E-05
W02H08R01T04	6.66E+00	-3.75E-01	1.89E-02	8.86E-06
W08H02R01T04	4.60E+00	-3.65E-01	1.89E-02	1.39E-05
W16H01R01T04	3.49E-01	-2.64E-01	1.85E-02	4.93E-04
			Average	6.81E-4
			Max	5.97E-3

Table B.5: Object Parametrization of Systematically Generated Scenes for SWM TOF, Part 1 of 4

Scene Code	c_0	c_1	c_2	Error
W01H01R00T00	4.98E-03	-2.77E-02	9.66E-02	4.88E-04
W02H02R00T00	1.97E-02	-5.90E-02	9.57E-02	2.36E-04
W04H04R00T00	7.69E-02	-1.23E-01	9.57E-02	1.47E-04
W08H08R00T00	3.14E-01	-2.27E-01	9.69E-02	1.73E-04
W16H16R00T00	1.54E+00	-3.55E-01	9.84E-02	7.06E-05
W01H16R00T00	9.67E-02	9.63E-01	1.26E-01	3.32E-03
W02H08R00T00	8.17E-02	5.74E-02	1.03E-01	3.76E-04
W08H02R00T00	8.17E-02	5.74E-02	1.03E-01	3.76E-04
W16H01R00T00	9.67E-02	9.63E-01	1.26E-01	3.32E-03
W01H01R05T00	1.11E-02	-6.32E-02	2.75E-02	9.90E-04
W02H02R05T00	4.33E-02	-1.28E-01	2.76E-02	6.22E-04
W04H04R05T00	1.69E-01	-2.50E-01	2.79E-02	7.45E-04
W08H08R05T00	8.33E-01	-4.32E-01	2.86E-02	5.31E-04
W16H16R05T00	1.41E+01	-6.00E-01	2.93E-02	1.61E-05
W01H16R05T00	1.62E-01	7.22E-01	3.43E-02	5.97E-03
W02H08R05T00	1.79E-01	-2.12E-02	2.97E-02	5.36E-04
W08H02R05T00	1.79E-01	-2.12E-02	2.97E-02	5.36E-04
W16H01R05T00	1.62E-01	7.22E-01	3.43E-02	5.97E-03
W01H01R01T00	2.91E-01	-2.75E-01	2.58E-02	5.52E-04
W02H02R01T00	1.68E+00	-4.54E-01	2.63E-02	1.95E-04
W04H04R01T00	7.33E+01	-5.69E-01	2.66E-02	5.92E-07
W08H08R01T00	2.70E+07	-5.46E-01	2.67E-02	8.44E-18
W16H16R01T00	2.94E+08	1.25E-06	2.67E-02	1.51E-29
W01H16R01T00	8.15E-01	-2.22E-01	2.65E-02	1.11E-04
W02H08R01T00	3.50E+00	-4.54E-01	2.65E-02	4.05E-05
W08H02R01T00	3.50E+00	-4.54E-01	2.65E-02	4.05E-05
W16H01R01T00	8.15E-01	-2.22E-01	2.65E-02	1.11E-04

Table B.6: Object Parametrization of Systematically Generated Scenes for SWM TOF, Part 2 of 4

W01H01R00T12	5.15E-03	-2.91E-02	9.28E-02	3.64E-04
W02H02R00T12	2.03E-02	-6.19E-02	9.21E-02	1.51E-04
W04H04R00T12	7.96E-02	-1.24E-01	9.26E-02	1.41E-04
W08H08R00T12	3.28E-01	-2.27E-01	9.37E-02	1.72E-04
W16H16R00T12	1.64E+00	-3.49E-01	9.52E-02	6.14E-05
W01H16R00T12	9.08E-02	8.12E-01	1.19E-01	3.20E-03
W02H08R00T12	8.35E-02	4.15E-02	9.90E-02	3.03E-04
W08H02R00T12	8.40E-02	6.40E-02	9.99E-02	4.10E-04
W16H01R00T12	9.07E-02	8.69E-01	1.20E-01	3.21E-03
W01H01R05T12	1.15E-02	-6.52E-02	2.64E-02	8.22E-04
W02H02R05T12	4.43E-02	-1.32E-01	2.66E-02	5.72E-04
W04H04R05T12	1.76E-01	-2.53E-01	2.70E-02	7.43E-04
W08H08R05T12	8.98E-01	-4.31E-01	2.77E-02	4.73E-04
W16H16R05T12	1.87E+01	-5.87E-01	2.83E-02	8.93E-06
W01H16R05T12	1.57E-01	6.23E-01	3.26E-02	5.69E-03
W02H08R05T12	1.81E-01	-4.33E-02	2.86E-02	4.03E-04
W08H02R05T12	1.83E-01	-1.61E-02	2.87E-02	5.81E-04
W16H01R05T12	1.55E-01	6.64E-01	3.29E-02	5.80E-03
W01H01R01T12	2.98E-01	-2.81E-01	2.50E-02	5.25E-04
W02H02R01T12	1.80E+00	-4.50E-01	2.55E-02	1.71E-04
W04H04R01T12	1.09E+02	-5.58E-01	2.58E-02	2.92E-07
W08H08R01T12	7.22E+07	-4.39E-01	2.59E-02	7.25E-19
W16H16R01T12	2.94E+08	-1.29E-06	2.59E-02	5.16E-30
W01H16R01T12	8.26E-01	-2.47E-01	2.56E-02	9.96E-05
W02H08R01T12	4.03E+00	-4.51E-01	2.57E-02	3.08E-05
W08H02R01T12	3.51E+00	-4.49E-01	2.57E-02	4.18E-05
W16H01R01T12	8.07E-01	-2.24E-01	2.57E-02	9.09E-05

Table B.7: Object Parametrization of Systematically Generated Scenes for SWM TOF, Part 3 of 4

W01H01R00T06	5.72E-03	-3.06E-02	8.34E-02	1.85E-03
W02H02R00T06	2.24E-02	-6.31E-02	8.34E-02	1.42E-04
W04H04R00T06	8.86E-02	-1.24E-01	8.40E-02	1.53E-04
W08H08R00T06	3.75E-01	-2.18E-01	8.51E-02	1.45E-04
W16H16R00T06	2.00E+00	-3.07E-01	8.63E-02	2.84E-05
W01H16R00T06	9.47E-02	6.57E-01	1.03E-01	2.99E-03
W02H08R00T06	9.25E-02	1.91E-02	8.84E-02	1.77E-04
W08H02R00T06	9.32E-02	9.94E-02	9.08E-02	6.14E-04
W16H01R00T06	9.28E-02	8.76E-01	1.07E-01	3.70E-03
W01H01R05T06	1.27E-02	-6.95E-02	2.37E-02	2.14E-03
W02H02R05T06	4.91E-02	-1.37E-01	2.39E-02	6.00E-04
W04H04R05T06	2.00E-01	-2.59E-01	2.43E-02	7.26E-04
W08H08R05T06	1.18E+00	-4.22E-01	2.50E-02	2.97E-04
W16H16R05T06	4.89E+01	-5.41E-01	2.54E-02	1.12E-06
W01H16R05T06	1.51E-01	4.02E-01	2.81E-02	4.43E-03
W02H08R05T06	2.00E-01	-8.34E-02	2.54E-02	2.55E-04
W08H02R05T06	1.97E-01	6.37E-03	2.59E-02	8.10E-04
W16H01R05T06	1.41E-01	5.43E-01	2.89E-02	5.59E-03
W01H01R01T06	3.25E-01	-2.97E-01	2.24E-02	1.53E-03
W02H02R01T06	2.65E+00	-4.30E-01	2.30E-02	7.80E-05
W04H04R01T06	4.13E+02	-5.06E-01	2.32E-02	1.50E-08
W08H08R01T06	2.86E+08	-1.38E-02	2.32E-02	3.71E-23
W16H16R01T06	2.94E+08	1.71E-06	2.32E-02	9.78E-30
W01H16R01T06	9.36E-01	-2.96E-01	2.29E-02	8.18E-05
W02H08R01T06	7.24E+00	-4.52E-01	2.31E-02	1.59E-05
W08H02R01T06	4.22E+00	-4.20E-01	2.31E-02	2.37E-05
W16H01R01T06	6.88E-01	-2.65E-01	2.29E-02	1.12E-04

Table B.8: Object Parametrization of Systematically Generated Scenes for SWM TOF, Part 4 of 4

W01H01R00T04	6.66E-03	-3.03E-02	7.08E-02	8.73E-04
W02H02R00T04	2.65E-02	-5.82E-02	7.14E-02	5.99E-05
W04H04R00T04	1.06E-01	-1.11E-01	7.19E-02	7.69E-05
W08H08R00T04	4.64E-01	-1.86E-01	7.27E-02	5.13E-05
W16H16R00T04	2.47E+00	-2.58E-01	7.33E-02	9.75E-06
W01H16R00T04	1.03E-01	4.86E-01	8.22E-02	2.24E-03
W02H08R00T04	1.10E-01	-8.43E-03	7.39E-02	2.88E-05
W08H02R00T04	1.03E-01	1.36E-01	7.71E-02	8.99E-04
W16H01R00T04	8.49E-02	7.42E-01	8.82E-02	4.00E-03
W01H01R05T04	1.51E-02	-7.50E-02	1.94E-02	1.10E-03
W02H02R05T04	6.00E-02	-1.43E-01	1.97E-02	4.96E-04
W04H04R05T04	2.63E-01	-2.56E-01	2.01E-02	5.01E-04
W08H08R05T04	2.22E+00	-3.81E-01	2.06E-02	6.93E-05
W16H16R05T04	3.14E+02	-4.52E-01	2.08E-02	1.67E-08
W01H16R05T04	1.49E-01	1.63E-01	2.18E-02	2.73E-03
W02H08R05T04	2.43E-01	-1.53E-01	2.05E-02	7.52E-05
W08H02R05T04	1.99E-01	8.88E-04	2.11E-02	9.15E-04
W16H01R05T04	1.11E-01	3.28E-01	2.28E-02	4.62E-03
W01H01R01T04	4.22E-01	-2.88E-01	1.85E-02	7.29E-04
W02H02R01T04	6.15E+00	-3.73E-01	1.89E-02	9.79E-06
W04H04R01T04	6.19E+03	-4.19E-01	1.89E-02	3.69E-11
W08H08R01T04	2.94E+08	4.54E-07	1.89E-02	1.48E-29
W16H16R01T04	2.94E+08	3.95E-07	1.89E-02	1.47E-29
W01H16R01T04	1.70E+00	-3.24E-01	1.88E-02	4.97E-05
W02H08R01T04	7.25E+01	-4.04E-01	1.89E-02	1.55E-07
W08H02R01T04	6.72E+00	-3.70E-01	1.89E-02	7.55E-06
W16H01R01T04	6.23E-01	-2.71E-01	1.87E-02	2.84E-04
			Average	8.88E-4
			Max	5.97E-3

Bibliography

[1] Berthold K.P. Horn. *Robot Vision.* The MIT Press, 1986.

[2] Intersil Corporation. *ISL29200 Preliminary Datasheet*, 2011.

[3] Marc Levoy. Light-field-parameterizations.png. CC-BY-SA-2.0, October 9th 2009.

[4] Morten S. Mikkelsen. Microfacet based bidirectional reflectance distribution function. University of Copenhagen Department of Computer Science, November 2009. Graduate Project.

[5] oomlout. Sharp gp2y0a21yk ir proximity sensor.jpg. CC-BY-2.5; GFDL-WITH-DISCLAIMERS; CC-BY-SA-3.0-MIGRATED, August 26th 2006.

[6] R.L.Cook and K. E. Torrance. A reflectance model for computer graphics. *Computer Graphics*, 15(3):307–316, August 1981.

[7] D. Stoppa, L. Pancheri, M. Scandiuzzo, L. Gonzo, G. Dalla Betta, and A. Simoni. A cmos 3-d imager based on single photon avalanche diode. *IEEE Transactions on Circuits and Systems*, 54(1):4–12, January 2007.

[8] David Stoppa and Andrea Simoni. Single-photon detectors for time-of-flight range imaging. In Peter Seitz and Albert J.P. Theuwissen, editors, *Single-Photon Imaging*, volume 160 of *Springer Series in Optical Sciences*, chapter 12. Springer, August 2011.

[9] Gilbert Strang. *Computational Science and Engineering.* Wellesley-Cambridge Press, 2007.

[10] K. E. Torrance and E. M. Sparrow. Theory for off-specular reflection from roughened surfaces. *Journal of the Optical Society of America*, 57(9):1105–1114, September 1967.

[11] A. Velten, T. Willwacher, O. Gupta, A. Veeraraghavan, M. G. Bawendi, and R. Raskar. Recovering three dimensional shape around a corner using ultra-fast time-of-flight imaging. *Nature Communications*, March 2012.